Physicochemical Properties of Atmospheric Aerosol Particles over Suburban and Remote Locations and Development of Techniques for the Improvement of their Determination Methods

Spyridon Bezantakos

A dissertation submitted to the

University of the Aegean

June 2016

Status: Final

Acknowledgments

First I wish to express my greatest appreciation to the Professor George Biskos, for introducing me to the field of Aerosol Science and for providing crucial suggestions, ideas and guidance during my research. I would also like to thank Prof. K. Eleftheriadis and the group of *Institute of Nuclear Technology and Radiation Protection*, N.S.C.R. Demokritos, Prof. N. Mihalopoulos and the group of *Department of Chemistry, University of Crete*, Prof. S. Pandis and the group of *Institute of Chemical Engineering, ICE-HT, Patras,* Prof. A. Nenes, Prof. A. Schmidt-Ott and the group of *Faculty of Applied Sciences, Delft University of Technology,* Prof. C. Pilinis and Prof. C. Matsoukas for providing infrastructure/resources and for their precious help and suggestions throughout my research.

Special thanks to K. Barmpounis, Dr. M. Giamarelou, Dr. A. Bougiatioti, Dr. E. Kostenidou and S. Vratolis for their excellent cooperation during the experiments conducted and exchange of ideas.

Last but not least, I would like to thank my beloved friends and family for their continuous support and encouragement.

This research has been co-financed by the European Union (European Social Fund – ESF) and Greek national funds through the Operational Program "Education and Lifelong Learning" of the National Strategic Reference Framework (NSRF) - Research Funding Program: THALES. Investing in knowledge society through the European Social Fund: "Sources and physicochemical properties of fine and ultrafine aerosol particles that affect the regional climate of Greece".

Contents

Summary

Aerosol particles affect the Earth's climate directly by absorbing and scattering solar radiation and indirectly by acting as cloud condensation nuclei. The contribution of these effects on climate depends on the size and chemical composition of aerosol particles, which in turn defines their hygroscopicity (i.e., their ability to take up water). Despite that thermodynamic models can be used to accurately predict the hygroscopic behavior of particles consisting of inorganic matter, existing knowledge leads to inaccurate predictions in cases of particles consisting purely of organic or mixtures of inorganic and organic compounds. The use of the hygroscopic parameter κ provides a parameterization of the hygroscopic behavior of mixed particles when the hygroscopicity and the volume fraction of each species comprising the particle are known. Considering the high spatial and temporal variability in chemical composition of atmospheric particles high temporal resolution, direct observations of particles hygroscopicity and/or chemical composition in different regions are needed in order to reduce the uncertainties of their impact on the climate.

Part I of this work provides direct observations on the hygroscopic behavior of atmospheric aerosols over remote and suburban regions, located in Greece, with the aim to better understand their impacts on the regional and global climate. Direct measurements of the hygroscopic properties of aerosol particles are directly compared to predicted particle hygroscopicity using information of their chemical composition, which was derived using aerosol mass spectrometry (AMS). Measurements were conducted at a remote site on the island of Lemnos in the Aegean sea and at two suburban sites, located near Patras and Athens.

Particles measured at the remote site of Lemnos exhibited moderate hygroscopicity, which is indicative of particles consisting of a mixture of inorganic and organic compounds. This was corroborated by measurements of particle chemical composition, conducted using an airborne platform, which during the measurements was flying over the wider region of the Aegean Sea. The good closure between the directly measured (ground station) and the estimated hygroscopicity using the particles chemical composition measurements (airborne AMS) at the vicinity of the monitoring station, allowed to further estimation of particles hygroscopicity in the wider Aegean Sea region.

The spatial variation of the estimated aerosol hygroscopicities was attributed to the different origins and paths of the air masses reaching the region, which in turn had a major effect in particle chemical composition.

Particles measured at the suburban sites of Patras and Athens showed differences in their hygroscopic properties. Particles sampled at Patras exhibited moderate hygroscopic behavior, which was more or less similar to other rural regions of continental Europe, while in contrast, those sampled in Athens exhibited significant temporal variation, ranging from moderate to highly hygroscopic. The estimated aerosol hygroscopicity (derived by chemical composition measurements conducted on both sites with AMS) gave better closure with the measurements at Patras suburban site than the one located near Athens. Differences between the measured and the estimated aerosol hygroscopicity could be attributed to the presence of organic species that are more hygroscopic than those commonly observed in the atmosphere. However, the associated volume fractions in the particle phase should dominate in order to explain the measured hygroscopicities, which are highly uncommon and have never been reported at field measurements in the past.

The second part of the thesis provides means and methods of improving the techniques used in measuring the size and hygroscopicity of aerosol particles. The motivation in trying to improve or find new methods/equipment is to provide measurements of higher spatial/temporal resolution which could be achieved by:

1. Reducing the time needed for each measurement, thus increasing the temporal resolution of the measurements.
2. Reducing the size/weight of the measuring equipment, thus improving its mobility, allowing easier and faster transport, leading to higher spatial resolution.
3. Reducing the cost allowing the development of a more extended network for monitoring aerosol physicochemical properties.

The first chapter of this part assesses in a theoretical way errors in hygroscopicity measurements conducted with hygroscopic tandem DMAs (HTDMAs), caused by temperature and relative humidity (RH) non-uniformities in the setup. Such non-uniformities can lead to erroneous estimates of the apparent hygroscopic behavior of the

sampled particles, as has been shown experimentally in the past. A prompt phase transition, for example, may become smeared and be erroneously interpreted as non-prompt. Although these issues have been raised in the past through experimental observations, it is the first time that theoretical models are coupled in order to explain the combined effect of these non-uniformities in the measured particle hygroscopicity. Quantitative results were provided by simulating the trajectories and the state of the particles classified in a DMA with non-uniform RH and temperature profiles, corroborating earlier observations and suggesting that such experimental artifacts can induce particle growth within the second DMA. Given the importance of maintaining uniform RH and temperature inside the second DMA of HTDMA systems and the limitations of existing RH and temperature sensors, the chapter further provides suggestions for the operation of HTDMA systems.

The second chapter of the 2nd part describes a simple modification of a classical cylindrical DMA with three monodisperse outlets in its central electrode (namely, the 3MO-DMA), with the objective of using it as first DMA in TDMA systems for reducing their measuring cycle time. The performance of the 3MO-DMA operated at different flow conditions was evaluated in laboratory conditions, and compared with theoretical predictions using the generic DMA transfer function provided by Giamarelou et al. (2012). The theory predicted accurately (i.e., within 3%) the geometric mean diameters of the three distinct populations, as well as the resolutions of the first and the third outlet, under all experimental conditions. Despite that the geometric standard deviation of the monodisperse aerosol from outlet #2 corresponded to a monodisperse aerosol (σ_g of up to 1.08 at 8.0 lpm sheath and 1.5 lpm aerosol flow), the resolution of this outlet was 10 to 74% lower than that predicted theoretically depending on the sheath-to-aerosol flow ratio. Despite the lower resolution of the 2nd monodisperse particle outlet compared to the rest, the 3MO-DMA designed and tested in this work can be used as a first DMA in TDMA systems. Doing so provides simultaneously three distinct monodisperse particle populations with accurately defined geometrical median diameters, thereby reducing the measuring cycle of the entire system when used to probe the size-dependent properties of particles of different size.

The third chapter of the second part describes the performance of an inexpensive and highly portable, simple cylindrical geometry particle segregator, made by electrostatic dissipative materials (EDMs). Apart from characterizing its performance a semi-empirical model for estimating particles penetration through the EDM-segregator and the main physical principles behind its operation are provided. EDM-segregators when combined with a differential mobility analyzer (DMA) and a particle number concentration detector can be employed for probing size-dependent aerosol properties such as hygroscopicity or volatility. Laboratory tests probing the volatility of ammonium sulfate particles carried out with this method are also provided in this chapter.

Περίληψη

Τα αιωρούμενα σωματίδια επηρεάζουν το κλίμα της Γης άμεσα απορροφώντας και σκεδάζοντας την ηλιακή ακτινοβολία και έμμεσα ενεργώντας ως πυρήνες συμπύκνωσης συννέφων. Η συνεισφορά αυτών των επιδράσεων των αιωρούμενων σωματιδίων στο κλίμα εξαρτάται από το μέγεθος και την χημική τους σύσταση, η οποία με την σειρά της καθορίζει την υγροσκοπικότητά τους (δηλ. την ικανότητά τους να απορροφούν νερό). Παρότι θερμοδυναμικά μοντέλα μπορούν να χρησιμοποιηθούν για να προβλέψουν επακριβώς την υγροσκοπική συμπεριφορά σωματιδίων που αποτελούνται από ανόργανες ενώσεις, η υπάρχουσα γνώση είναι ελλειπής για να προβλέψει περιπτώσεις που τα σωματίδια αποτελούνται καθαρά από οργανικές ή από μίγματα ανόργανων και οργανικών ενώσεων. Η χρήση της υγροσκοπικής παραμέτρου *κ* επιτρέπει την ακριβέστερη προσέγγιση της υγροσκοπικής συμπεριφοράς των ανάμικτων σωματιδίων, όταν η υγροσκοπικότητα και το κλάσμα όγκου του κάθε χημικού είδους που αποτελεί το σωματίδιο, είναι γνωστά. Δεδομένου ότι η χημική σύσταση των αιωρούμενων σωματιδίων ποικίλει χωρικά και χρονικά, απ' απευθείας παρατηρήσεις, υψηλής χρονικής ανάλυσης, της υγροσκοπικότητας των σωματιδίων και/ή της χημικής τους σύστασης σε διαφορετικές περιοχές, είναι επομένως απαραίτητες για να μειωθούν οι αβεβαιότητες των επιδράσεών τους στο κλίμα.

Στο πρώτο μέρος της παρούσας διατριβής παρέχονται παρατηρήσεις της υγροσκοπικής συμπεριφοράς των ατμοσφαιρικών αιωρούμενων σωματιδίων σε

απομακρυσμένες και σε περιαστικές περιοχές της Ελλάδας με σκοπό την καλλίτερη κατανόηση των επιδράσεών τους στο τοπικό και παγκόσμιο κλίμα. Οι μετρούμενες υγροσκοπικές ιδιότητες των σωματιδίων συγκρίνονται απευθείας με την εκτιμώμενη υγροσκοπικότητά τους, όπως προκύπτει από την χημική τους σύσταση, η οποία προέκυψε από φασματογραφία μάζας αιωρούμενων σωματιδίων (aerosol mass spectrometry; AMS). Οι μετρήσεις διεξήχθησαν σε απομακρυσμένο σταθμό στο νησί της Λήμνου, στο Αιγαίο Πέλαγος, και σε δύο περιαστικούς σταθμούς που βρίσκονται πλησίον της Πάτρας και της Αθήνας.

Τα σωματίδια που μετρήθηκαν στον απομακρυσμένο σταθμό της Λήμνου επέδειξαν ενδιάμεσες τιμές υγροσκοπικότητας, ενδεικτικές για σωματίδια που αποτελούνται από μείγμα ανόργανων και οργανικών ενώσεων. Αυτό επιβεβαιώθηκε από τις μετρήσεις της χημικής τους σύστασης, οι οποίες διεξήχθησαν χρησιμοποιώντας μια εναέρια πλατφόρμα (αεροσκάφος) και η οποία κατά την ίδια χρονική περίοδο πετούσε πάνω από την ευρύτερη περιοχή του Αιγαίου Πελάγους. Η καλή συμφωνία μεταξύ της υγροσκοπικότητας που υπολογίστηκε από την χημική σύσταση των σωματιδίων (αερομεταφερόμενο AMS) και των μετρήσεων (σταθμός εδάφους) επέτρεψε την περαιτέρω εκτίμηση της υγροσκοπικότητας των αιωρούμενων σωματιδίων για ολόκληρη την ευρύτερη περιοχή του Αιγαίου. Η χωρική ποικιλομορφία των εκτιμώμενων τιμών υγροσκοπικότητας των αιωρούμενων σωματιδίων αποδίδεται στις διαφορετικές αφετηρίες και διαδρομές των αέριων μαζών που φτάνουν στην περιοχή, οι οποίες με την σειρά τους επηρεάζουν έντονα την χημική σύσταση των σωματιδίων.

Τα σωματίδια που μετρήθηκαν στους περιαστικούς σταθμούς της Πάτρας και της Αθήνας έδειξαν διαφορές ως προς τις υγροσκοπικές τους ιδιότητες. Τα σωματίδια που μετρήθηκαν στην Πάτρα επέδειξαν μέτρια υγροσκοπικότητα, παρόμοια με αυτήν που παρατηρείται σε ημιαστικές/αγροτικές περιοχές της ηπειρωτικής Ευρώπης, ενώ αντίθετα τα σωματίδια που μετρήθηκαν στην Αθήνα επέδειξαν σημαντική χρονική μεταβολή, κυμαινόμενα από μετρίως ως υψηλά υγροσκοπικά. Η εκτιμώμενη (βάση των μετρήσεων της χημικής τους σύστασης που διεξήχθη και στους δύο σταθμούς χρησιμοποιώντας AMS) υγροσκοπικότητα συσχετίζεται καλλίτερα με τις μετρήσεις στον περιαστικό σταθμό της Πάτρας από ότι σε αυτόν που βρίσκονταν κοντά στην Αθήνα. Οι διαφορές μεταξύ μετρούμενης και εκτιμόμενης υγροσκοπικότητας θα μπορούσαν να οφείλονται

είτε στην παρουσία συγκεκριμένων οργανικών ενώσεων, οι οποίες είναι πολύ περισσότερο υγροσκοπικές από αυτές που βρίσκονται συνήθως στην ατμόσφαιρα. Παρόλα αυτά, το κλάσμα όγκου αυτών των ενώσεων στην σωματιδιακή φάση θα έπρεπε να κυριαρχεί, ώστε να εξηγήσει τις παρατηρούμενες υγροσκοπικότητες, κάτι το οποίο είναι πολύ ασυνήθιστο και δεν έχει ποτέ αναφερθεί σε μετρήσεις πεδίου κατά το περελθόν.

Στο δεύτερο μέρος της διατριβής παρέχονται τρόποι και μέθοδοι για την βελτίωση των τεχνικών που χρησιμοποιούνται για τον καθορισμό του μεγέθους και της υγροσκοπικότητας των αιωρούμενων σωματιδίων. Το κίνητρο στην προσπάθεια βελτίωσης ή ανεύρεσης νέων μεθόδων/εξοπλισμού είναι η επίτευξη μετρήσεων με υψηλότερη χωρική/χρονική ανάλυση, κάτι που μπορεί να επιτευχθεί με:

1. Την μείωση του αναγκαίου χρόνου για κάθε μέτρηση, αυξάνοντας έτσι την χρονική ανάλυση των μετρήσεων.
2. Την μείωση του βάρους/μεγέθους του μετρητικού εξοπλισμού, βελτιώνοντας την φορητότητα του, οδηγώντας έτσι σε υψηλότερη χωρική ανάλυση.
3. Την μείωση του κόστους, επιτρέποντας την ανάπτυξη ενός πιο εκτεταμένου δικτύου για την παρακολούθηση των φυσικοχημικών ιδιοτήτων των αερολυμάτων.

Το πρώτο κεφάλαιο αυτού του μέρους αξιολογεί θεωρητικά σφάλματα σε μετρήσεις υγροσκοπικότητας που διεξήχθησαν με συστήματα DMA σε σειρά για την μέτρηση της υγροσκοπικότητας (Hygroscopic Tandem DMAs; HTDMAs), προκαλούμενες από ανομοιογένειες στην θερμοκρασια και σχετική υγρασία (ΣΥ) των συστημάτων. Αυτές οι ανομοιογένειες μπορούν να οδηγήσουν σε εσφαλμένες εκτιμήσεις σχετικά με την φαινομενική υγροσκοπική συμπεριφορά των υπό μελέτη σωματιδίων, όπως είχε δειχτεί πειραματικά και στο παρελθόν. Μια στιγμιαία αλλαγή φάσης των σωματίδιων από στερεά σε υγρά, παραδείγματος χάρη, μπορεί να ερμηνευτεί λανθασμένα ως σταδιακή. Παρόλο που αυτά τα θέματα έχουν αναδειχτεί και στο παρελθόν μέσω πειραματικών παρατηρήσεων, είναι η πρώτη φορά που θεωρητικά μοντέλα συνδέθηκαν ώστε να εξηγήσουν το συνδιαστικό φαινόμενο αυτών των ανομοιωγενειών στην μετρούμενη υγροσκοπικότητα των αιωρούμενων σωματιδίων. Ποσοτικά αποτελέσματα παρέχονται προσομοιώνοντας τις τροχιές και την κατάσταση

(ως προς την υγροσκοπικότητα) των αιωρούμενων σωματιδίων εντός ενός ταξινομητή DMA, υπό ανομοιωγενείς συνθήκες θερμοκρασίας και ΣΥ, επιβεβαιώνοντας παλιότερες παρατηρήσεις και αποδεικνύοντας ότι τέτοια πειραματικά σφάλματα μπορούν να επιφέρουν αύξηση του μεγέθους των σωματιδίων εντός του ταξινομητή (DMA). Δεδομένης της σημασίας της διατήρησης ομοιογενούς θερμοκρασίας και ΣΥ εντός του δεύτερου ταξινομητή ενός συστήματος μέτρησης της υγροσκοπικότητας των σωματιδίων (HTDMA) και τους περιορισμούς των υπαρχόντων αισθητηρίων ΣΥ και θερμοκρασίας παρέχονται επιπλέον προτάσεις για την ορθή λειτουργία αυτών των συστημάτων.

Στο δεύτερο κεφάλαιο του δεύτερου μέρους προτείνεται μια απλοποιημένη μετατροπή ενός κλασσικού κυλινδρικού ταξινομητή (DMA) με τρεις εξόδους στο κεντρικό του ηλεκτρόδιο (ονομαστικά το 3MO-DMA), με σκοπό την χρήση του ως πρώτου ταξινομητή (DMA) σε συστήματα ταξινομητών εν σειρά (TDMA) για την μείωση του κύκλου μέτρησής τους. Η απόδοση του 3MO-DMA σε διαφορετικές συνθήκες ροής μελετήθηκε στο εργαστήριο και συγκρίθηκε με τις θεωρητικές προβλέψεις χρησιμοποιώντας την συνάρτηση μεταφοράς των Giamarelou et al. (2012). Η θεωρεία προέβλεψε με ακρίβεια (μέγιστο σφάλμα 3%) τις γεωμετρικές μέσες διαμέτρους των τριών ξεχωριστών (από άποψη μεγέθους) πληθυσμών σωματιδίων από τις διαφορετικές εξόδους, καθώς και την διακριτική ικανότητα της πρώτης και τρίτης εξόδου, σε όλες τις πειραματικές συνθήκες που δοκιμάστηκαν. Παρά το γεγονός ότι η γεωμετρική τυπική απόκλιση των ταξινομηθέντων σωματιδίων της δεύτερης εξόδου ανταποκρίνεται σε σωματίδια στενού εύρους διαμέτρων (σ_g ως 1.08 με 8.0 lpm ροή sheath και 1.5 lpm ροή aerosol), η διακριτική ικανότητα αυτής της εξόδου ήταν από 10 έως 74% χαμηλότερη από τις θεωρητικές προβλέψεις, ανάλογα με τον λόγο των ροών sheath/aerosol. Παρά την χαμηλότερη διακριτική ικανότητα της δεύτερης εξόδου, σε σχέση με τις υπόλοιπες, το 3MO-DMA που σχεδιάστηκε και ελέγχτηκε σε αυτήν την εργασία μπορεί να χρησιμοποιηθεί επαρκώς ως πρώτος ταξινομητής DMA σε συστήματα σειράς (TDMA). Η χρήση του αυτή παρέχει ταυτόχρονα τρεις ξεχωριστούς πληθυσμούς, με στενό εύρος μεγεθών, με καθορισμένες μέσες γεωμετρικές διαμέτρους, μειώνοντας με τον τρόπο αυτών τον κύκλο μέτρησης όλου του συστήματος, όταν αυτό χρησιμοποιείται σε μετρήσεις πεδίου.

Στο τρίτο κεφάλαιο του δεύτερου μέρους μελετάται η απόδοση ενός φτηνού και φορητού, απλής κυλινδρικής γεωμετρίας ταξινομητή σωματιδίων, ο οποίος κατασκευάστηκε από υλικά διάχυσης στατικού ηλεκτρισμού (electrostatic dissipative materials; EDMs). Εκτός από τον χαρακτηρισμό της απόδοσης, παρέχεται και μια ημι-εμπειρική εξίσωση για την εκτίμηση της διείσδυσης των σωματιδίων μέσω του ταξινομητή EDM, καθώς και οι βασικές φυσικές αρχές πίσω από την λειτουργία του. Ένας ταξινομητής EDM σε συνδυασμό με έναν αναλυτή διαφορικής κινητικότητας (differential mobility analyzer; DMA) και έναν ανιχνευτή αριθμητικής συγκέντρωσης σωματιδίων μπορεί να χρησιμοποιηθεί για την μέτρηση των εξαρτόμενων από το μέγεθος, φυσικοχημικών ιδιοτήτων, των αιωρούμενων σωματιδίων, όπως η υγροσκοπικότητα και η πτητικότητα. Εργαστηριακές μετρήσεις της πτητικότητας αιωρούμενων σωματιδίων θειϊκού αμμωνίου, η οποίες διεξήχθησαν με την μέθοδο αυτή, παρέχονται επίσης σε αυτό το κεφάλαιο.

1. Introduction

1.1 Atmospheric aerosol particles

The term aerosol is used to define gas suspended solid or liquid particles having sizes that vary from a few nanometers to a few hundreds of micrometers (Hinds, 1999). Aerosol particles may directly be emitted in the atmosphere (primary aerosols) or resulted by nucleation of gaseous species (secondary aerosols; Seinfeld and Pandis, 2006). While their origin can be both natural and anthropogenic, the contribution of the latter is constantly increasing since the beginning of the industrial revolution primarily due to the increased usage of fossil fuels for supporting the modern way of living (Raes et al., 2000).

Aerosols affect Earth's climate directly by absorbing or scattering incoming solar radiation (Haywood and Boucher, 2000) and indirectly by acting as Cloud Condensation Nuclei (i.e., indirect effect; Ogren and Charlson, 1992). Both these effects depend on particle size and chemical composition, both of which vary spatially and temporarily as a result of the large diversity of their sources and the different physicochemical processes they are involved in during their lifetime (Hallquist et al., 2009). Measuring the variability in the size of atmospheric particles is therefore of primary importance in understanding their climate impacts (McMurry, 2000). Early methods for sizing aerosol particles were based on size-dependent properties such as their diffusivity (for small particles) and inertia (for bigger particles). For instance, diffusion batteries were used for classifying small particles (e.g., Gormley and Kennedy, 1949), while impactors (e.g., Marple 1970) and cyclones (e.g., Leith and Mehta, 1973) for sizing large segregated particles. While simple and easy to construct, deploy, and maintain, these instruments have limited resolution and measuring size range. Knutson and Whitby (1975) introduced the Differential Mobility Analyzer (DMA), which exploited the motion of charged particles in a flowing aerosol under an electric field, for determining their electrical mobility and from that their size. This approach provided a significant improvement in sizing resolution and extended the range of particle sizes that a single instrument could classify.

Particle chemical composition also plays a role in the climate impacts of aerosols by directly defining their optical properties, and indirectly by affecting their ability to take up water (i.e., hygroscopicity), which also affects their size, optical properties and their ability to act as CCN.

1.2 Aerosol hygroscopicity

Particles that take up water when exposed to elevated relative humidity (RH) conditions (i.e., hygroscopic particles), can exhibit an increase in their size due to water condensation. The hygroscopic growth factor (g) is often used to quantify the growth of particles due to water uptake, which is expressed as:

$$g(\mathrm{RH})=\frac{d(\mathrm{RH})}{d_{dry}}, \quad (1.1)$$

where $d(\mathrm{RH})$ and d_{dry} are the diameters of the sampled particles at the hydrated and at the dry state, respectively.

Inorganic salt particles spontaneously transform from solid to droplets when exposed to RH above a certain threshold, namely the deliquescence RH (DRH; Seinfeld and Pandis, 2006). The resulting droplets, however, will transform into solid particles at lower RH than the DRH, exhibiting a hysteresis effect. The RH threshold at which particles in the droplet state will transform into solids is called the efflorescence RH (ERH; Seinfeld and Pandis, 2006). Both DRH and ERH depend on particles chemical composition. The water saturation S_R, equal to RH/100 and the diameter of droplets when the particles are in the aqueous state, are connected through the Köhler equation (Köhler, 1936):

$$S_R = a_{w,s}\ exp\left(\frac{4\sigma_{\mathrm{aq}}M_{\mathrm{w}}}{\rho_{\mathrm{w}}RTd(\mathrm{RH})}\right) \quad (1.2)$$

where $\alpha_{\mathrm{w,s}}$ is the water activity for the specific solution, σ_{aq} is the surface tension of the solution droplet, M_{w} and ρ_{w} are respectively the density and molar weight of water, R is the universal gas constant and T the absolute temperature. The exponential term (Kelvin term) accounts for the increase in relative vapor pressure, as compared to the one over a flat surface, caused by the curved surface of the particle. It should be noted here that the Kelvin term becomes dominant for particles smaller than ca. 100 nm.

While basic thermodynamic models (e.g., Clegg et al., 1998) are used to accurately predict the hygroscopic behavior of pure or mixed inorganic species, the complexity of atmospheric particles which mainly consist of mixtures of inorganic and organic compounds limits their predictability. To overcome the difficulties involved in associating the variable and complex chemical composition of atmospheric particles, with their hygroscopic behavior, Petters and Kreidenweis (2007) proposed the use of a single hygroscopic parameter κ. Using this parameter, the hygroscopic growth factor of the particles can be expressed as:

$$g\,(\mathrm{RH}) = \left(1 + \kappa\left(\frac{a_w}{1-a_w}\right)\right)^{1/3}, \tag{1.3}$$

with

$$a_{\mathrm{w}} \approx \frac{\mathrm{RH}}{100}\left(exp\left(\frac{4\sigma_{s/\alpha}\ M_w}{RT\rho_w d(RH)}\right)\right)^{-1}. \tag{1.4}$$

Here $\sigma_{s/a}$ denotes the surface tension of pure water, equal to 0.072 J m^{-2}. The surface tension of pure water is used in Eq. 1.4, as the best approximation, since the surface tension of the resulting solution would be unknown, for particles of unknown chemical composition, which is the usual case during field measurements.

A κ value of zero is assigned to hydrophobic (i.e., completely insoluble but wettable) particles. Most typical atmospheric soluble-salt particles exhibit higher κ values (e.g. 0.53 and 1.12 for ammonium sulfate and sodium chloride, respectively), whereas those of most organic aerosols lay in the range between zero and 0.3 (Petters and Kreidenweis 2007).

In cases where aerosol particles are mixtures of different species, their hygroscopic parameter κ can be calculated using information of their chemical composition as follows:

$$\kappa = \sum_{\mathrm{i}} \varepsilon_{\mathrm{i}}\, \kappa_{\mathrm{i}}\,, \tag{1.5}$$

where $\varepsilon_i = V_{\mathrm{si}}/V_{\mathrm{s}}$ and κ_{i} are the volume fraction and the hygroscopic parameter of the *i*th chemical species comprising the particles, with V_{si} being the volume occupied by that species and V_{s} the volume of the dry particle.

1.3 Measurement techniques of aerosols hygroscopicity

A variety of experimental methods has been employed for measuring the hygroscopic behavior of airborne particles. More specifically, these methods involve changes in particle mass (e.g. using Electrodynamic Balance EDBs; Peng and Chan, 2001), changing in particles optical properties (e.g. using a wet and dry nephelometer; McInnes et al., 1998) and in particles electrical mobility diameter (e.g. using a Hygroscopic Tandem Differential Mobility Analyzer; HTDMA; Rader and McMurry, 1986). The latter offers size resolved, near real-time measurements of changes in particles electrical mobility diameter after exposing them to elevated RH conditions and is considered the method of choice for sub micrometer particles. The HTDMA mainly consists of two Differential Mobility Analyzers (DMAs; Knutson and Whitby, 1975), and a Condensation Particle Counter (CPC, TSI Model 3772; Agarwal and Sem, 1980). Figure 1.1 depicts the operating principle of the HTDMA. In brief, the particles in the sample flow are initially dried and passed through a bipolar charger before entering the first DMA (DMA-1) that produces a monodisperse aerosol flow. The monodisperse particles downstream DMA-1 are then exposed to elevated RH conditions inside the humidifier before their size is measured by the second DMA (DMA-2) and the CPC.

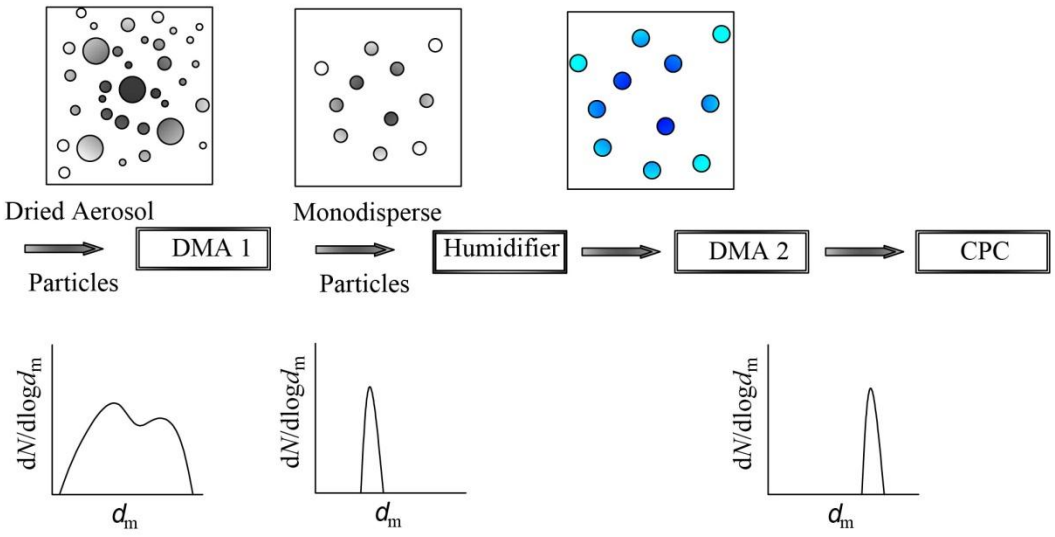

Fig. 1.1: Schematic illustration of the HTDMA measuring principle. Aerosols are initially dried, neutralized before entering the first DMA (DMA-1). The monodisperse particles produced by DMA-1are then exposed to increased RH conditions inside the humidifier and their size distribution is measured downstream by the second DMA (DMA-2) and the CPC.

While all of the methods described above are used for measuring particle hygroscopic properties at sub-saturation conditions (i.e., RH < 100%) a Continuous Flow Streamwise Thermal Gradient CCN Chamber (CFSTGC; Roberts and Nenes, 2005; cf. Fig. 1.2a) is able to provide information on particle hygroscopicity at the super-saturation regime. In brief, aerosol particles are introduced inside a wet ceramic column surrounded by a saturated (i.e., RH=100%) sheath flow. A temperature gradient is maintained within the column resulting in quasi uniform water vapor super-saturation along the centerline. Depending on their size at dry conditions and their chemical composition, aerosol particles can become CCN active above a certain super-saturation conditions, namely above the critical super-saturation (S_c). CCN active particles are then optically counted downstream of the growth chamber by an Optical Particle Counter (OPC).

The CFSTGC (CCNC from now on for simplicity reasons) can be employed downstream DMA-1 of the HTDMA system for simultaneously measuring size resolved particle hygroscopicity at both sub- and super-saturated conditions. In the more advance "Scanning Flow CCN Analysis" (SFCA) operation mode, the flow rate in the growth chamber changes over time, while a constant streamwise temperature difference is maintained. This causes super-saturation to change continuously, allowing the rapid and continuous measurement of super-saturation spectra with high temporal resolution without being affected by shifts in activation kinetics and aerosol composition (Moore and Nenes, 2009). For each particle size, the critical super-saturation value $S_{c,}$ above which particles act as CCN was obtained from Köhler theory (Moore et al., 2012a). The CCN activity of the particles is characterized by the activation ratio given by:

$$R_a \equiv \frac{CCN}{CN} = a_0 + \frac{a_1 - a_0}{1 + (Q/Q_{50})^{-a_2}} \quad , \tag{1.6}$$

where CCN and CN are the activated and total particle concentrations, while a_0, a_1, a_2 and Q_{50} are constants that describe the minimum, maximum, slope and inflection point of the sigmoidal, respectively, while Q is the instantaneous volumetric flow rate. The inflection point (i.e., Q_{50} or "critical flow rate"), corresponds to the instantaneous flow rate, that produces a level of super-saturation within the CCNC, required to activate the

measured monodisperse aerosol. An example of a CCN activity spectrum with the sigmoidal fit and its defined parameters is depicted in Fig. 1.2b.

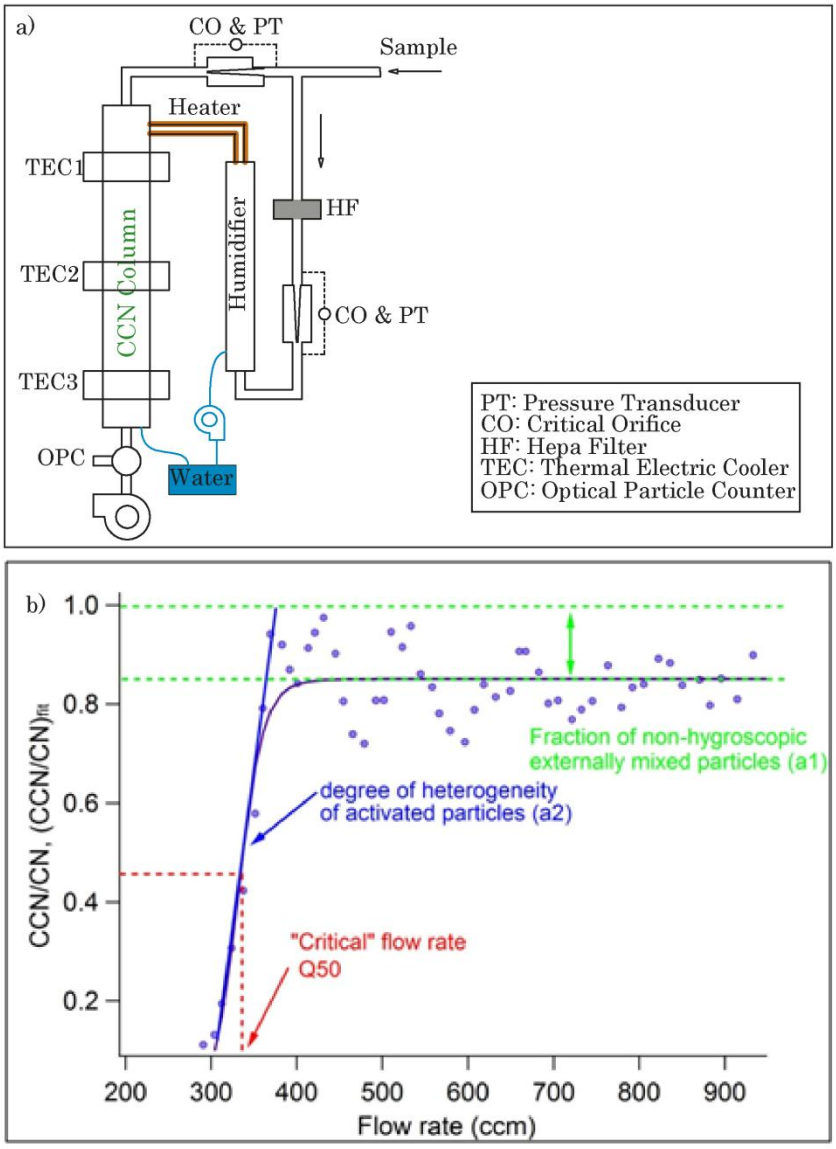

Fig. 1.2: Schematic illustration of the CCNC (**a**; Roberts and Nenes, 2005) and example of measured CCN activity spectrum with the sigmoidal fit and its parameters (**b**).

1.4 Motivation

During the last few decades a large attempt is made in order to better understand the ways that modern human societies affect the climate of the planet and predict the consequences of our actions. During the last two centuries, which in terms of geological time is a short period, we have already concluded that the release of certain gases

("greenhouse gases") in the atmosphere increases its property to absorb infrared radiation and thus increase the temperature of the planet. A wide number of models that capture a number of complex interactions have been developed and used to understand the climate and its changes at a local, regional and global scale. Atmospheric aerosols play also a key role in earth's climate and therefore the study of their effects in climate is intense.

Although the uncertainties regarding the effects of aerosols in the global climate have been reduced during the last few years, these uncertainties remain relatively high in contrast to other sources of climate change (IPCC, 2014). Climate models are largely affected by limited particle emission inventories, while inaccurate particle hygroscopic properties may lead to uncertain estimation of the aerosol indirect effect on a global scale (Lohmann and Ferrachat, 2010). For this reason monitoring the properties of aerosols in different locations and with high temporal resolution is important for reducing these uncertainties.

Part I of this thesis focuses on aerosol hygroscopicity. More specifically it describes and discusses a number of field measurements in remote and sub-urban locations of Greece. Part II provides the means of improving the methods/techniques of determining their properties in order to improve the accuracy and spatial, as well as temporal resolution of these measurements. The sections that follow give an overview of the entire thesis.

1.5 Overview

The first chapter (current chapter) of this thesis serves as an introduction addressing the impacts of aerosol in climate and the importance of high temporal and spatial measurements of the their size and hygroscopicity. Fundamental theoretical background and techniques for probing the hygroscopic properties of particles are also provided.

In the second chapter are reported high temporal resolution chemical composition and hygroscopicity measurements of particles over the Aegean Sea, during a period with prevailing northern winds (i.e., Etesians), which carry polluted air masses from central Europe, the Balkans (including Greece), and the Black Sea (Mihalopoulos et al., 1997; Lelieveld et al., 2002). Measured particle hygroscopicity (i.e., HTDMA on the ground

station) was compared to particles chemical composition (i.e., on-board AMS) when the aircraft was flying in the vicinity of the ground station, using the κ-Köhler theory. Based on the good agreement between the measured and estimated (i.e., from the chemical composition) particle hygroscopicity, vertical profiles of the hygroscopic parameter κ were estimated for the region.

In the third chapter size resolved measurements of particles mixing state and hygroscopicity at sub- and super-saturated conditions, together with high temporal measurements of their chemical composition, are reported for two suburban sites. The back trajectories of the air masses reaching the sites were used to distinguish between periods of increased pollution, originating from the nearby cities. The hygroscopic parameter of the particles organic fraction at sub- and super-saturated conditions was also estimated using the size resolved particles chemical composition and hygroscopicity.

In the fourth chapter the experimental artifacts caused by non-uniform temperature and RH in the second DMA of an HTDMA system are theoretically assessed, using for the first time a combination of numerical models. A comparison between the model results with previous experimental observations and guidelines to reduce the effects of such non-uniformities on the measured particles hygroscopicity are provided as well.

In the fifth chapter a simple modification of a classical cylindrical DMA to have three monodisperse outlets (i.e., 3MODMA), with the scope of reducing the measuring cycle of HTDMA systems is described. The classification accuracy and the resolution of the 3MODMA was experimentally evaluated and compared with the theory provided by Giamarelou et al. (2012).

The sixth chapter describes a simple and cost effective method for size segregating sub 100 nm aerosols. The method employs a simple tube made of electrostatic dissipative materials (EDMs), which can be operated at high voltages. The resulted electrostatic force decelerates the particles, enhancing their diffusional deposition. Except from the characterization of the EDM-segregator, a semi-empirical equation for estimating particle penetration through the tube at different flows and voltages as well as its basic operating principles are provided. In addition, an example of its use for probing the volatility of aerosol particles is given.

Finally in the seventh chapter the general conclusions of the present work are given, together with some suggestions for future investigation.

References

Agarwal, J. K. and Sem, G. J. (1980). Continuous flow, single-particle-counting condensation nucleus counter. *J. Aerosol Sci.*, 11:343–357.

Clegg, S. L., Brimblecombe, P., Wexler, A. S.: Thermodynamic Model of the System H^+-NH_4^+ - SO_4^{2-} - NO_3^- - H_2O at TroposphericTemperatures. *J. Phys. Chem. A*, 102, 2137–2154, 1998.

Giamarelou, M., Stolzenburg, M., and Biskos, G. (2012). The Multiple Monodisperse Outlet Differential Mobility Analyzer: Derivation of its Transfer Function and Resolution. *Aerosol Sci. Technol.*, 46:951–965.

Gormley, P.G., Kennedy, M. (1949). Diffusion from a stream flowing through a cylindrical tube. *P. Roy. Irish Acad*. 52: 163-169.

Hallquist, M., Wenger, J. C., Baltensperger, U., Rudich, Y., Simpson, D., Claeys, M., Dommen, J., Donahue, N. M., George, C., Goldstein, A. H., Hamilton, J. F., Herrmann, H., Hoffmann, T., Iinuma, Y., Jang, M., Jenkin, M. E., Jimenez, J. L., Kiendler-Scharr, A., Maenhaut, W., McFiggans, G., Mentel, Th. F., Monod, A., Prévôt, A. S. H., Seinfeld, J. H., Surratt, J. D., Szmigielski, R., Wildt, J.: The formation, properties and impact of secondary organic aerosol: current and emerging issues, *Atmos. Chem. Phys*., 9, 5155–5236, doi:10.5194/acp-9-5155-2009, 2009.

Haywood, J. and Boucher, O.: Estimates of the direct and indirect radiative forcing due to tropospheric aerosols: a review, *Rev. Geophys*., 38, 513–543, 2000.

Hinds, W. C.: Aerosol Technology: Properties, Behavior, and Measurement of Airborne Particles, 2nd Edition. *John Willey & Sons, Inc*., 1999.

IPCC, 2014: Climate Change 2014: Synthesis Report. Contribution of Working Groups I, II and III to the Fifth Assessment Report of the Intergovernmental Panel on Climate Change [Core Writing Team, R.K. Pachauri and L.A. Meyer (eds.)]. IPCC, Geneva, Switzerland, 151 pp.

Knutson, E.O., Whitby, K.T.: Aerosol classification by electric mobility: Apparatus, theory, and applications. *J. Aerosol Sci*., 6, 443-451, 1975.

Köhler, H.: The nucleus in and the growth of hygroscopic droplets, *Trans. Faraday Soc.*, 32, 1152-1161, (1936).

Lelieveld, J., Berresheim, H., Borrmann, S., Crutzen, P. J., Dentener, F. J., Fisher, H., Feichter, J., Flatau, P. J., Heland, J., Holzinger, R., Korrmann, R., Lawrence, M. G., Levin, Z., Markowitz, K. M., Mihalopoulos, N., Minikin, A., Ramanathan, V., de Reus, M., Roelofs, G. J., Scheeren, H. A., Sciare, J., Schlager, H., Schultz, M., Siegmund, P., Steil, B., Stephanou, E. G., Stier, P., Traub, M., Warneke, C., Williams, J., and Ziereis, H.: Global air pollution crossroads over the Mediterranean, *Science*, 298, 794–799, 2002.

Leith, D., Mehta, D., 1973. Cyclone performance and design. *Atmos. Environ.* 7: 527-549.

Lohmann U., Ferrachat, S.: Impact of parametric uncertainties on the present-day climate and on the anthropogenic aerosol effect, *Atmos. Chem. Phys*., 10, 11373–11383, 2010

Marple, V.A., 1970. A fundamental study of inertial impactors, Ph.D. Thesis, Department of Mechanical Engineering, University of Minnesota, Minneapolis, MN.

McInnes, L., Bergin, M., Ogren, J. and Schwartz, S.: Apportionment of light scattering and hygroscopic growth to aerosol composition, *Geophys. Res. Lett.*, 25, 513-516, 1998.

McMurry, P. H. (2000). A review of Atmospheric Aerosol Measurements. *Atmos. Environ*., 34:1959-1999.

Mihalopoulos, N., Stephanou, E., Kanakidou, M., Pilitsidis, S.,Bousquet, P.: Tropospheric aerosol ionic compositionabove the Eastern Mediterranean Area, *Tellus B* 49B, 314–326, 1997.

Moore, Richard H., and Nenes, A.: Scanning flow CCN analysis - A method for fast measurements of CCN spectra. *Aerosol Sci. Tech.* 43.12, 1192-1207, 2009.

Moore, R.H., Cerully, K., Bahreini, R., Brock, C.A., Middelbrook, A.M., and Nenes, A.: Hygroscopicity and composition of California CCN during summer 2010, *J. Geophys. Res.*, 117, D00V12, doi:10.1029/2011JD017352, 2012a.

Ogren, J. and Charlson, J.: Implications for models and measurementsof chemical inhomogeneities among cloud droplets, *Tellus, 44B*, 489–504, 1992.

Peng C. and Chan, C. K.: The water cycles of water-soluble organic salts of atmospheric importance, *Atmos. Environ*. 35, 1183-1992, 2001.

Petters, M. D. & Kreidenweis S. M.: A single parameter representation of hygroscopic growth and cloud condensation nucleus activity, *Atmos. Chem. Phys*., 7, 1961–1971, doi:10.5194/acp-7-1961-2007, 2007.

Rader, D.J., McMurry P.H.: Application of the tandem differential mobility analyzer to studies of droplet growth or evaporation, *J. Aerosol Sci*., 17, 771-787, 1986.

Raes, F., Van Dingenen, R., Vignati, E., Wilson, J., Putaud, J. P., Seinfeld, J H., Adams, P. (2000): Formation and cycling of aerosols in the global troposphere. *Atmos. Environ*., 34, 4214-4220.

Roberts, G. C., and Nenes, A.: A continuous-flow streamwise thermal-gradient CCN chamber for atmospheric measurements. *Aerosol Sci. Tech*. 39.3, 206-221, 2005.

Seinfeld, J. H. & Pandis, S.N., (2006): Atmospheric Chemistry And Physics. *John Wiley & Sons, inc.*

PART I: Physicochemical Properties of Atmospheric Aerosol Particles over Suburban and Remote Locations

2. Chemical Composition and Hygroscopic Properties of Aerosol Particles over the Aegean Sea

S. Bezantakos[1,2], K. Barmpounis[3], M. Giamarelou[1], E. Bossioli[4], M. Tombrou[4], N. Mihalopoulos[5], K. Eleftheriadis[2], J. Kalogiros[6], J. D. Allan[7], A. Bacak[7], C. J. Percival[7], H. Coe[7], and G. Biskos[1,3]

[1]*Department of Environment, University of the Aegean, Mytilene 81100, Greece*

[2]*ERL, Inst. of Nuclear Tech. & Rad. Protection, NCSR Demokritos, 15310 Ag. Paraskevi, Attiki, Greece*

[3]*Faculty of Applied Sciences, Delft University of Technology, Delft 2628-BL, The Netherlands*

[4]*Department of Physics, National and Kapodistrian University of Athens, Athens 15784, Greece*

[5]*Department of Chemistry, University of Crete, Heraklion 71003, Greece*

[6]*Institute of Environmental Research and Sustainable Development, National Observatory of Athens, Athens, Greece*

[7]*School of Earth, Atmospheric and Environmental Science, The University of Manchester, Manchester, United Kingdom*

Correspondence to: G. Biskos
(biskos@aegean.gr; g.biskos@tudelft.nl)
Published: 29 November 2013
Atmospheric Chemistry and Physics
(Atmos. Chem. Phys., 13, 11595–11608, 2013)

Abstract

The chemical composition and water uptake characteristics of sub-micrometre atmospheric particles over the region of the Aegean Sea were measured between 25 August and 11 September 2011 within the framework of the Aegean Game campaign. High temporal-resolution measurements of the chemical composition of the particles were conducted using an airborne compact time-of-flight aerosol mass spectrometer (cToF-AMS). These measurements were performed during two flights from the island of Crete to the island of Lemnos and back. A hygroscopic tandem differential mobility analyser (HTDMA) located on the island of Lemnos was used to measure the ability of the particles to take up water. The HTDMA measurements showed that the particles in the dominant mode were internally mixed, having hygroscopic growth factors that ranged from 1.00 to 1.59 when exposed to 85% relative humidity. When the aircraft flew near the ground station on Lemnos, the cToF-AMS measurements showed that the organic volume fraction of the particles ranged from 43 to 56%. These measurements corroborate the range of hygroscopic growth factors measured by the HTDMA during that time. Good closure between HTDMA and cToF-AMS measurements was achieved when assuming that the organic species were less hygroscopic and had an average density that corresponds to aged organic species. Using the results from the closure study, the cToF-AMS measurements were employed to determine vertical profiles of a representative aerosol hygroscopic parameter κ_{mix}. Calculated κ_{mix} values ranged from 0.19 to 0.84 during the first flight and from 0.22 to 0.80 during the second flight. Air masses of different origin as determined by back trajectory calculations can explain the spatial variation in chemical composition and κ_{mix} values of the particles observed in the region.

2.1. Introduction

Atmospheric aerosol particles affect the global radiative balance of the Earth by directly absorbing and scattering solar radiation (i.e., direct effect; Haywood and Boucher, 2000), and indirectly by acting as Cloud Condensation Nuclei (i.e., indirect effect; Ogren and Charlson, 1992). Scattering and absorption of aerosol particles strongly depends on their size and chemical composition, which are often characterised by high variability as a result of the large diversity of their sources and the different physicochemical processes they are involved in during their lifetime (Hallquist et al., 2009). The chemical composition of the particles also defines their hygroscopicity, i.e., their ability to take up water, which in turn can affect their interaction with incoming solar radiation. To predict the hygroscopic behaviour of pure or mixed inorganic particles one can use basic thermodynamic principles (e.g. Clegg et al., 1998). For particles that consist of organic species or mixtures of organic and inorganic compounds, however, existing knowledge does not allow accurate predictions of their hygroscopicity. This limited understanding is one of the greatest uncertainties in determining the role of atmospheric aerosols on climate.

To overcome the complexities involved in associating the chemical composition of atmospheric particles with their hygroscopic behaviour Petters and Kreidenweis(2007) proposed the use of a single hygroscopic parameter κ. The value of κ is 0 for completely insoluble but wettable particles whose water activity is not affected by water adsorbed on their surface. For typical atmospheric soluble-salt particles such as ammonium sulphate or sodium chloride the value of κ is 0.53 and 1.12, respectively, whereas for secondary organic aerosols (SOAs) it typically ranges between 0.0 and 0.2 (Petters and Kreidenweiss, 2007). Using the parameter κ, and information about the hygroscopic behaviour of the pure chemical species, one can make a good first approximation of the water uptake characteristics of internally mixed particles.

Particles observed in remote areas are typically suspended in the atmosphere long enough to reach an internally mixed state through coagulation and condensation of gaseous species (Heintzenberg 1989). This is typically the case for the wider area of Eastern Mediterranean, and particularly the region over the Aegean Sea, during July and August when the prevailing northern winds (i.e., the Etesians) carry polluted air masses from central Europe, the Balkans (including Greece), and the Black Sea (Mihalopoulos et al., 1997; Lelieveld et al., 2002). The polluted air masses blend with

natural primary and secondary particles, resulting in increased particle concentrations commonly observed in the region (Salisbury et al, 2003).

Although information about the size, the concentration, and the integrated chemical composition of particles found over the southern Aegean region has been extensively reported in the literature (Koulouri et al., 2008; Kalivitis et al., 2008), high temporal resolution measurements of their hygroscopicity and/or chemical composition has been rather scarce (Pikridas et al., 2010). To the best of our knowledge, only Stock et al. (2011) have carried out measurements using a hygroscopic tandem differential mobility analyser (HTDMA) system at Finokalia on the island of Crete. During that study the observed hygroscopic growth factors of particles having dry mobility diameters of 50, 80 and 150 nm ranged from 1.12 to 1.59 when exposed at 90% relative humidity.

In this work we report high temporal resolution chemical composition and hygroscopicity measurements of particles in the atmosphere over the Aegean Sea. Chemical composition measurements of non-refractory fine aerosol particles were conducted using an airborne compact time-of-flight aerosol mass spectrometer (cToF-AMS) onboard the UK BAe-146-301 Atmospheric Research Aircraft, which was operated through the Facility for Airborne Atmospheric Measurement (referred to as the FAAM BAe-146 aircraft from this point onwards). Particle hygroscopicity measurements were performed by an HTDMA system located in the northern region of the Aegean Sea. Good closure between cToF-AMS and HTDMA measurements (agreement within ±5% uncertainty) was achieved when the aircraft flew in the vicinity of the ground station. Using the parameterisation from the closure study, we employ the cToF-AMS measurements to determine vertical profiles of the hygroscopic parameter κ_{mix} of the particles in the region.

2.2. Methods

2.2.1 Instrumentation

2.2.1.1 Airborne measurements

The airborne measurements involved a total of three flights from Crete to Lemnos and back with the FAAM BAe146 aircraft (cf. Tombrou et al., 2012). The cToF-AMS was operational in only two of these flights; namely flights b637 and

b641 performed on 1 and on 4 September, respectively. Detailed paths of these flights are shown in Fig. 2.1. In both cases the aircraft took off from Chania Airport, on Crete and headed east before turning north towards the island of Lemnos. The first flight took place from 09:00 to 13:45 UTC on 1 September. During that flight, the altitude of the aircraft was above 300 m on its way to Lemnos (eastern leg of the flight). To capture the vertical variation of the chemical composition of the particles along this path, the aircraft performed two missed approaches: one over the central Aegean Sea, and one over the island of Lemnos (Tombrou et al., 2012). The second flight took place from 11:13 to 15:38 UTC on 4 September. During that flight, the altitude of the aircraft along the leg from Crete to Lemnos (i.e., the part over the eastern Aegean Sea) was at lower altitude, almost constantly at 150 m above sea level (a.s.l.). The flight leg from Lemnos to Crete (i.e., the part over the western Aegean Sea) was in general at altitudes above 2.3 km during both flights, except for a small period during the second flight when the aircraft flew at 160 m a.s.l. on the southeast of Athens. Considering that the marine atmospheric boundary layer (MABL) was below 1 km, some parts of the flights were within and some above it.

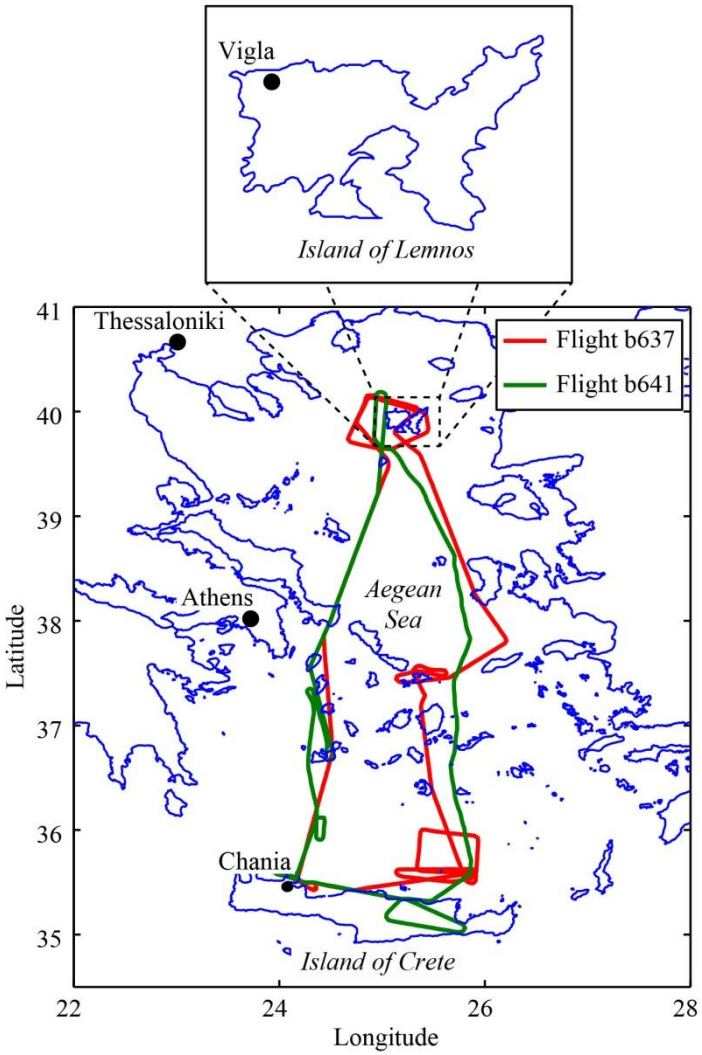

Fig. 2.1. Map of Greece showing the island of Lemnos and the location of the ground station at Vigla on the northwestern part of the island. The red and green lines show the paths followed by the FAAM BAe-146 aircraft on flights b637 and b641, performed on 1 and 4 September, respectively.

The non-refractory submicron chemical composition of the aerosol particles was determined by a cToF type (Canagaratna et al., 2007; Drewnick et al., 2005) AMS (Aerodyne Research Inc.) onboard the aircraft. Details of the airborne cToF-AMS instrument and the algorithm used for the analysis of the measurements are provided in Morgan et al. (2010). In brief, air was sampled through a Rosemount inlet (a forward facing, sub-isokinetic inlet with sampling efficiency close to unity for particles ≤ 600 nm; for more details cf. Foltescu et al., 1995), mounted on the aircraft fuselage. Inside the AMS an aerodynamic lens (Wang et al., 2005) was used for focusing the sampled particles onto the heated surface, which was maintained at 600 ˚C. The vapours resulting from volatilising the particles on the heated surface were then ionised using electron impact at 70 eV, and the ion fragments were analysed by a

quadruple mass spectrometer for specific ions, including NH_4^+, Cl^-, NO_3^-, SO_4^{2-} and organics. The cToF-AMS can measure particles having vacuum aerodynamic diameters (VADs) in the range from 50 to 700 nm (Liu et al., 2007), with a detection limit of ca. 50 ng m^{-3}.

The cToF-AMS was calibrated using monodisperse ammonium nitrate particles and the recorded measurements were analysed using the fragmentation table approach (Allan et al., 2003, 2004) with the modifications introduced by Aiken et al. (2008). Corrections for variations in the composition-dependent collection efficiency were applied according to the parameterisation introduced by Middlebrook et al. (2012).

2.2.1.2 Ground measurements

The ground-based hygroscopicity measurements were conducted at a station located 420 m a.s.l. in the area of Vigla, on the northwestern part of the island of Lemnos (39˚ 58' N, 25˚ 04' E; cf. Fig. 2.1). The area is far from any major city and from local anthropogenic sources. A custom-made HTDMA system (Rader and McMurry, 1986) and a commercially available scanning mobility particle sizer (SMPS, TSI Model 3034; Wang and Flagan, 1990) were used to measure the hygroscopic growth factor and the size distribution of the particles, respectively. For these measurements, ambient air was sampled through a 6-m long copper tube (ID = 26 mm) with a total flow rate of 30.0 lpm at atmospheric conditions. From this flow, 0.3 lpm were sampled by the HTDMA system and 1.0 lpm by the SMPS. A silica-gel diffusion drier was used upstream of the two systems in order to maintain the relative humidity (RH) of the sampled flow at 30±3 %. The SMPS system measured the particle size distribution from 10 to 487 nm, whereas the HTDMA measured the hygroscopicity of the particles having dry diameters from 50 to 170 nm.

The HTDMA system consisted of two differential mobility analysers (DMAs; Knutson and Whitby, 1975), and a condensation particle counter (CPC, TSI Model 3022A; Stolzenburg and McMurry, 1991). The first DMA (DMA-1, TSI 3080) included a ^{85}Kr aerosol neutraliser and a closed-loop system for recirculating the sheath flow. The second DMA (DMA-2) employed a custom-made system for the sheath flow recirculation with an RH controller (cf. Biskos et al., 2006a). For each measurement, the voltage on DMA-1 was adjusted to select dry aerosol particles

having mobility diameters from 50 to 170 nm. The quasi-monodisperse particles downstream of DMA-1 were conditioned within a single Nafion-tube humidity exchanger (Perma Pure Model MD-110) to a constant RH of 85 %. The size distribution of the humidified particles was then measured by DMA-2 and the CPC. The aerosol and the sheath flows for both DMAs were 0.3 and 3.0 lpm, respectively.

The RH and temperature of the aerosol flow downstream the humidity exchanger and of the sheath flow in DMA-2 were measured by two humidity/temperature sensors (Rotronic Model SC-05). A proportional-integral-derivative (PID) controller was used to control the RH in both flows by adjusting the flow of a parallel stream of very high RH (ca. 100 %) on the outer annulus of each Nafion-tube humidity exchanger. The overall performance of the HTDMA was tested with ammonium sulfate and sodium chloride particles produced by atomisation. The uncertainty of the particle size measurements by the system was less than 1 % whereas RH variations were within less than 2 % of the set point.

2.2.2. Data Analysis

2.2.2.1. SMPS Measurements

The inversion of the SMPS measurements was performed using the Aerosol Instrument Manager software (AIM, TSI version 6.0), including correction for multiply charged particles. The inverted particle-number size distributions were then analyzed using a curve-fitting algorithm similar to that described in Hussein et al. (2005). This algorithm employed the least squares method to fit the sum of up to three lognormal distributions to the measurements. The first lognormal distribution corresponded to particles having a geometric mean mobility diameter from 10.0 to 25.0 nm (nucleation mode), the second from 25.1 to 90.0 nm (Aitken mode), and third from 90.1 to 500.0 nm (accumulation mode). The geometric standard deviation of each lognormal distribution was allowed to vary between 1.2 and 2.1. The algorithm starts by fitting a tri-modal lognormal distribution to the measurements, and successively tests the possibility of reducing it to a bi- or to a uni-modal distribution based on the estimated number concentration of each mode, the geometric mean diameter, and the geometric standard deviation of the neighbouring modes.

2.2.2.2. HTDMA Measurements

The hygroscopic growth factor, *g*, determined by the HTDMA measurements is given by:

$$g(\mathrm{RH})=\frac{d_m(\mathrm{RH})}{d_{m,dry}}, \quad (2.1)$$

where d_m(RH) and $d_{m,dry}$ are the geometric mean mobility diameters of the sampled particles at the hydrated state (i.e., RH = 85%) measured by DMA-2 and the CPC, and at the dry state, i.e., the mobility diameter selected by DMA-1, respectively. The RH at the inlet of DMA-1 varied between 27 and 33%, having an average value of 30% during the entire period of the measurements. As a result the measured growth factor can be more accurately expressed as:

$$g(85\%|30\%)=\frac{d_m(85\%)}{d_m(30\%)}. \quad (2.2)$$

Here d_m(30%) is the nominal mobility diameter of the particles selected by DMA-1, and d_m(85%) is the mobility diameter measured by DMA-2 and the CPC of the HTDMA system.

Internally mixed monodisperse particles of uniform chemical composition will grow to the same size when subjected to identical RH conditions downstream of DMA-1. In this case, the size distribution of the humidified monodisperse particles can exhibit a single mode that is significantly broadened compared to that of the dry sample, or distinct monodisperse modes, depending on the hygroscopic variability of the particles.

To distinguish between modes that may correspond to different particle populations in a systematic way we employed the TDMAfit algorithm (Stolzenburg and McMurry, 1998) for inverting the HTDMA measurements. The algorithm uses the least squares method to fit Gaussian-shaped transfer functions to the measured response of the system. To locate the peak positions and the associated concentrations that give the best fit, the algorithm employs a search routine that is based on a number of convergence criteria and constrains. When a chi-square function of the fit residual changes by less than 0.1% and each of the fitted parameters alters by less than 10% of its respective estimated uncertainty, the TDMAfit is considered to have converged to the best fit. Measurements inverted also by the TDMAinv algorithm developed by Gysel et al. (2009) gave hygroscopic growth factors that agreed within less than ± 2.5% with those calculated by TDMAfit.

For the analysis of the HTDMA measurements, we assumed that all the particles have a spherical shape when selected by DMA-1, and that particle shrinkage

due to the presence of volatile species, (e.g. ammonium nitrate) was negligible. Under these assumptions, the measured hygroscopic growth factors less than 1.0, comprising ca. 3% of all the measurements, were excluded.

2.2.2.3. Determining hygroscopic growth factors from the AMS measurements

The hygroscopic growth factor of internally mixed particles, g_{mix}, can be estimated using the AMS measurements as (Kreidenweis et al., 2008)

$$g_{mix}\,(\mathrm{RH}) = \left(1 + \kappa_{mix}\left(\frac{a_w}{1-a_w}\right)\right)^{1/3}, \tag{2.3}$$

where a_{w} is the water activity of the solution droplet, which neglecting the Kelvin effect is equal to RH/100, and κ_{mix} is the hygroscopic parameter of the mixed particles given by

$$\kappa_{mix} = \sum_i \varepsilon_i \kappa_i. \tag{2.4}$$

Here $\varepsilon_i = V_{si}/V_{\mathrm{s}}$ and κ_i are the volume fraction and the hygroscopic parameter of the *i*th chemical species of the particles, with V_{si} being the volume occupied by that species, and V_s the dry volume of the particle.

To estimate the volume fractions of each species of the particles from the cToF-AMS measurements we first determined the molar fractions of the ions and the then those of the chemical compounds comprising the particles using the ion pairing algorithm proposed by Pilinis et al. (1987) and later simplified by Gysel et al. (2007). In this simplified algorithm by setting the fraction of nitric acid to zero, the molar fraction of ammonium nitrate is equal to the molar fraction of nitrate ions. The rest of the ammonium ions are assigned to the sulfate ions, and depending on the ammonium to sulfate ratio, the molar fractions of sulfuric acid, ammonium bisulfate and ammonium sulfate are determined. To convert the mole fractions to volume fraction we used the bulk densities for every chemical species as summarized in Table 1 (Duplissy et al., 2011). The respective hygroscopic parameters are also shown in Table 1 (Petters and Kreidenweis, 2007). For the organic compounds commonly present in atmospheric particles, the density, ρ_{org}, and hygroscopic parameter, κ_{org}, can vary from 1200 to 1700 kg m^{-3} (Hallquist et al., 2009), and from 0.0 to 0.2 (Petters and Kreidenweis, 2007), respectively.

Table 2.1. *Hygroscopic parameters k* and densities used in the k-Köhler theory (Eq. 2.3).

Chemical species	κ	Density (kg m^{-3})
$(NH_4)_2SO_4$	0.53[a]	1769[b]
NH_4HSO_4	0.56[a]	1720[b]
NH_4NO_3	0.68[a]	1780[b]
H_2SO_4	0.97[d]	1830[b]
Organics	0.00-0.20[b]	1200-1700[c]

[a] Petters and Kreidenweis (2007);

[b]Duplissy et al. (2011);

[c]Hallquist et al. (2009);

[d]Biskos et al. (2009).

2.3. Results and Discussion

The prevailing synoptic conditions during the entire period of the measurements correspond mainly to north easterlies surface winds over the Aegean Sea, being associated with a large-scale surface anticyclone. From 30 August to 3 September, however, the wind speeds were substantially lower with northwesterly directions. In particular, during the flight performed on 1 September (flight b637), a large-scale surface anticyclone prevailed over southeastern Europe, producing fair weather conditions and a moderate flow from the north-east sector over the Aegean Sea. During the flight performed on 4 September (flight b641), the low pressure pattern that prevailed over southeastern Europe, in combination with the anticyclone over Balkans, resulted in a strong channeled surface-wind flow over the Aegean Sea. Average wind speeds of up to 20 m s^{-1} were measured at altitudes 150 m a.s.l, but diminished above 4.5 km. When the aircraft flew in the vicinity of the station on Lemnos, the surface winds were from southwest direction and lower than 5 m s^{-1} during the first flight, and from northeast directions with speeds ranging from 9.5 to 13 m s^{-1} during the second flight. The surface temperature and RH at the ground station on Lemnos during the two missed approaches were 28 and 21˚C, and 45 and 75 %, respectively. For the entire period of the measurements, the surface temperature and the RH at the ground station ranged from 17.7 to 29.6 ˚C and from 16 to 87 %, respectively.

2.3.1. Measurements in the Atmosphere over the Ground Station

As described in Sect. 2.1, the size distributions and the hygroscopicities of the particles were continuously measured at the ground station during the entire period of the campaign. During each flight, the FAAM BAe146 aircraft flew in the vicinity of the ground station (i.e., ± 300 m above or below the station and within a radius of 30 km) for approximately 10 to 15 min. The measurements performed by the airborne cToF-AMS during these two time windows were used to check the closure between hygroscopicity and chemical composition measurements. The following paragraphs provide an overview of the ground-based measurements and the closure study.

2.3.1.1. Particle Size Distributions

The evolution of the 1 h averaged particle size distributions measured by the SMPS, together with time series of the number concentration of particles having dry mobility diameters in the ranges of 50–80, 80–100 and 100–170 nm, for all the days of the experiment are shown in Fig. 2.2. The total number concentration of the particles having diameters from 10 to 487 nm varied from ca. 4×10^2 to 1.0×10^4 particles cm^{-3} with median value of 1.9×10^3. Almost 72.1% of the samples exhibited bi-modal distributions, whereas 12.4% and 13.7% of them showed uni-modal and tri-modal distributions, respectively. The total particle number concentration in the nucleation mode varied from 1.7×10^2 to 3.2×10^3 particles cm^{-3}, with a median value of 7.7×10^2, in the Aitken mode from 1.7×10^2 to 7.1×10^3 particles cm^{-3}, with a median value of 1.0×10^3, and in the accumulation mode from 1.8×10^2 to 3.4×10^3 particles cm^{-3}, with a median value of 9.9×10^2. Most often the particles were observed in the Aitken and the accumulation modes during the entire period of the measurements. Particle size distribution measurements over the region of the Aegean Sea are only available for the station of Finokalia on Crete (Pikridas et al., 2010). According to that study, the average total number concentration of particles having mobility diameters from 10 to 500 nm was ca. 2.7×10^3 particles cm^{-3}, which is very similar to the concentrations measured on Lemnos. From 30 August to 3 September, the majority of the particles resided in the accumulation and the Aitken modes. The rest of the period was characterised by wider size distributions with particles residing also in the nucleation mode (i.e., particles having diameter smaller than 25 nm). This pattern is well correlated with the variability in the origin of the air masses arriving at the station (cf. discussion in Sect. 2.3.2 and back-trajectory calculations shown in Fig. S2.1).

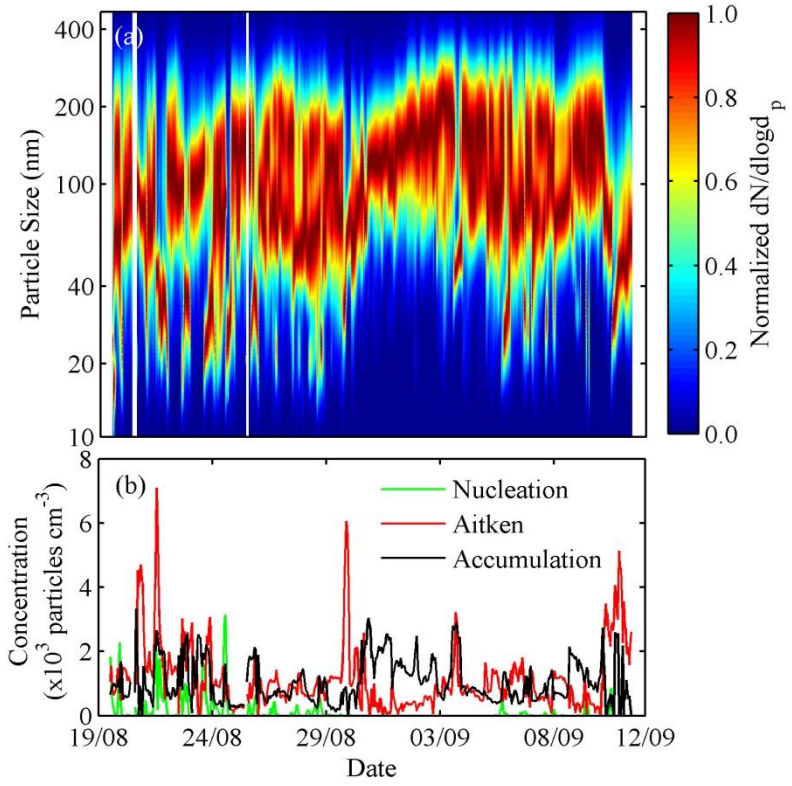

Fig. 2.2. Evolution of normalised, hourly averaged size distributions of particles having dry mobility diameters from 10 to 487 nm (**a**), and temporal variation of the respective number concentration of particles residing in the nucleation, Aitken and accumulation modes (**b**) throughout the whole period of the Aegean-Game field campaign.

2.3.1.2. Particle Hygroscopicity

Characteristic raw measurements by the ground-based HTDMA are shown in Fig. 2.3. The recorded size distributions correspond to particles having dry mobility diameters (i.e., diameters selected by DMA-1) of 70, 90, and 150 nm after being exposed to 85 % RH. The respective hygroscopic growth factors *g*(85%|30%) of those samples are 1.22, 1.22, and 1.21. In almost all the HTDMA measurements, the geometric standard deviation of the size distribution of the humidified particles was similar to that of the dry ones, indicating that the samples were internally mixed. This is expected in remote areas with no major local anthropogenic particle sources.

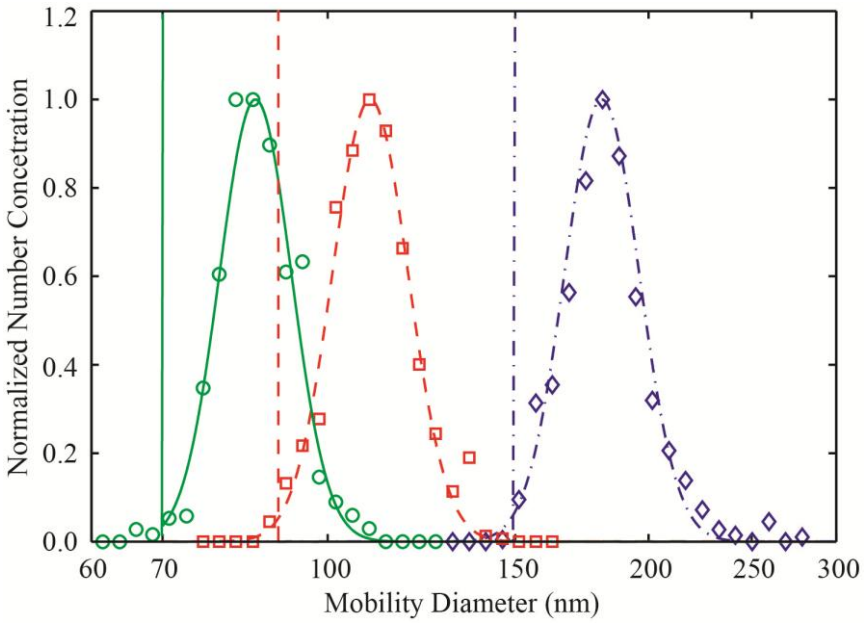

Fig. 2.3. Size distribution measurements of the humidified monodisperse particle samples recorded by the HTDMA system. Particles having dry mobility diameters of 70 (green), 90 (red), and 150 nm (blue) selected by DMA-1 at 30 ± 3 % RH were exposed to 85 % RH and measured by DMA-2 and the CPC. Symbols represent the actual measurements and lines the fitted curves determined by the TDMAFIT algorithm. One hygroscopic mode is observed in all the measurements, corresponding to growth factors of 1.22, 1.22 and 1.21, for the 70-, 90- and 150-nm dry particles, respectively.

Figure 2.4 shows the hygroscopic growth factors $g(85\%|30\%)$ measured by the HTDMA (Fig. 2.4a) together with the measured (SMPS data) number concentrations of the particles having dry diameters in the ranges selected by DMA-1 (Fig. 2.4b) during the entire period of the campaign. The measurements are grouped in three different classes depending on the dry mobility diameters selected by DMA-1: green circles and curve correspond to measurements of particles having dry mobility diameter from 50 to 80 nm, red squares and curve from 80 to 100 nm, and blue diamonds and curve from 100 to 170 nm. Note that although the dry diameter was selected to be close to the peak of the most dominant mode of the particle size distribution as measured by the SMPS, measurements of dry particles in other modes were randomly sampled to investigate potential differences in their hygroscopicity. For the Aitken (19 % of the samples) and accumulation (81 % of the samples) mode particles, the average growth factors were 1.18 (ranging from 1.00 to 1.56) and 1.21 (ranging from 1.00 to 1.59), respectively. The average growth factor for all particle sizes was 1.20, having a minimum value of 1.00 and a maximum of 1.59. Periods with particles of high (from 25 to 30 August), low (from 30 August to 2 September) and

moderate (from 2 to 9 September) variation in the growth factor can be identified in the HTDMA measurements. This difference is well correlated with the variability in the origin of the air masses arriving at the station. During the days with the low variation in particle hygroscopicity, the air masses reaching the station had almost the same origin (i.e., the Black Sea), as indicated in Fig. S2.1 in the Supplement.

Although the selected dry diameters correspond to different periods during the campaign, they exhibit very similar growth factors when comparing nearby measurements. Considering also that the variability and the average growth factors corresponding to particles having different dry diameters are also very similar, in most of the cases, suggests that there is no noticeable variation of chemical composition as a function of particles size. It should also be pointed out that the selected dry particles had diameters in the range from 50 to 170 nm, within which the contribution of the Kelvin effect to the hygroscopic growth of the particles is negligible (Biskos et al., 2006b; Park et al., 2009).

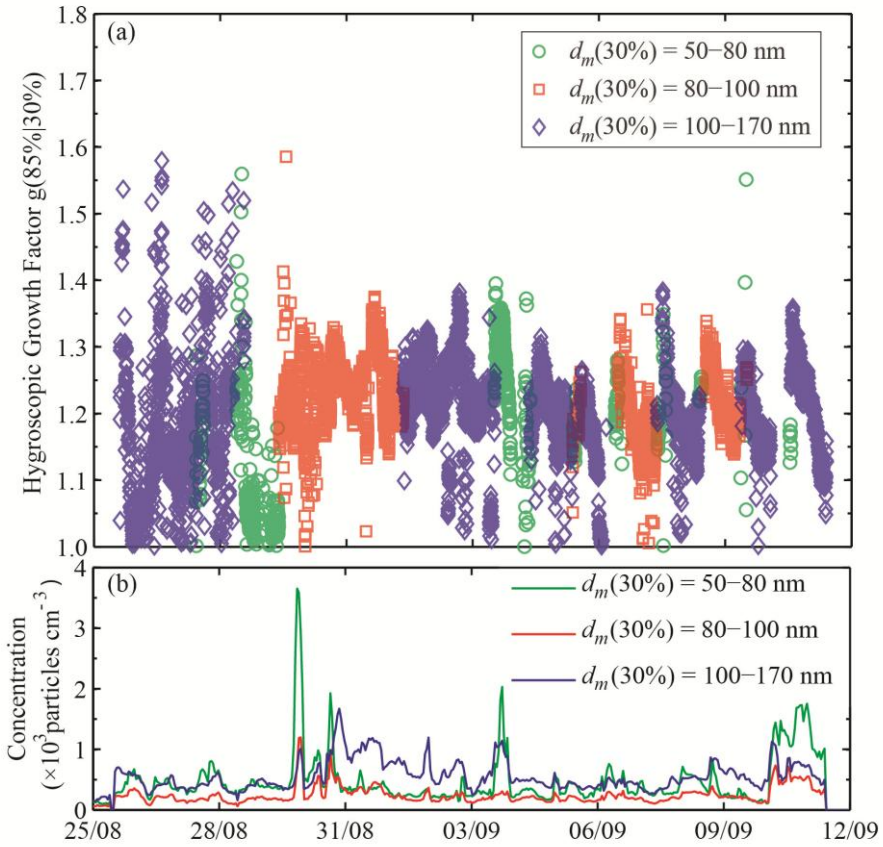

Fig. 2.4. Time series of the hygroscopic growth factors of atmospheric aerosol particles measured with the HTDMA (**a**) and number concentrations of the particles having dry mobility diameters in the ranges sampled by the HTDMA (**b**) at the ground station on Lemnos island. Aerosol particles are grouped in three different regions based on their dry mobility diameters: from 50 to 80 nm (green circles and

curve), from 80 to 100 nm (red squares and curve), and from 100 to 170 nm (blue diamonds and curve).

The average hygroscopic growth factor measured in our work is ca. 12 % lower compared to those reported by Stock et al. (2011), who also employed an HTDMA system at Finokalia, on the island of Crete, from 12 August to 20 October 2005. The hygroscopic growth factors of particles having dry diameters 50, 80, and 150 nm observed during that study ranged from 1.12 (nearly hydrophobic particles) to 1.59 (more hygroscopic particles). Considering that those HTDMA measurements were conducted at 90 % RH using the κ-Köhler theory (i.e., Eqs. 2.3 and 2.4), we calculate the corresponding growth factors at 85 % RH to be in the range from 1.08 to 1.43. Although this range is similar to that observed in our study, the occurrence frequency of the more hygroscopic particles reported by Stock et al. (2011) was significantly higher (of the order of 84 to 90 %) compared to that in our study (i.e., ca. 35 %).

2.3.1.3. Particle Chemical Composition and Hygroscopicity

Figure 2.5 shows the chemical composition of the atmospheric particles when the aircraft was flying within a 30-km radius from the ground station and between 100 and 700 m altitude (i.e., ca. ± 300 m from the altitude of the ground station). The reported volume fractions are estimated by applying the ion pairing algorithm (cf. sect. 2.2.2.3) to the cToF-AMS measurements. The organic species comprised almost 50% of the total particle dry volume, whereas ammonium sulfate and ammonium bisulfate accounted for the rest. Although the volume fraction of the organic species was similar during both days, the inorganic fraction of the particles was more acidic during the flight on 1 September (Fig. 2.5a). Considering that during both flights the chemical composition of the particles did not show high variability with size (data not shown), the cToF-AMS measurements can be considered as representative for the entire particle size range and therefore can be used to predict the hygroscopic growth of the particles using the κ-Köhler theory.

The comparison between predicted (i.e., using Eqs. (2.3) and (2.4) and the cToF-AMS measurements) and measured (i.e., using Eq. (2.2) and the HTDMA measurements) hygroscopic growth factors is shown in Fig. 2.6. The particles measured by the HTDMA had dry mobility diameters of 100 nm. To account for the fact that the relative humidity of the dry sample was 30 %, and therefore the particles

entering the HTDMA may have already had some water due to their acidity (cf. Biskos et al. 2009; Engelhaart et al. 2011), and/or their organic content (c.f. Marcolli et al., 2004), we calculate the absolute growth factor at 85% RH as

$$g(85\%)=\frac{d_m(85\%)}{d_{m,dry}}=\frac{d_m(30\%)}{d_{m,dry}}\times\frac{d_m(85\%)}{d_m(30\%)}=g(30\%)\times g(85\%|30\%). \quad (2.5)$$

Here $g(85\%|30\%)$ is the measured growth factor (cf. Eq. 2.2), and $g(30\%)$ is the growth factor of the particles entering the HTDMA at 30% RH. The latter is estimated using the κ-Köhler theory and the composition measurements provided by the cTOF-AMS. The estimated $g(30\%)$ values varied from 1.03 to 1.06 during the specific measurements.

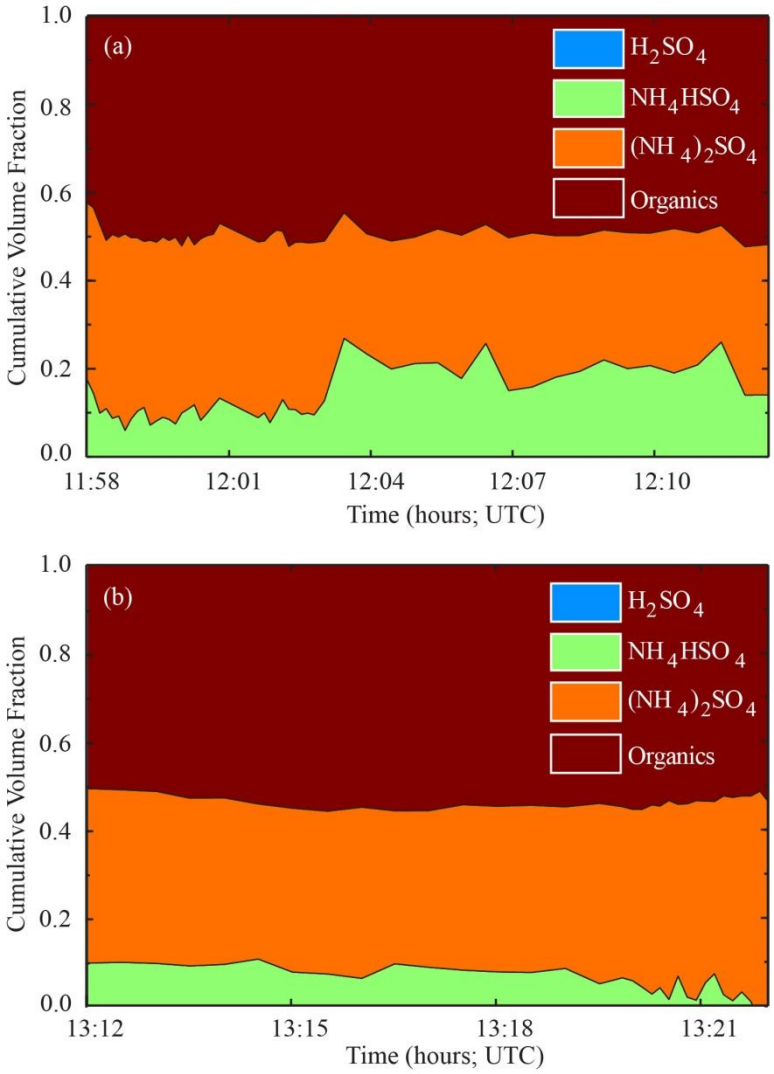

Fig. 2.5. Cumulative volume fractions of the chemical species comprising the particles in the atmosphere over the ground station on Lemnos island during the flights performed on 1 September (flight b637) (**a**) and on 4 September (flight b641) (**b**). The volume fractions are estimated by the ion pairing algorithm and the chemical composition measurements from the airborne cToF-AMS.

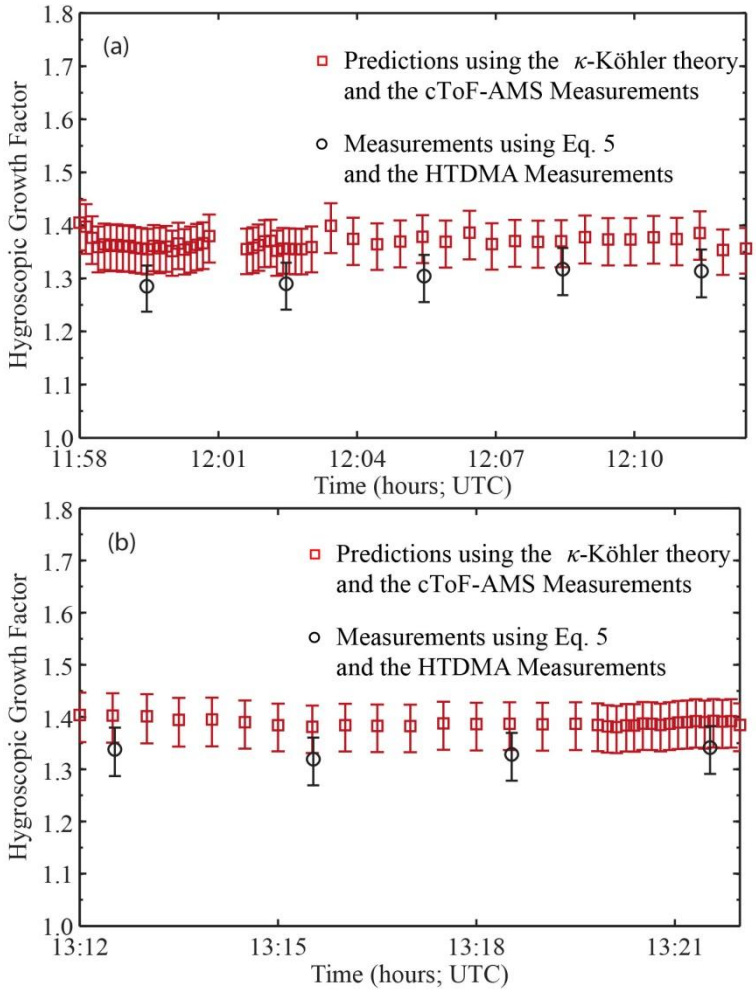

Fig. 2.6. Hygroscopic growth factors measured by the HTDMA (black dots) and predicted by κ-Köhler theory using the chemical composition measurements from the airborne cToF-AMS (red squares) when the aircraft was flying close to Vigla station on 1 (flight b637) September 2011 (**a**) and on 4 (flight b641) (**b**) September 2011. The HTDMA growth factors correspond to particles having dry mobility diameter of 100 nm, whereas the chemical composition corresponds to particles having Vacuum Aerodynamic Diameters (VADs) in the range 50–700 nm. Error bars represent the 2 % uncertainty in the RH measurements.

For the predicted growth factors shown in Fig. 2.6, we used the fixed κ and ρ values for the inorganic species shown in Table 2.1. The values of κ_{org} and ρ_{org} were determined as follows. By keeping κ_{org} = 1200 kg m^{-3} (i.e., the lowest density of organic species as indicated from the literature; cf. Hallquist et al., 2009), we increased κ_{org} from 0 up to the value that the predicted hygroscopic growth factors agreed with the measured ones within 5 %. In a similar manner, we increased ρ_{org} from 1200 kg m^{-3} by keeping κ_{org} = 0. From the resulting ranges of κ_{org} and ρ_{org}, we

used the mean values as the most representative for each day. Following this procedure we estimated κ_{org} = 0.03 and ρ_{org} = 1300 kg m^{-3} during the flight on 1 September, and κ_{org} = 0.1 and ρ_{org} = 1400 kg m^{-3} during the flight on 4 September. Evidently, the organic fraction of the particles observed during the closure on 4 September was more hygroscopic and slightly more dense compared to that on 1 September. In either case, the organic fraction of the particles was far less hygroscopic than the inorganic fraction, resulting in a reduction of the amount of water they could uptake as compared to their pure inorganic counterparts.

2.3.2. Measurements in the Atmosphere over the Aegean Sea

In the paragraphs that follow we provide an overview of the cToF-AMS chemical composition measurements conducted over the Aegean Sea during the two flights of the campaign, and employ them to predict the representative hygroscopic parameter of the particles using the κ-Köhler theory.

3.2.1. Particle Chemical Composition

The volume fractions of the compounds comprising the particles observed during the entire flights on 1 and 4 September are shown in Figs. 2.7 and 2.8, respectively. During the flight on 1 September (data shown in Fig. 2.7) the volume fraction of sulfuric acid, ammonium bisulfate, and ammonium sulfate ranged from zero to 0.86 with a median value of zero; from zero to 0.66 with a median value of 0.22, and from zero to 1.00 with a median value of 0.31; respectively. In two of the four vertical paths of the flight (i.e., above the central Aegean Sea and above the island of Lemnos), the acidity of the particles appeared to increase with increasing height, indicating that the concentration of ammonia was very low at high altitudes, as had been observed in other regions (e.g. Spengler et al., 1990). The volume fraction of ammonium sulfate was almost zero at lower altitudes, rising to 0.5 at 2.5 km a.s.l. This pattern was inverted in the two vertical paths above Crete. The volume fractions of ammonium bisulfate in this case were high at lower altitudes (<700 m a.s.l.) and, with the exception of a couple of points (one around 2.0 and one 3.7 km a.s.l.), decreased with increasing height. In all cases, the concentration of H_2SO_4 was almost zero for the entire flight, with the exception of a few measurements higher than 4.0 km a.s.l. over Crete.

As shown by back trajectory calculations (cf. Fig. S2.2), low-altitude air masses arriving over the north or central Aegean Sea originated from eastern Europe and the wider Black Sea region. These air masses appeared to carry particles of very low acidity, as shown in Fig. 2.7. The low-altitude air masses arriving over Crete, on the other hand, originated either from the marine environment or from the mainland, but in both cases they passed over the wider Athens region. This can explain the high acidity of the particles observed at lower altitudes in that area. Acidic particles formed or directly emitted from anthropogenic activities in the region of Athens travelled over the central Aegean Sea towards Crete. The acidity of these particles did not change significantly during advection as a result of the low concentrations of ammonia over the marine environment (Clarisse et al., 2009). Acidic particles coming from eastern Europe (i.e., those arriving over the north Aegean Sea) have a greater chance of being neutralised due to the higher concentration of ammonia over the mainland.

The organic volume fraction of the particles observed during the flight conducted on 1 September ranged from zero to 0.74, with a median value of 0.46. Their vertical variability during all four vertical parts of the flight was similar, starting with low values at the lower altitudes, increasing at intermediated heights and decreasing again at even higher levels. The height of the layers with particles of high organic fractions differed from place to place, with the highest layer observed over the central Aegean Sea. Considering that the air masses arriving over Lemnos and the central Aegean Sea during the respective missed approaches have passed over urban, rural and marine environments, and that their origin was similar (i.e., from eastern Europe), the organic fraction of the particles could be either biogenic or anthropogenic.

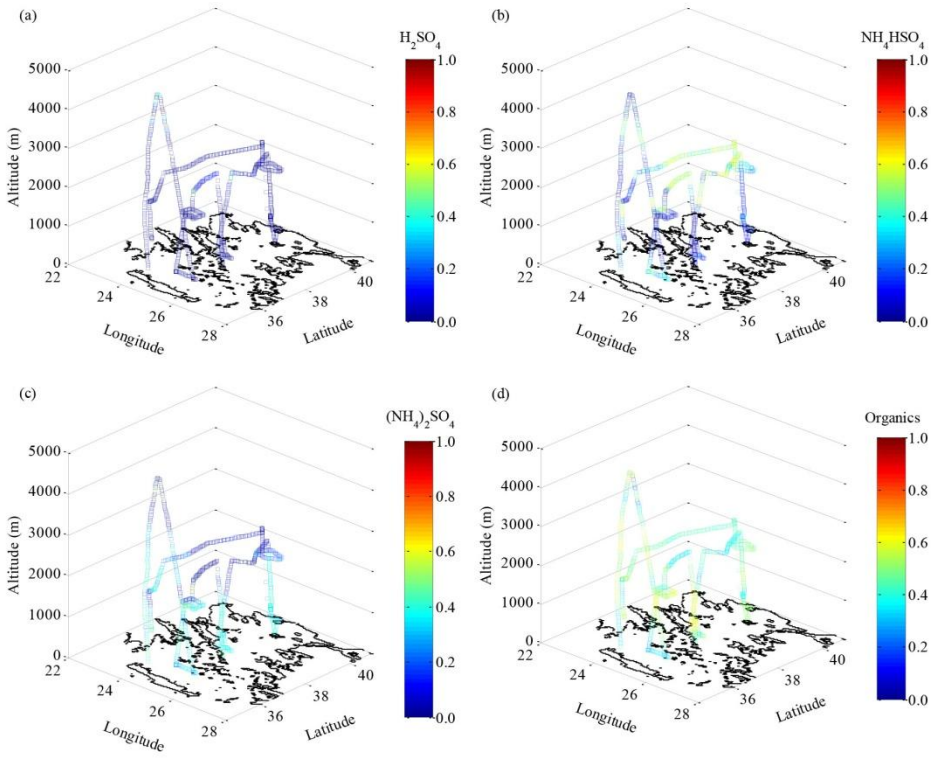

Fig. 2.7. Composition of the non-refractory compounds measured by the cToF-AMS during the flight performed on 1 September 2011 (flight b637) over the Aegean Sea. The reported volume fractions for H_2SO_4 (**a**), NH_4HSO_4 (**b**), $(NH_4)_2SO_4$ (**c**) and organic matter (**d**) are estimated using the mole fractions determined by the cToF-AMS measurements and the simplified ion pairing algorithm proposed by Gysel et al. (2007).

The chemical composition of the particles observed during the flight on 4 September is shown in Fig. 2.8. During that flight the aircraft flew at lower altitudes from Crete to Lemnos (eastern leg of the flight) and at higher altitudes from Lemnos to Crete (western leg of the flight). Three of the four vertical parts of the flight in this case ended at substantially higher altitudes (ca. 4.0 km a.s.l.) compared to those of the first one. The vertical part of the flight over the central Aegean Sea was limited to ca. 1.0 km. The volume fraction of sulfuric acid, ammonium bisulfate, and ammonium sulfate ranged from zero to 0.79, with a median value of zero; from zero to 0.69, with a median value of 0.10; and from zero to 0.97, with a median value of 0.35; respectively. Similarly to the measurements recorded during the flight on 1 September, particle acidity increased with increasing altitude. In this case, however, the particles observed at ca. 2.5 km a.s.l. (i.e., similar to the altitude of the eastern leg of the first flight) were even more acidic, having a H_2SO_4 volume fraction that reached values as high as ca. 0.4. High volume fractions of NH_4HSO_4 were observed at a layer between 1.0 and 2.0 km a.s.l. over the west/northwest of Crete.

The respective fractions for the organic compounds of the particles during the flight conducted on 4 September ranged from 0.03 to 0.84, with a median value of 0.48. An increasing particle organic content is observed with increasing altitude, having median volume fractions of 0.44 and 0.54 for altitudes below and above 2.0 km, respectively. Compared to the flight on 1 September, the vertical distributions of the second flight (i.e., 4 September) exhibited a higher uniformity. This can be explained by the fact that the air masses arriving in many regions over the study area all originated from central/western Europe and followed similar paths (cf. Fig. S2.3 in the Supplement).

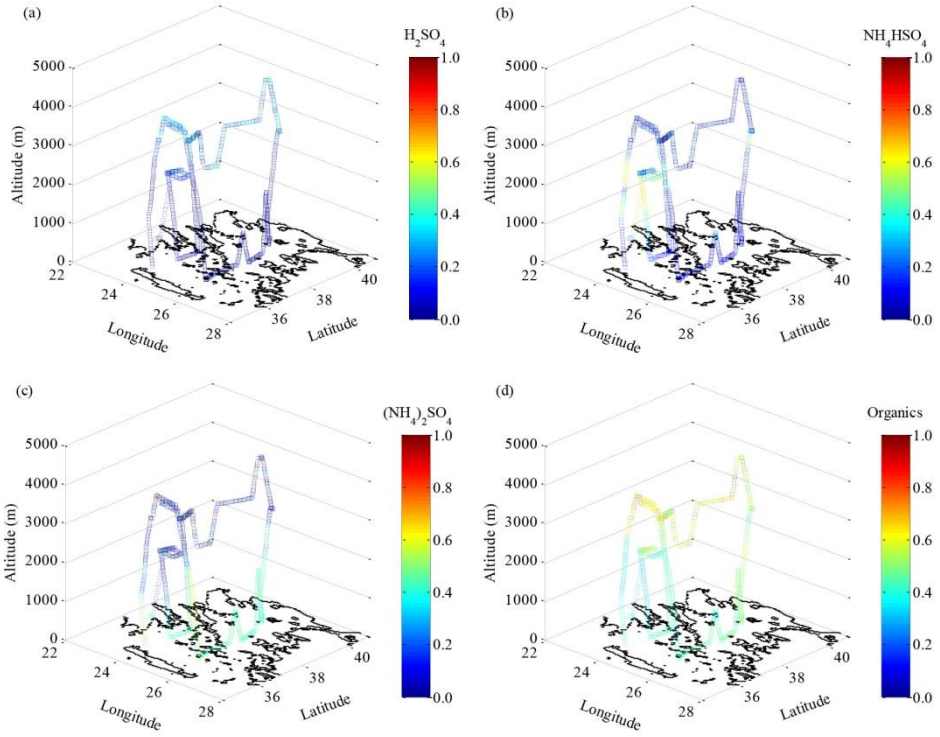

Fig. 2.8. Composition of the non-refractory compounds measured by the cToF-AMS during the flight performed on 4 September 2011 (flight b641) over the Aegean Sea. The reported volume fractions for H_2SO_4 (**a**), NH_4HSO_4 (**b**), $(NH_4)_2SO_4$ (**c**) and organic matter (**d**) are estimated using the mole fractions determined by the cToF-AMS measurements and the simplified ion pairing algorithm proposed by Gysel et al. (2007).

2.3.2.2. Particle Hygroscopicity

Using the bulk chemical composition measurements discussed above, we calculated vertical profiles of the aerosol hygroscopic parameter κ_{mix} (Eq. 2.4) during the two flights (cf. Figs. 2.9 and 2.10). For these calculations we used the hygroscopic parameters and the densities of the organic fraction of the particles derived from the

closure study (i.e., κ_{org} = 0.03, ρ_{org} = 1300 kg m^{-3} and κ_{org} = 0.1, ρ_{org} = 1400 kg m^{-3} for the flights conducted on 1 and 4 September, respectively; cf. Sect. 2.3.1.3 and Fig. 2.6), and assumed that all the samples were internally mixed. During the flight on 1 September (Fig. 2.9), the hygroscopic parameter ranged from 0.19 to 0.84, with a median value of 0.31. The hygroscopic parameter κ_{mix} within the MABL (i.e., up to 1 km a.s.l.) exhibited a decreasing trend with increasing altitude over the southern and central Aegean Sea (Fig. 2.9a–c). At higher altitudes κ_{mix} showed a noticeably higher variability, with values ranging from 0.21 at lower altitudes to 0.84 at altitudes above 4 km where the particles were highly acidic. The vertical variability of κ_{mix} over the northern Aegean Sea was significantly lower, having values that ranged from 0.19 to 0.38. Overall, the hygroscopic parameter κ_{mix} below the MABL was higher over the southern Aegean sea due to the influence of air masses arriving from the wider Athens region, as described in Sect. 2.3.2.1.

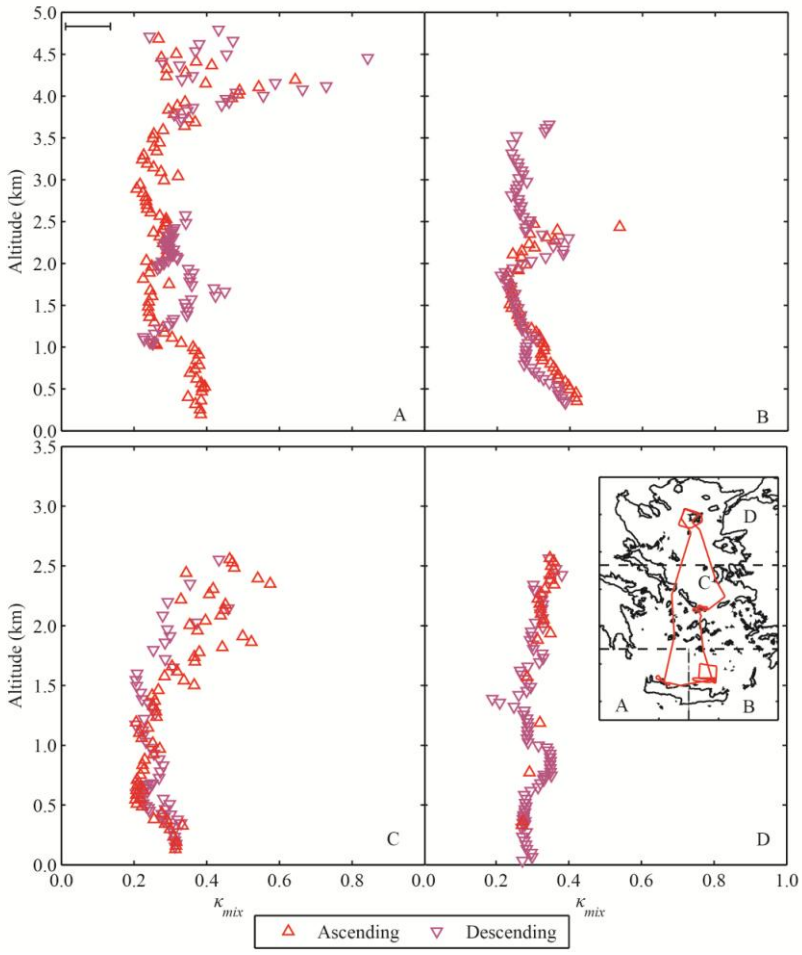

Fig. 2.9. Vertical profiles of the estimated hygroscopic parameters κ_{mix} of aerosol particles observed over southwestern (**a**) southeastern (**b**), central (**c**) and northern (**d**) Aegean Sea, during ascends (up triangles) and descends (down triangles) performed on the flight of 1 September 2011 (flight b637).

The inset shows the locations corresponding to the vertical profiles of κ_{mix} shown in the different subplots. The hygroscopic parameters are calculated using the κ-Köhler theory (Eq. 2.3) and the bulk chemical composition measurements from the airborne cToF-AMS. For the calculations we assumed that the particles were internally mixed, and that all the organic species had κ_{org} = 0.03 and ρ_{org} = 1300 kg m^{-3}. The error bar represents the spread of the estimated κmix values when adopting the level of uncertainty used in our closure study.

The vertical profiles of the hygroscopic parameters predicted for the flight on 4 September are shown in Fig. 2.10. In this case, the calculated κ_{mix} values ranged from 0.22 to 0.80, with a median value of 0.36, which is comparable to that calculated for the first flight. However, the vertical variability of κ_{mix} for altitudes even up to 2–3 km was significantly lower compared to that observed during the first flight. The median value of κ_{mix} was of the order of 0.3 for the whole region as a result of the low acidity (i.e., the inorganic fraction of the particles was mostly ammonium sulfate) and relatively low organic volume fractions of the particles. The variability of κ_{mix} was higher at higher altitudes, with values reaching up to 0.80. This increase is explained by the increasing acidity of the particles, i.e., their higher volume fraction of sulfuric acid with increasing altitude, as shown in Fig. 2.8a.

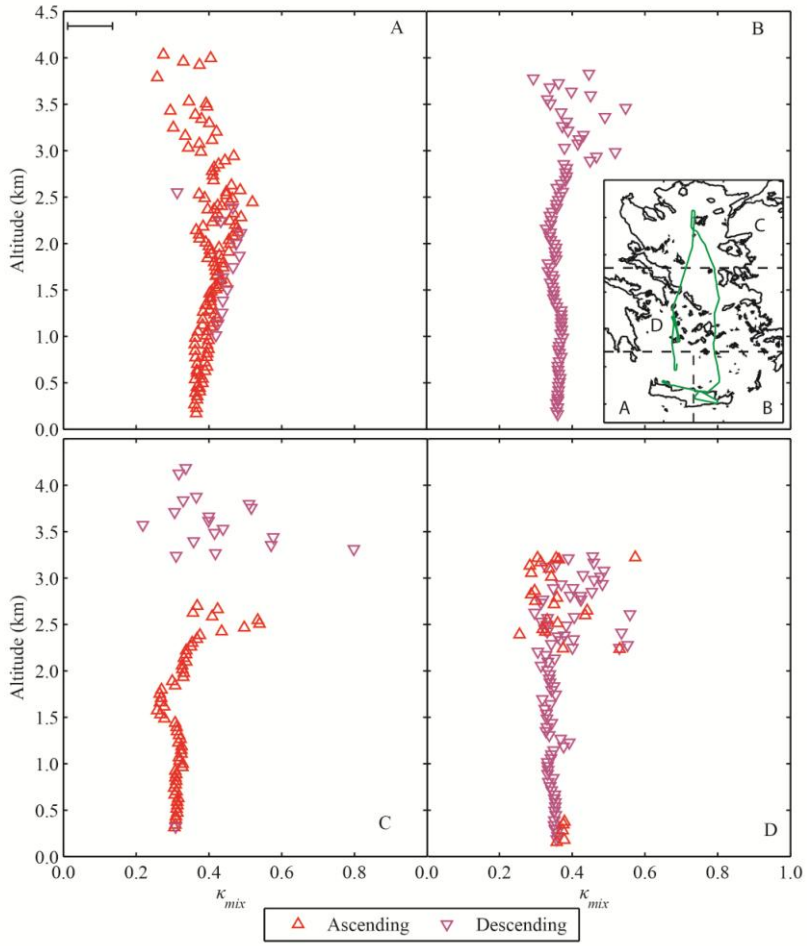

Fig. 2.10. Vertical profiles of the estimated hygroscopic parameters κ_{mix} of aerosol particles observed over southwestern (**a**) southeastern (**b**), central (**c**) and northern (**d**) Aegean Sea, during ascends (up triangles) and descends (down triangles) performed on the flight of 4 September 2011 (flight b641). The inset shows the locations corresponding to the vertical profiles of κ_{mix}, shown in the different subplots. The hygroscopic parameters are calculated using the κ-Köhler theory (Eq. 2.3) and the bulk chemical composition measurements from the airborne cToF-AMS. For the calculations we assumed that the particles were internally mixed, and that all the organic species had $\kappa_{org} = 0.1$ and $\rho_{org} = 1400$ kg m^{-3}. The error bar represents the spread of the estimated κ_{mix} values when adopting the level of uncertainty used in our closure study.

Despite that the measurements are performed in a marine environment of the Aegean Sea, the estimated median κ_{mix} values, during both flights, reside well within the range measured in urban and rural regions (Wex et al., 2010) and modelled for continental Europe (Pringle et al., 2010).

2.4. Conclusions

Measurements of the chemical composition and hygroscopicity of atmospheric particles were conducted over the region of the Aegean Sea using a cToF-AMS

onboard the FAAM BAe-146 aircraft, and a ground-based HTDMA system located on a remote station on the island of Lemnos. The HTDMA measurements showed that the mean hygroscopic growth factor of particles having dry diameters from 50 to 170 nm was ca. 1.2, and that the aerosol samples were internally mixed during the entire period of the campaign. Good closure between cToF-AMS and HTDMA measurements was achieved when the aircraft flew in the vicinity of the ground station. For these cases, the most representative values of κ_{org} and ρ_{org} were respectively 0.03 and 1300 kg m^{-3} for the flight on 1 September (b637), and 0.10 and 1400 kg m^{-3} for the flight on 4 September (b641).

The particles observed over the wider region of the Aegean Sea during the two flights exhibited high variability in their acidity and organic volume fraction, which can be attributed to differences in the origin of the air masses arriving in the region. During the flight conducted on 1 September, the air masses arriving over the northern and central Aegean Sea had origins ranging from eastern Europe, the Black Sea, and the Balkans, while those arriving over Crete had passed near the city of Athens, transferring anthropogenic emissions. During the flight conducted on 4 September, air masses originated mainly from western and central Europe and the wind patterns were more uniform and representative of the summer period in the region. For both flights we observed that the organic species accounted for almost 50 % of the volume of the particles, and that their acidity increased with increasing altitude. Higher spatial uniformity of the chemical composition of the particles was observed during the second flight as a result of the low variability in the origin and the paths of the air masses arriving in the region. The acidity of the particles observed during that flight was significantly high at high altitudes, exhibiting H_2SO_4 volume fractions of up to 0.4.

Using the particle parameters κ_{org} and ρ_{org} obtained from the closure study when the aircraft flew in the vicinity of the ground station, the cToF-AMS chemical composition measurements were used to estimate vertical profiles of the aerosol single hygroscopic parameter κ_{mix}. Although the median hygroscopic parameter was not significantly different for both flights (i.e., 0.31 and 0.36 during the flights on 1 and 4 September, respectively), its vertical variability was higher during the first flight. This can be explained by the high diversity in the origin of the air masses arriving in the study region, and the contribution of polluted air from the wider Athens area over the southern Aegean Sea during that flight. Despite that the measurements

were performed in the marine environment of the Aegean Sea, the estimated median hygroscopic parameters were more representative of continental aerosol particles.

Acknowledgements

The airborne measurements reported in this work have been supported by the EUFAR (227159) EC grant agreement under the Aegean-Game-2 project. Airborne data were obtained using the BAe-146-301 Atmospheric Research Aircraft (ARA) flown by Directflight Ltd and managed by the Facility for Airborne Atmospheric Measurements (FAAM), which is a joint entity of the Natural Environment Research Council (NERC) and the Met Office. The ground measurements have been co-financed by the European Union (European Social Fund – ESF) and Greek national funds through the operational program "Education and Lifelong Learning" of the National Strategic Reference Framework (NSRF) – research funding program: Heracleitus II, Investing in knowledge society through the European Social Fund.

References

Aiken, A. C., Decarlo, P. F., Kroll, J. H., Worsnop, D. R., Huffman, J. A., Docherty, K. S., Ulbrich, I. M., Mohr, C., Kimmel, J. R., Sueper, D., Sun, Y., Zhang, Q., Trimborn, A., Northway, M., Ziemann, P. J., Canagaratna, M. R., Onasch, T. B., Alfarra, M. R., Prévôt, A. S. H., Dommen, J., Duplissy, J., Metzger, A., Baltensperger, U., and Jimenez, J. L.: O/C and OM/OC ratios of primary, secondary, and ambient organic aerosols with high-resolution time-of-flight aerosol mass spectrometry, Environ. Sci. Technol., 42, 4478-4485, 2008.

Allan, J. D., Jimenez, J. L., Williams, P. I., Alfarra, M. R., Bower, K. N., Jayne, J. T., Coe, H., and Worsnop, D. R.: Quantitative sampling using an aerodyne aerosol mass spectrometer - 1. Techniques of data interpretation and error analysis", J. Geophys. Res. Atmos., 108, 4090, doi:10.1029/2002JD002358, 2003.

Allan, J. D., Coe, H., Bower, K. N., Alfarra, M. R., Delia, A. E., Jimenez, J. L., Middlebrook, A. M., Drewnick, F., Onasch, T. B., Canagaratna, M. R., Jayne, J. T., and Worsnop, D. R.: A generalised method for the extraction of chemically resolved mass spectra from aerodyne aerosol mass spectrometer data, J. Aerosol Sci., 35, 909-922, 2004.

Biskos, G., Paulsen, D., Russell, L. M., Buseck, P. R., Martin, S. T.: Prompt deliquescence and efflorescence of aerosol nanoparticles. Atmos.Chem. Phys., 6, 4633-4642, doi:10.5194/acp-6-4633-2006, 2006a.

Biskos, G., Russel, L. M., Buseck, P. R., Martin, S. T.: Nanosize effect on the hygroscopic growth factor of aerosol particles, Geoph.Res. Lett., 33, L07801 doi:10.1029/2005GL025199, 2006b.

Biskos, G., Buseck, P. R., Martin, S. T.: Hygroscopic Growth of Nucleation-mode Acidic Sulfate Particles, J. Aerosol Sci., 40, 338-347, 2009.

Canagaratna, M. R., Jayne, J. T., Jimenez, J. L., Allan, J. D., Alfarra, M. R., Zhang, Q., Onasch, T. B., Drewnick, F., Coe, H., Middlebrook, A., Delia, A., Williams, L. R., Trimborn, A. M., Northway, M. J., DeCarlo, P. F., Kolb, C. E., Davidovits, P., and Worsnop, D. R.: Chemical and microphysical characterization of ambient aerosols with the aerodyne aerosol mass spectrometer, Mass Spectrom. Rev., 26, 185–222, 2007.

Clarisse, L., Clerbaux, C., Dentener, F., Hurtmans, D., and Coheur, P.-F.: Global ammonia distribution derived from infrared satellite observations, Nature Geosci., 2, 479–483, 2009.

Clegg, S. L., Brimblecombe, P., Wexler, A. S.: Thermodynamic Model of the System H^+- NH_4^+ - SO_4^{2-} - NO_3^- - H_2O at TroposphericTemperatures. J. Phys. Chem. A, 102, 2137–2154, 1998.

Drewnick, F., Hings, S. S., DeCarlo, P., Jayne, J. T., Gonin, M., Fuhrer, K., Weimer, S., Jimenez, J. L., Demerjian, K. L., Borrmann, S., and Worsnop, D. R.: A new time-of-flight aerosol mass spectrometer (TOF-AMS)-instrument description and first field deployment, Aerosol Sci. Tech., 39, 637-658, 2005.

Duplissy, J., DeCarlo, P. F., Dommen, J., Alfarra, M. R.: Relating hygroscopicity and composition of organic aerosol particulate matter. Atmos. Chem. Phys., 11, 1155–

1165, doi:10.5194/acp-11-1155-2011, 2011.

Engelhart, G. J., Hildebrandt, L., Kostenidou, E., Mihalopoulos, N., Donahue, N. M., and Pandis, S. N.: Water Content of aged aerosol, Atmos. Chem. Phys., 11, 911–920, doi:10.5194/acp-11-911-2011, 2011.

Foltescu, V. L., Selin, E., and Below, M.: Corrections for particle losses and sizing errors during aircraft aerosol sampling using a rosemount inlet and the pms las-x, Atmos. Environ., 29, 449–453, 1995.

Gysel, M., Crosier, J., Topping, D. O., Whitehead J. D.: Closure study between chemical composition and hygroscopic growth of aerosol particles during TORCH2, Atmos. Chem. Phys., 7, 6131–6144, doi:10.5194/acp-7-6131-2007, 2007.

Gysel, M. McFiggans, G.B. Coe, H.: Inversion of tandem differential mobility analyser (TDMA) measurements, J. Aerosol Sci., 40, 134-151, 2009.

Hallquist, M., Wenger, J. C., Baltensperger, U., Rudich, Y., Simpson, D., Claeys, M., Dommen, J., Donahue, N. M., George, C., Goldstein, A. H., Hamilton, J. F., Herrmann, H., Hoffmann, T., Iinuma, Y., Jang, M., Jenkin, M. E., Jimenez, J. L., Kiendler-Scharr, A., Maenhaut, W., McFiggans, G., Mentel, Th. F., Monod, A., Prévôt, A. S. H., Seinfeld, J. H., Surratt, J. D., Szmigielski, R., Wildt, J.: The formation, properties and impact of secondary organic aerosol: current and emerging issues, Atmos. Chem. Phys., 9, 5155–5236, doi:10.5194/acp-9-5155-2009, 2009.

Haywood, J. and Boucher, O.: Estimates of the direct and indirect radiative forcing due to tropospheric aerosols: a review, Rev. Geophys., 38, 513–543, 2000.

Heintzenberg J.: Fine particles in the global troposphere. A review , Tellus, 41B, 149-160, 1989.

Hussein, T., Maso, M. D., Petäjä, T., Koponen I. S., Paatero, P.: Evaluation of an automatic algorithm for fitting the particle number size distributions, Boreal Environ. Res., 10, 337–355, 2005.

Kalivitis, N., Birmili, W., Stock, M., Wehner, B., Massling, A., Wiedensohler, A., Gerasopoulos, E., and Mihalopoulos, N.: Particle size distributions in the Eastern Mediterranean troposphere, Atmos. Chem. Phys., 8, 6729–6738, doi:10.5194/acp-8-6729-2008, 2008.

Koulouri, E., Saarikoski, S., Theodosi, C., Markaki, Z., Gerasopoulos, E., Kouvarakis, G., Mäkelä, T., Hillamo, R., and Mihalopoulos, N.: Chemical composition and sources of fine and coarse aerosol particles in the eastern Mediterranean, Atmos. Environ., 42, 6542–6550, 2008.

Knutson, E. O. and Whitby, K. T.: Aerosol classification by electric mobility: apparatus, theory, and applications, J. Aerosol Sci., 6, 443–451, 1975.

Kreidenweis, S. M., Petters, M. D., and DeMott, P. J.: Single parameter estimates of aerosol water content, Environ. Res. Lett., 3, 035002, doi:10.1088/1748-9326/3/3/035002, 2008.

Lelieveld, J., Berresheim, H., Borrmann, S., Crutzen, P. J., Dentener, F. J., Fisher, H., Feichter, J., Flatau, P. J., Heland, J., Holzinger, R., Korrmann, R., Lawrence, M. G., Levin, Z., Markowitz, K. M., Mihalopoulos, N., Minikin, A., Ramanathan, V., de Reus, M., Roelofs, G. J., Scheeren, H. A., Sciare, J., Schlager, H., Schultz, M., Siegmund, P., Steil, B., Stephanou, E. G., Stier, P., Traub, M., Warneke, C., Williams, J., and Ziereis, H.: Global air pollution crossroads over the Mediterranean, Science, 298, 794–799, 2002.

Liu, P. S. K., Deng, R., Smith, K. A., Williams, L. R., Jayne, J. T., Canagaratna, M. R., Moore, K., Onasch, T. B., Worsnop, D. R., and Deshler, T.: Transmission efficiency of an aerodynamic focusing lens system: comparison of model calculations and laboratory measurements for the aerodyne aerosol mass spectrometer, Aerosol Sci. Tech., 41, 721–733, 2007.

Marcolli, C., Luo, B. P. and Peter, T.: Mixing of the organic aerosol fractions: liquids as the thermodynamically stable phases, J. Phys. Chem. A, 108, 2216–2224, 2004.

Middlebrook, A. M., Bahreini, R., Jimenez, J. L., and Canagaratna, M. R.: Evaluation of composition-dependent collection efficiencies for the aerodyne aerosol mass spectrometer using field data, Aerosol Sci. Tech., 46, 258–271, 2012.

Mihalopoulos, N., Stephanou, E., Kanakidou, M., Pilitsidis, S.,Bousquet, P.: Tropospheric aerosol ionic compositionabove the Eastern Mediterranean Area, Tellus B 49B, 314–326, 1997.

Morgan, W. T., Allan, J. D., Bower, K. N., Highwood, E. J., Liu, D., McMeeking, G. R., Northway, M. J., Williams, P. I., Krejci, R., and Coe, H.: Airborne measurements of the spatial distribution of aerosol chemical composition across Europe and evolution of the organic fraction, Atmos. Chem. Phys., 10, 4065–4083, doi:10.5194/acp-10-4065-2010, 2010.

Ogren, J. and Charlson, J.: Implications for models and measurementsof chemical inhomogeneities among cloud droplets, Tellus, 44B, 489–504, 1992.

Park, K., Kim, J. S., Miller, A. L.: A study on effects of size and structure on hygroscopicity of nanoparticles using a tandem differential mobility analyzer and TEM, J. Nanopart. Res., 11,175–183, 2009.

Petters, M. D. & Kreidenweis S. M.: A single parameter representation of hygroscopic growth and cloud condensation nucleus activity, Atmos. Chem. Phys., 7, 1961–1971, doi:10.5194/acp-7-1961-2007, 2007.

Pikridas, M., Bougiatioti, A., Hildebrandt, L., Engelhart, G. J., Kostenidou, E., Mohr, C., Prévôt, A. S. H., Kouvarakis, G., Zarmpas, P., Burkhart, J. F., Lee, B.-H., Psichoudaki, M., Mihalopoulos, N., Pilinis, C., Stohl, A., Baltensperger, U., Kulmala, M., and Pandis, S. N.: The Finokalia Aerosol Measurement Experiment – 2008 (FAME-08): an overview, Atmos. Chem. Phys., 10, 6793–6806, doi:10.5194/acp-10-6793-2010, 2010.

Pilinis, C. and Seinfeld, J. H.: Continued development of a general equilibrium model for inorganic multicomponent atmospheric aerosols, Atmos. Environ., 21, 2453–2466, 1987.

Pringle, K. J., Tost, H., Pozzer, A., Pöschl, U., and Lelieveld, J.: Global distribution of the effective aerosol hygroscopicity parameter for CCN activation, Atmos. Chem. Phys., 10, 5241–5255, doi:10.5194/acp-10-5241-2010, 2010.

Rader, D. J. and McMurry, P. H.: Application of the tandem differential mobility analyzer to studies of droplet growth or evaporation, J. Aerosol Sci., 17, 771–787, 1986.

Salisbury, G., Williams, J., Holzinger, R., Gros, V., Mihalopoulos, N., Vrekoussis, M., Sarda-Estéve, R., Berresheim, H., von Kuhlmann, R., Lawrence, M., and Lelieveld, J.: Ground-based PTR-MS measurements of reactive organic compounds during the MINOS campaign in Crete, July–August 2001, Atmos. Chem. Phys., 3, 925–940, doi:10.5194/acp-3-925-2003, 2003.

Spengler, J. D., Brauer, M., and Koutrakis, P.: Acid air and health, Environ. Sci. Technol., 24, 946–955, 1990.

Stock, M., Cheng, Y. F., Birmili, W., Massling, A., Wehner, B., Müller, T., Leinert, S., Kalivitis, N., Mihalopoulos, N., and Wiedensohler, A.: Hygroscopic properties of atmospheric aerosol particles over the Eastern Mediterranean: implications for regional direct radiative forcing under clean and polluted conditions, Atmos. Chem. Phys., 11, 4251–4271, doi:10.5194/acp-11-4251-2011, 2011.

Stolzenburg, M. R. and McMurry, P. H.: TDMAFIT user's manual, Particle Technology Laboratory, Department of Mechanical Engineering, Univercity of Minnesota, Minneapolis, 1–61, 1988.

Stolzenburg, M. R. and McMurry, P. H.: An ultrafine aerosol condensation nucleus counter, Aerosol Sci. Technol., 14, 48–65,1991.

Tombrou, M., Bossioli, E., Kalogiros, J., Allan, J., Bacak, A., Biskos, G., Coe, H.,Dandou, A., Kouvarakis, G., Mihalopoulos, N., Protonotariou, A. P., Szabó-Takács, B., and Triantafillou, E.: Physical and chemical processes of polluted air masses during etesians: Aegean-Game airborne campaign – an out-line, in advances in meteorology, climatology and atmospheric physics, Springer Atmospheric Sciences, 1239–1244, Springer Verlag Berlin Heidelberg, 2012.

Wang, C. S. and Flagan C. R.: Scanning electrical mobility spectrometer, Aerosol Sci. Technol., 13, 230–240, 1990.

Wang, X., Kruis, F. E., and McMurry, P. H.: Aerodynamic focusing of nanoparticles: I. Guidelines for designing aerodynamic lenses for nanoparticles, Aerosol Sci. Tech., 39, 611–623, 2005.

Wex, H., McFiggans, G., Henning, S., and Stratmann, F.: Influence of the external mixing state of atmospheric aerosol on derived CCN number concentrations, Geophys. Res. Lett., 37, L10805, doi:10.1029/2010GL043337, 2010.

Supplement

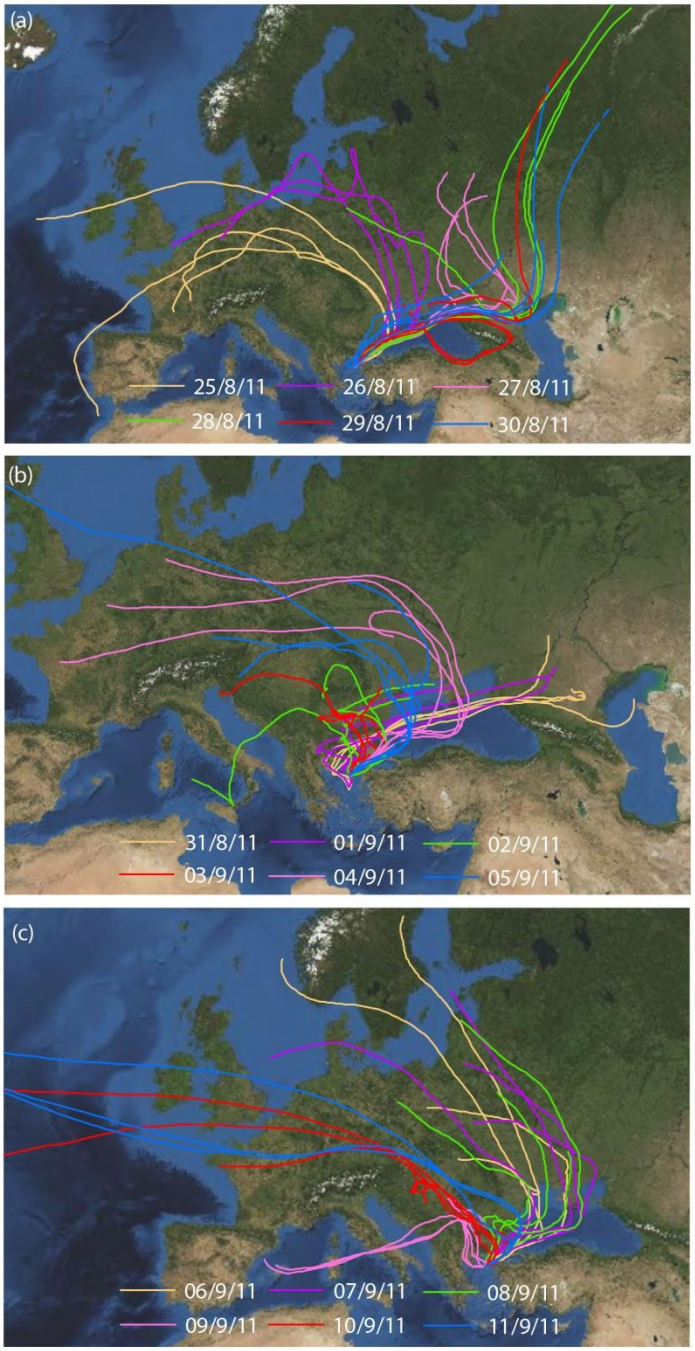

Figure S1. Wind back trajectories (120-hours long) caclulated by NOAA's HYSPLIT model for the ground station station located at Vigla on the island of Lemnos at an altitude of 420 m asl. Different colors corespond to back trajectories arriving at the station on different dates during the field campaign.

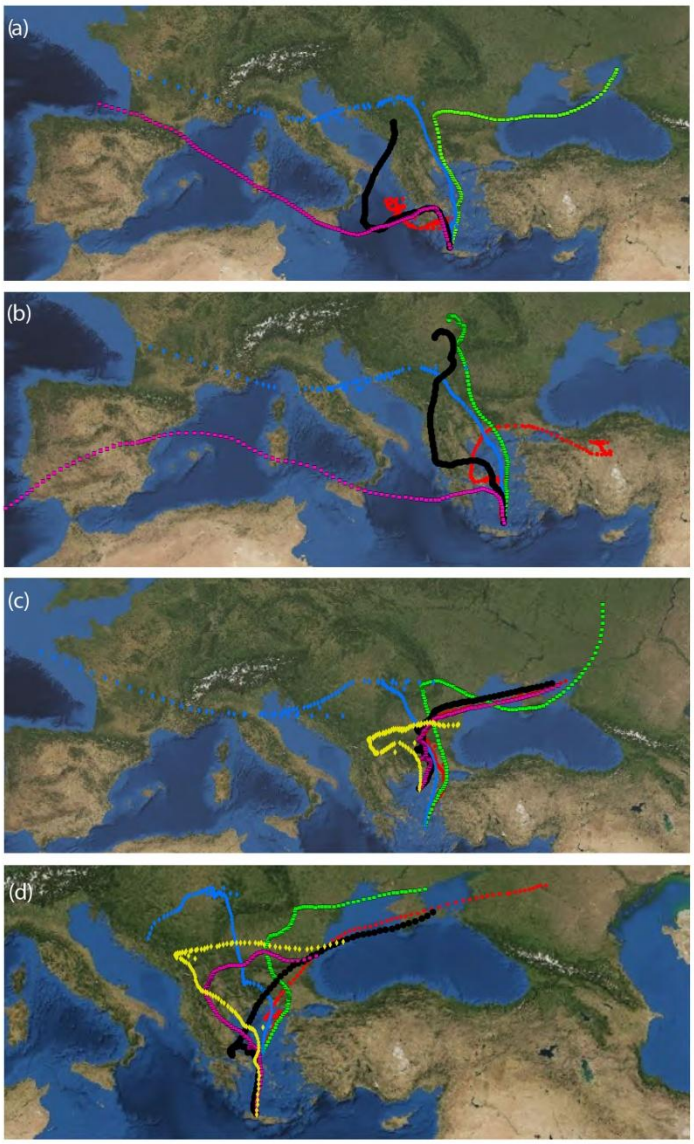

Figure S2. Wind back trajectories (120-hours long) caclulated by NOAA's HYSPLIT model for the different positions of the aircraft during the flight on the 1st of September 2011. The calculations have been performed when the aircraft was over Chania at 09:00 UTC (a), over north of Crete at 10:00 UTC (b), over the central Aegean Sea and Lemnos at 11:00 and 12:00 UTC, respectively (c), and over the central Aegean Sea and Chania on the way back at 13:00 and 14:00 UTC, respectively (d). Different colors of the trajectories correspond to different flight altitudes: 500 m (red), 1500 m (green), 2500 m (blue), 3500 m (black), and 4500 m (magenta).

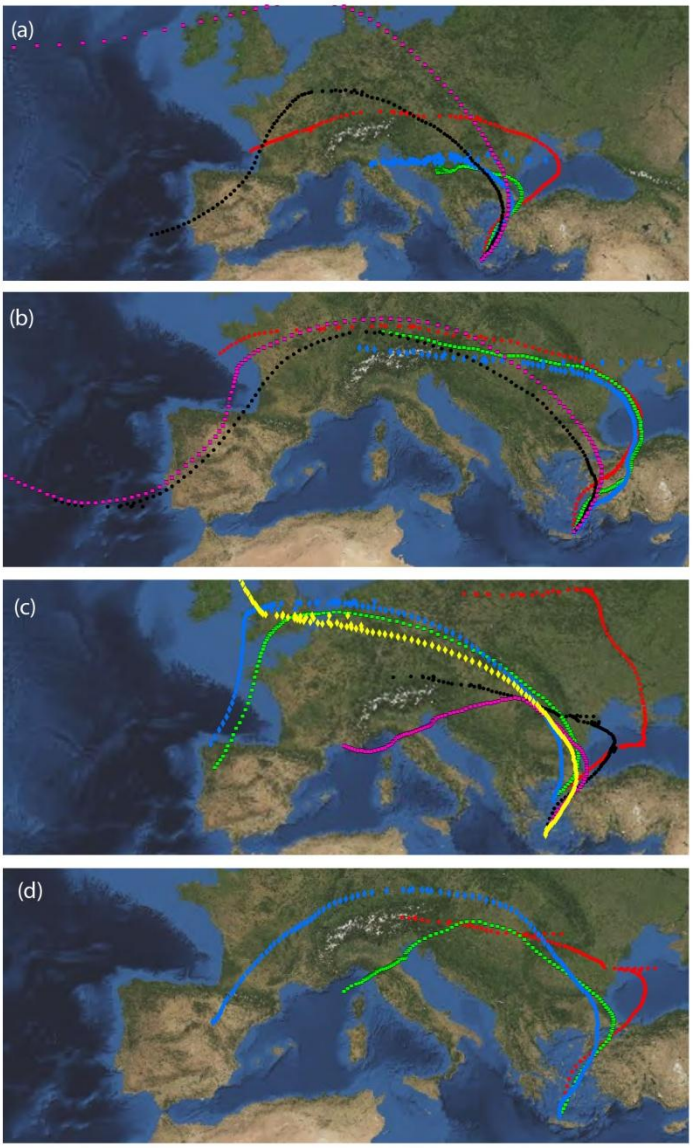

Figure S3. Wind back trajectories (120-hours long) caclulated by NOAA's HYSPLIT model for the different positions of the aircraft during the flight on the 4th of September 2011. The calculations have been performed when the aircraft was over Chania at 11:00 UTC (a), over eastern Crete at 12:00 UTC (b), over the Lemnos and northwestern of Crete at 13:00 and 14:00 UTC, respectively (c), and over Chania on the way back at 15:00 UTC, respectively (d). Different colors of the trajectories correspond to different flight altitudes: 500 m (red), 1500 m (green), 2500 m (blue), 3500 m (black), and 4500 m (magenta).

3. Hygroscopic Properties and Mixing State of Ultrafine Aerosol Particles in Urban Background Sites

Abstract

The hygroscopicity and mixing state of atmospheric ultrafine particles over suburban areas of two large cities in Greece, namely Athens and Patras, were measured using a combination of a Hygroscopic Tandem Differential Mobility Analyzer (HTDMA) and a continuous-flow streamwise-thermal-gradient Cloud Condensation Nuclei Counter (CCNC). The chemical composition of the particles was also measured using a High-Resolution Time-of-Flight Aerosol Mass Spectrometer (HR-ToF-AMS) and filter samples. Although both sites are affected by local and long range transported emissions, the measurements showed that the observed particles were more hygroscopic, more CCN active and more often externally mixed in Athens than in Patras. The frequency of externally mixed samples in both cases, was higher when long-range transported air masses passed above the city centers as indicated by wind back-trajectory calculations. Closure between HR-ToF-AMS and HTDMA/CCNC using the κ-Köhler theory was conducted for both sites, allowing the hygroscopic parameter of the organic fraction (κ_{org}) to vary between 0.0 and 0.3. In Patras the estimated hygroscopicity of the organic fraction was higher in super- than in sub-saturated conditions, indicating that the organics could exhibit different hygroscopicities, depending on the conditions they are exposed to. For both sub- and super-saturated conditions however, the estimated κ_{org} was comparable to other studies conducted in the eastern Mediterranean region. In contrast the closure conducted in Athens showed poorer agreement between the estimated from chemical composition hygroscopicity and that measured by either the HTDMA or the CCNC. A better agreement between HR-ToF-AMS and HTDMA/CCNC could be achieved if significant fractions of highly hygroscopic refractory or organic matter was present on the sampled particles. Such fractions of refractory matter on the particles is excluded based on filter samples collected on the site and on the fact that a diurnal variation on particle hygroscopicity was only observable with the HTDMA. The possibility of highly hygroscopic organic material cannot be excluded, nor corroborated by the measurements we have in our disposal, while it is very uncommon for atmospheric particles to be consisted by these organics.

3.1 Introduction

Atmospheric particles scatter and absorb the incoming solar radiation, thereby affecting the radiative balance of the Earth in a direct way (Haywood and Boucher, 2000). In addition, by acting as cloud condensation nuclei (CCN) they can affect the energy balance of the planet in an indirect way (Ogren and Charlson, 1992). Both the direct and indirect effect of atmospheric particles on climate depends strongly on their size and chemical composition, as well as on the amount of water they hold at different atmospheric conditions. The later is determined by the hygroscopicity and the CCN activity of the particles, i.e., their ability to take up water from the vapour phase when exposed to different relative humidity (RH) and supersaturated conditions, respectively.

Basic thermodynamic models (e.g., Clegg et al., 1998) have been developed for predicting the hygroscopic behaviour of pure or mixed inorganic particles. However, existing knowledge provides inaccurate predictions on the hygroscopicity of particles that consist of organic species or mixtures of organic and inorganic compounds. To simplify the association of particle chemical composition with hygroscopicity, Peters and Kreidenweiss (2007) proposed the use of a single hygroscopic parameter κ. Typical atmospheric soluble-salt particles such as ammonium sulphate or sodium chloride have κ values of 0.53 and 1.12, respectively, whereas those of organic compounds lie in the range between zero and 0.3 (Petters and Kreidenweiss, 2007). For completely insoluble but wettable particles, whose water activity is not affected by water adsorbed on their surface, the κ value is zero. Using the parameter κ, and information about the hygroscopic behaviour of the pure chemical species, one can make a good approximation of the water uptake characteristics of mixed atmospheric particles.

The use of the single parameter κ proposed by Petters and Kreidenweis has been one way for describing the hygroscopic behaviour of atmospheric aerosols in atmospheric-climate models (e.g., Liu and Wang, 2010). For accurately represent particle hygroscopicity in these models, however, observations of the hygroscopicity, as well as the and mixing state, of aerosol particles are needed for different regions (Pringle et al., 2010). Such measurements are available for remote environments in the region of the Aegean Sea and Eastern Mediterranean (Stock et al., 2011; Bougiatioti et al., 2009 and 2011; Bezantakos et al., 2013). However, to the best of our knowledge, the only data available for suburban environments in the broader

region of Southeastern Europe and especially for the mainland of Greece are those reported by Petäjä et al. (2007), which measured the hygroscopic growth factor of sub-50-nm particles in a suburban site close to Athens. Such measurements (i.e., conducted in suburban areas) can provide useful information on the hygroscopicity and CCN activity of freshly emitted (i.e., from local sources) or mixed (i.e., fresh and aged) aerosols. This is useful for evaluating regional/local scale climate or air quality models and in addition with background measurements, information on the impact of aging of anthropogenic aerosols in their hygroscopicity may be obtained.

In this work we report measurements of the CCN activity, hygroscopicity, and mixing state of particles observed in the atmosphere over suburban areas in Patras and Athens. The measurements were conducted using a combination of one Hygroscopic Tandem Differential Mobility Analyzer (HTDMA; Rader and McMurry, 1986) and a continuous flow streamwise thermal gradient Cloud Condensation Nuclei Counter (CCNC; Roberts and Nenes, 2005). The HTDMA and CCNC were coupled so that the hygroscopic behavior of dry monodisperse particles was measured simultaneously at sub- and super-saturated conditions, whereas the mixing state of the particles was also derived by the HTDMA part of the system. Particle chemical composition measurements were also conducted using a High-Resolution Time-Of-Flight Aerosol Mass Spectrometer (HR-ToF-AMS; DeCarlo et al., 2006) and filter samplers used to collect particles having diameters smaller than 2.5 μm ($PM_{2.5}$). Closure between the HTDMA/CCNC and chemical composition measurements was used in an attempt to further interpret the hygroscopicity of the particles observed in this study.

3.2. Experimental

Hygroscopicity measurements at sub- and super-saturated conditions were performed from 8 to 26 June 2012 in Patras and from 4 to 26 July 2012 in Athens. Particles chemical composition was measured during the total sampling period in Patras and from 12 to 26 July 2012 in Athens. The measuring site at Patras was located at FORTH/ICE-HT (38.297º N, 21.809º E), at a height of 85 m and ca. 10 km far from the center of the city. The measuring site in Athens was located in Demokritos GAW station (37.995º N, 23.816º E), at 250 m height, having a distance of ca. 8 km from the city center. The sampling locations were influenced by particles emitted from the cities when the wind had western and south- to northwestern direction in case of Patras and Athens, respectively (cf. Fig. 3.1). Five-day wind back-

trajectories, which were calculated on a 6-h basis using NOAA's HYSPLIT model (Draxler and Hess, 1997, 1998; Draxler, 1999; Stein et al., 2015), were employed to distinguish sub-periods during which air masses of different origin arrived at the two stations.

Fig 3.1. Map of Greece showing the locations of the ground stations in Patras and Athens.

3.2.1 Instrumentation

A combined system consisting of an HTDMA and a CCNC were used to measure the hygroscopic properties of particles when exposed to sub- and super-saturated conditions, respectively (cf. Fig. S3.1 in the supplement for the details). The whole system sampled air with a total flow rate of 1.8 lpm. Dried particles were selected by the first Differential Mobility Analyzer (DMA-1; TSI Model 3081; Knutsen and Whitby 1975) of the HTDMA. The closed-loop sheath flow and the monodisperse aerosol outlet flow of DMA-1 were 10.8 and 1.8 lpm, while the voltage on the central rod was changed every 6 minutes in order to select particles having mobility diameters of 60, 80, 100 and 120 nm. The aerosol flow upstream DMA-1 was dried to below 35% RH using a silica gel diffusion drier in Patras site, and below 15% using a dried air system and a Nafion humidity exchange membrane in Athens. A fraction (0.3 lpm) of the quasi-monodisperse flow downstream DMA-1 was passed through a Nafion-tube humidity exchanger where its RH was increased to 87%, before the size distribution of the particles was measured with a second DMA (DMA-2;

custom-made DMA using a closed-loop sheath flow with RH control; cf. Biskos et al., 2006a) and the Condensation Particle Counter (CPC, TSI Model 3772; Stolzenburg and McMurry, 1991). The RH in both the aerosol and the sheath flow in DMA-2 was controlled by PID controllers within a ±2% accuracy. Both DMAs in the HTDMA system were calibrated with Polystyrene Latex (PSL) spheres, while the overall performance of the HTDMA was investigated with ammonium sulfate particles. The rest (1.5 lpm) of the quasi-monodisperse flow downstream DMA-1 was sampled by the CCNC, which was operated in a scanning flow mode (Moore and Nenes, 2009). In this mode particles were exposed to super-saturations that progressively varied from 0.1 to 1.0%, allowing the rapid and continuous measurement of super-saturation spectra with high temporal resolution. A more detailed description of the CCNC used in this study is given in Bougiatioti et al. (2009).

An HR-ToF-AMS and filter samplers under an impactor with cutoff diameter of 2.5 μm were used to determine the chemical composition of the particles. Details of the HR-ToF-AMS can be found in DeCarlo et al. (2006). The collection efficiency (CE) was calculated using the algorithm of Kostenidou et al. (2007). The filter samples were collected daily on quartz pre-treated filters and were analyzed using ion chromatography for inorganic species of atmospheric relevance.

3.2.2. Data Analysis

3.2.2.1. HTDMA Measurements

The hygroscopic growth factor, *g*, determined by the HTDMA measurements is given by:

$$g(\mathrm{RH}|\mathrm{RH_{dr}}) = \frac{d_m(\mathrm{RH})}{d_{\mathrm{dry}}(\mathrm{RH_{dr}})}, \quad (3.1)$$

where $d_m(\mathrm{RH})$ and $d_{\mathrm{dry}}(\mathrm{RH_{dr}})$ are respectively the geometric mean mobility diameters of the sampled particles at the hydrated state (i.e., at RH = 87%) as measured by DMA-2 and the CPC, and at the dry state (i.e., $\mathrm{RH_{dr}}$ < 35% in Patras and $\mathrm{RH_{dr}}$ < 15% in Athens) as dictated by the settings (i.e., flow rates and voltage) used in DMA-1.

Internally mixed monodisperse dry particles exposed to elevated RH conditions within the HTDMA system will grow by the same amount due to water uptake. As a result they will exhibit a unimodal size distribution when measured by DMA-2 and the CPC of the HTDMA. Externally mixed dry monodisperse particles, on the other hand, may grow to different sizes exhibiting either a wider unimodal or a

bimodal size distribution when measured by the HTDMA. The TDMAfit algorithm (Stolzenburg and McMurry, 1988) was employed for inverting the HTDMA measurements and distinguishing between internally and externally mixed aerosols (cf. Bezantakos et al., 2013). Characteristic HTDMA measurements of internally and externally mixed particles after data inversion are provided in the supplement (Fig. S3.2).

3.2.2.2. CCNC Measurements

The super-saturated conditions within the CCNC were calibrated in terms of the temperature difference between the inlet and the outlet (ΔT = 5 °C), the instantaneous flow rate and the overall flow rate range. The relationship between super-saturation and instantaneous flow rate was determined by the procedure described by Moore and Nenes (2009). According to that, size-classified ammonium sulfate particles from DMA-1 are introduced into the CCNC whose flow, the range of super-saturated conditions, was scanned. For each particle size, the critical super-saturation value $S_{c,}$ above which particles act as CCN was obtained from Köhler theory (Moore et al., 2012a). The process was repeated with five different particles sizes. The calibration measurements were fitted with sigmoidal curves where the inflection point, corresponding to the S_c of the selected ammonium sulfate particles, was used to determine the critical activation flow rate Q_{50}. The absolute uncertainty of the calibrated CCNC super-saturation is estimated to be ± 0.04% (Moore et al., 2012a; 2012b).

The CCN activity of the particles is characterized by the activation ratio given by:

$$R_a \equiv \frac{CCN}{CN} = a_0 + \frac{a_1 - a_0}{1 + (Q/Q_{50})^{-a_2}}, \tag{3.2}$$

where CCN and CN are the activated and total particle concentrations, while a_0, a_1, a_2 and Q_{50} are constants that describe the minimum, maximum, slope and inflection point of the sigmoidal, respectively, while Q is the instantaneous volumetric flow rate. Ideally, a_0 is zero and a_1 is expected to be unity; however, values for a_1 varied throughout the measurement period depending on the selected aerosol particle size and the mixing state. The inflection point (i.e., Q_{50} or "critical flow rate"), corresponds to the instantaneous flow rate, that produces a level of super-saturation

within the CCNC that is required to activate the measured monodisperse aerosol. A characteristic sigmoid activation curve corresponding to particles having dry mobility diameter of 120 nm at super-saturated conditions ranging from 0.1 to 1.0% is shown in Fig. S3.3.

3.2.2.3. AMS Measurements

The standard HR-AMS data analysis software SQUIRREL v1.51C and PIKA v1.10C (Sueper, 2011) with Igor Pro 6.22A (Wavemetrics) was used for the AMS data analysis. For the organic mass spectra we applied the fragmentation table of Aiken et al. (2008) modifying the *m/z* ratio 18 and 28 according to Kostenidou et al., (2015). Positive Matrix Factorization, PMF, (Paatero and Tapper, 1994; Lanz et al., 2007) was applied to the high-resolution organic mass spectra using the measurements at *m/z* ratios between12 and 200 according to the approach of Ulbrich et al. (2009). PMF, which is a bilinear unmixing model, reproduces the measurements as a linear combination of factors to identify the different organic aerosol sources.

3.2.3. Estimation of the hygroscopic parameter κ

3.2.3.1. Determining the hygroscopic parameter κ from HTDMA measurements

The hygroscopic parameter κ can be determined by the hygroscopic growth factor measured by HTDMA as follows (Kreidenweis et al., 2008):

$$\kappa_{\mathrm{HTDMA}} = \frac{\left(g(\mathrm{RH})^3\text{-}1\right)}{a_{\mathrm{w}}/(1\text{-}a_{\mathrm{w}})}\ , \tag{3.3}$$

where g(RH) is the measured hygroscopic growth factor (i.e., at 87% RH in our measurements) and a_{w} is the water activity of the solution droplet, which can be calculated by:

$$a_{\mathrm{w}} \approx \frac{\mathrm{RH}}{100}\left(exp\left(\frac{4\sigma_{s/\alpha}\ M_w}{RT\rho_w d_m(RH)}\right)\right)^{-1}. \tag{3.4}$$

Here $\sigma_{s/a}$ and M_w are the surface tension and molecular weight of pure water (0.072 J m^{-2} and 18^{-3} kg/mol, respectively), R is the universal gas constant, T is the absolute temperature, ρ_{w} is the density of water and d_m is the diameter of the particles at elevated RH. Note that the exponential term, i.e., the Kelvin term, provides only a small correction for particles larger than 60 nm.

For externally mixed particles κ_{HTDMA} corresponding to each mode can be obtained. An average value of the hygroscopic parameter, which is representative of the hygroscopic properties of the entire particle population, can be also obtained as follows:

$$\bar{\kappa}_{\mathrm{HTDMA}} = \frac{\left(g_{\mathrm{avg}}(\mathrm{RH})^3 - 1\right)}{a_{\mathrm{w}}/(1-a_{\mathrm{w}})} . \quad (3.5)$$

Here g_{avg}(RH) is the average hygroscopic growth factor of the entire monodisperse particle population.

3.2.3.2. Determining the hygroscopic parameter κ from CCNC measurements

The hygroscopic parameter of the particles can also be obtained using the CCNC measurements (i.e., critical super-saturation) as follows:

$$\kappa_{\mathrm{CCN}} = \frac{4A^3}{d_{\mathrm{dry}}^3 S_c^2} , \quad (3.6)$$

where S_c is the critical super-saturation at which half of the monodisperse particles activate (cf. sect. 3.2.2.2), d_{dry} is the dry mobility diameter selected by DMA-1, and:

$$A = \frac{4M_{\mathrm{w}}\sigma_{\mathrm{w}}}{RT\rho_{\mathrm{w}}} . \quad (3.7)$$

Here M_{w}, σ_{w} and ρ_{w} are the molecular weight, the surface tension and the density of water, while R and T are the universal gas constant and temperature of the system, respectively.

3.2.3.3. Estimating the hygroscopic parameter κ from particle chemical composition measurements

The hygroscopic parameter of the particles can be estimated using measurements of their chemical composition as follows:

$$\kappa_{\mathrm{CHEM}} = \sum_{\mathrm{i}} \varepsilon_{\mathrm{i}} \kappa_{\mathrm{i}} . \quad (3.8)$$

Here $\varepsilon_i = V_{\mathrm{si}}/V_{\mathrm{s}}$ and κ_{i} are the volume fraction and the hygroscopic parameter of the ith chemical species comprising the particles, with V_{si} being the volume occupied by that species and V_{s} the volume of the dry particle. The volume fraction of each species was estimated using fixed densities for the inorganic compounds (cf. Bezantakos et al., 2013 and Table 1 therein; chapter 2 in this thesis). To determine the organic volume fraction of the particles the corresponding density of the organics ρ_{org}

was derived by combining the HR-ToF-AMS and the SMPS measurements (cf. DeCarlo et al., 2004). The hygroscopic parameters of the inorganic species were taken by Petters and Kreidenweis (2007; cf. Table 1 therein). For the organic fraction, κ_{org} was estimated by fitting the predicted hygroscopic parameters κ_{CHEM} to that determined by the HTDMA and the CCNC (i.e., $\bar{\kappa}_{HTDMA}$ and κ_{CCN}, respectively), for the 120-nm particles. The hygroscopic parameter κ_{CHEM} was estimated using 2-h averaged size resolved HR-ToF-AMS measurements corresponding to particles with vacuum aerodynamic diameters (VADs) from ca. 165 to 209 nm. The reason for using such a wide range of particle sizes was to improve the signal to noise ratio in the measurements. The fitted hygroscopic parameter of the organic fraction (i.e., κ_{org}) was allowed to vary from 0.0 to 0.3 (Kreidenweis et al., 2007).

Values of κ_{org} were also estimated on a 24-hour basis, were also estimated by fitting κ_{CHEM} obtained by the off-line chemical composition measurements with the corresponding 24-h averaged $\bar{\kappa}_{HTDMA}$and κ_{CCN} values. In this case, the mass of the inorganic fraction of the particles was obtained from the filter samples, while the mass and density of the organic fraction was obtained by the HR-ToF-AMS. A similar procedure, as described above was followed to estimate the aerosol hygroscopic parameter. The simplified ion-pairing scheme described by Gysel et al., (2007), was used for the measurements conducted in Patras. For the measurements in Athens, due to the presence of Na^+, Cl^-, Ca^{2+}, K^+ in the filter samples we used ISORROPIA II (Fountoukis and Nenes, 2007) for the ion-pairing of the inorganic fraction.

3.3. Results and Discussion

3.3.1. Measurements in the atmosphere over the suburban site of Patras

The measuring period in Patras was divided into three distinct sub-periods based on the origin of the air masses arriving at the monitoring station as determined by 5-day wind back-trajectories using the NOAA HYSPLIT model. During the first and the third sub-period (i.e., 8-17 and 24-27 June, respectively) the air masses had western and north western origin while during the second (18-23 June), their origin was north-eastern. Discussion of the measurements in the sections that follows is based on the wind patterns observed in each sub-period.

3.3.1.1. Particle Hygroscopicity at sub-saturated conditions (HTDMA measurements)

Figure 3.2 shows the calculated 5-day wind back-trajectories for characteristic days corresponding to each sub-period, together with the measured growth factor distributions for 60- and 120-nm particles exposed to 87% RH. On 11 and 26 June (i.e., representative days of the first and the third period) the air masses passed over the city of Patras (Fig. 3.2a and c) carrying both locally emitted and long-range transported particles. The observed aerosols during these days were both internally and externally mixed depending on the time, with the fraction of the latter being higher for the smaller dry mobility diameters (i.e., $d_{m,dry}$ = 60 nm) as shown in Fig. 3.2d, e and h, i. On 20 June (i.e., characteristic day of the second period) the air masses were not influenced by emissions from the city of Patras (Fig. 3.2b), as indicated by the fact that both the 60- and 120-nm particles were internally mixed (Figs. 3.2f and g).

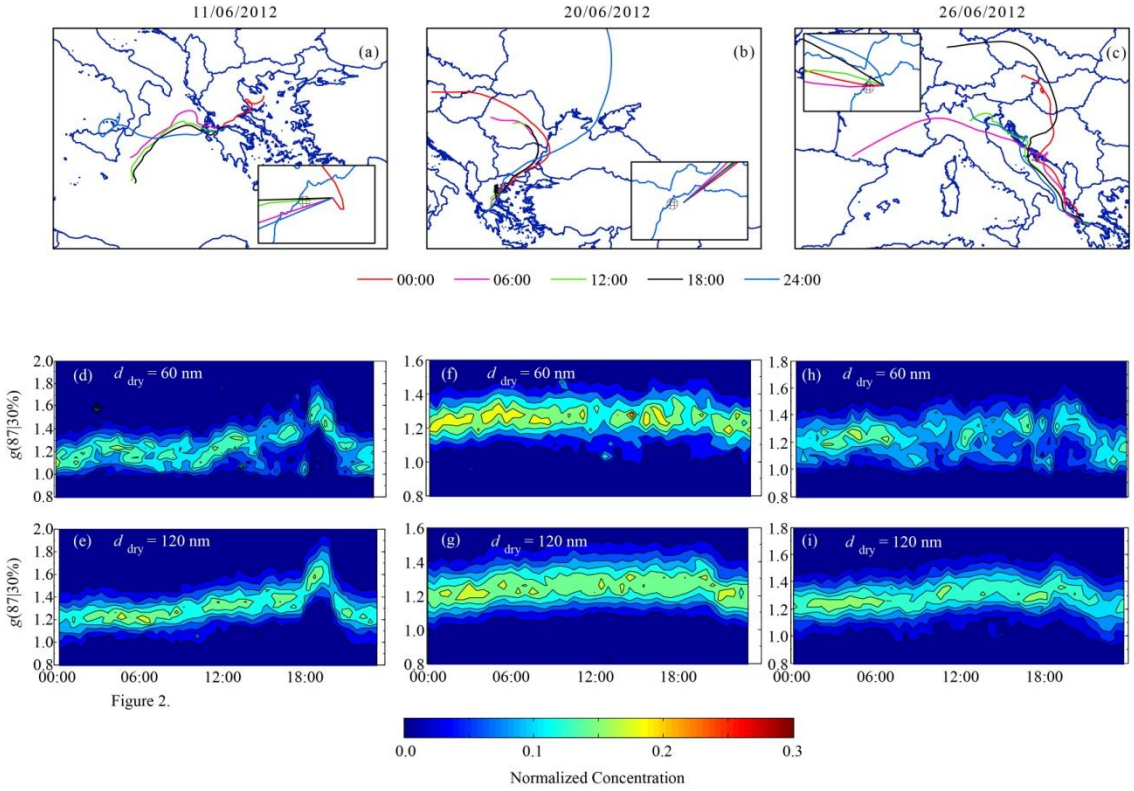

Fig. 3.2. Calculated 5-day wind back-trajectories and the growth factor distributions of 60- and 120-nm particles, when exposed to 87±2% RH, on 11 (**a, d, e**), 20 (**b, f, g**) and 26 (**c, h, i**) June. Three characteristic days that represent three distinct sub-periods during the measurements in Patras.

Figure 3.3 shows 6-h averaged hygroscopic growth factors of particles having dry mobility diameters of 60, 80, 100 and 120 nm after being exposed at 87% RH, for

the entire period of the measurements in Patras. The particles can be divided in more and less hygroscopic fractions, depending on whether they exhibit *g*(87|30%) values above or below 1.15, as indicated by solid red or open blue circles, respectively. The size of the circles in Fig. 3.3 indicates the relative population of the more or less hygroscopic fraction, while Table 3.1 summarizes the median values and the range of the more hygroscopic relative population in each sub-period.

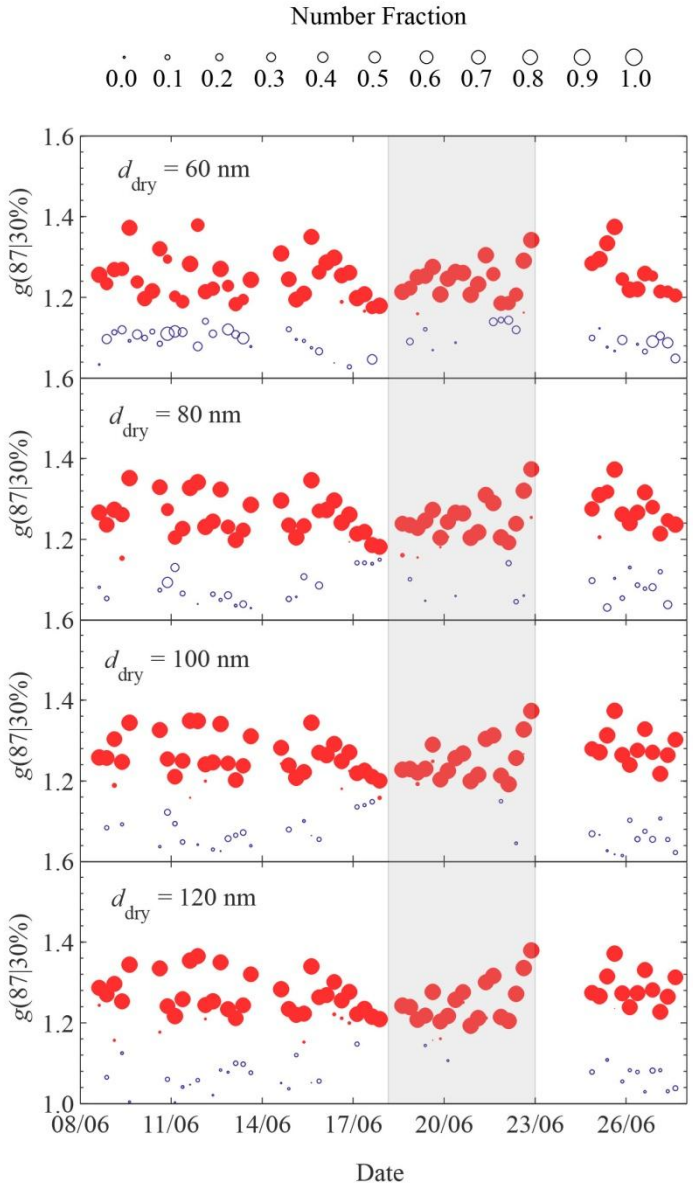

Fig. 3.3: HTDMA measurements of 60-, 80-, 100-, 120-nm particles for the entire period of the measurements in Patras. Particles that exhibit hygroscopic growth factor greater than 1.15 (more hygroscopic are denoted with red solid symbols, where as those with growth factors below 1.15 (less hygroscopic) with open blue circles. The size of the circles is proportional to the number fraction of each mode. The grayed area marks the second sub-period.

Table 3.1. Median values and range (in brackets) of the number fractions of particles residing in the more hygroscopic mode (i.e., $g(87\%|30\%) > 1.15$) during the three different sub-periods (P1 8-17 June; P2 18-23 June; P3: 24-27 June) of the measurements in Patras.

d_{dry} (nm)	P1	P2	P3
60	0.90 (0.34-1.00)	0.99 (0.75-1.00)	0.88 (0.47-1.00)
80	0.97 (0.60-1.00)	0.98 (0.89-1.00)	0.92 (0.73-1.00)
100	0.97 (0.86-1.00)	1.00 (0.92-1.00)	0.97 (0.86-1.00)
120	0.97 (0.89-1.00)	1.00 (0.93-1.00)	0.96 (0.89-1.00)

Overall, the majority of the particle population resided in the more hygroscopic mode. Particles having dry mobility diameters of 60 nm exhibited the highest fraction of less hygroscopic particles. The variability of the number concentration of the more hygroscopic mode decreased with increasing dry mobility diameter. Higher fractions of particles residing in the less hygroscopic mode were observed during the first and the third sub-period (i.e., 8-17 and 24-27 June, respectively) when more than 10% of the aerosol samples were externally mixed. This observation can be explained by the HR-ToF-AMS (cf. sect. 2.2.3), which during these two periods was measuring increased concentrations of the less oxygenated Hydrocarbon and Cooking-like Organic Aerosol (HOA and COA, respectively; cf. Fig. S3.4), indicating the presence of anthropogenic particles.

The median values and ranges of the hygroscopic growth factors of particles residing in either the less or the more hygroscopic mode during each sub-period of the measurements in Patras are summarized in Table 3.2. The observed particles exhibited hygroscopic growth factors similar to the ones observed in North Aegean Sea (cf. Bezantakos et al., 2013 and chapter 2 in this thesis) and 10% lower than the ones observed in South Aegean (cf. Stock et al., 2011).

Table 3.2. Median values and range (in brackets) of externally mixed particles classified as less hygroscopic (lh; $g \leq 1.15$) and as more hygroscopic (mh; $g > 1.15$) when exposed to 87% RH, during each sub-period in Patras.

d_{dry} (nm)	P1		P2		P3	
	lh	mh	lh	mh	lh	mh
60	1.10 (1.00-1.15)	1.23 (1.15-1.59)	1.13 (1.03-1.15)	1.24 (1.15-1.38)	1.08 (1.02-1.15)	1.26 (1.15-1.69)
80	1.05 (1.00-1.15)	1.24 (1.15-1.59)	1.06 (1.03-1.15)	1.24 (1.15-1.44)	1.05 (1.01-1.15)	1.27 (1.15-1.44)
100	1.05 (1.00-1.15)	1.25 (1.16-1.60)	1.06 (1.03-1.15)	1.24 (1.15-1.62)	1.03 (1.00-1.14)	1.27 (1.15-1.44)
120	1.04 (1.00-1.15)	1.25 (1.15-1.63)	1.13 (1.11-1.14)	1.24 (1.16-1.43)	1.03 (1.00-1.12)	1.27 (1.15-1.45)

3.3.1.2. Particle hygroscopicity at supersaturated conditions (CCNC measurements)

The hygroscopic parameters κ and activation fractions of the monodisperse particles determined by the CCNC measurements (i.e., when the particles were exposed to super-saturated conditions) averaged over 6 h are shown in Fig. 3.4 and summarized in Table 3.3. The lowest activation fractions but with the highest variability were observed for 60-nm particles in all three sub-periods. The larger particle exhibited similar activation fractions with values close to unity during most of the first sub-period. During the second and the third sub-periods, however, the larger particles exhibited somewhat lower activation fractions with values as low as 70%. Overall, the activation fraction decreased with increasing dry mobility diameter from 80 nm.

The variability of κ_{CCN} increased with increasing particle size but overall exhibited moderate values that are indicative of mixed particles composed of inorganic and organic species. Only the largest sampled particles (i.e., those having dry diameters of 100 and 120 nm) exhibited hygroscopic properties representative of pure inorganic particles during a short period around 22 June. The observed κ_{CCN} values were not significantly different than the ones reported by Bougiatioti et al. (2009) for the South Aegean region.

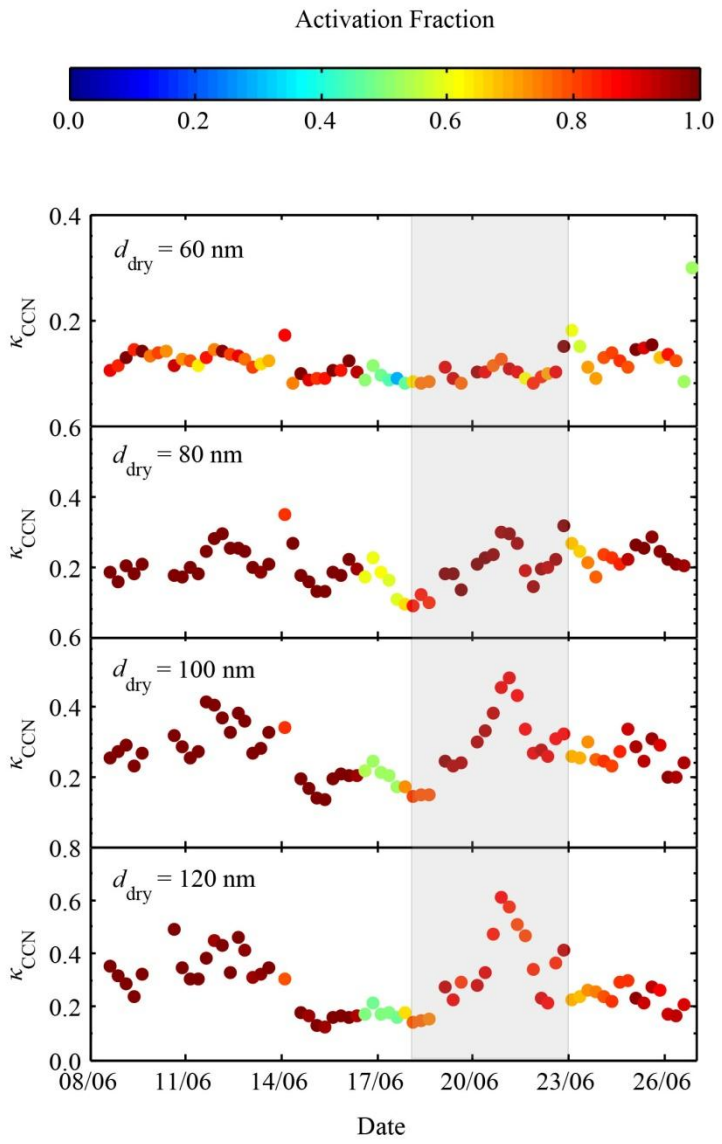

Fig 3.4. Hygroscopic parameters κ_{CCN} and their activation fractions (Color bar) of 60-, 80-, 100-, 120-nm particles, measured by the CCNC in Patras. The grayed area marks the second sub-period.

Table 3.3. Median values together with the range (in brackets) of hygroscopicity parameters κ and activation fractions R_a of particles having dry mobility diameters of 60, 80, 100 and 120 nm at various super-saturation conditions, rating from 0.1 to 1.0, in Patras suburban sampling site.

d_{dry} (nm)	P1		P2		P3	
	κ_{CCN}	Ra	κ_{CCN}	Ra	κ_{CCN}	Ra
60	0.12 (0.06-0.23)	0.82 (0.21-1.00)	0.10 (0.06-0.24)	0.77 (0.26-1.00)	0.13 (0.06-0.19)	0.83 (0.33-1.00)
80	0.18 (0.07-0.39)	1.00 (0.46-1.00)	0.20 (0.07-0.36)	0.91 (0.53-1.00)	0.23 (0.12-0.32)	0.88 (0.64-1.00)
100	0.23 (0.10-0.51)	1.00 (0.42-1.00)	0.27 (0.12-0.60)	0.83 (0.55-1.00)	0.24 (0.15-0.40)	0.87 (0.65-1.00)
120	0.23 (0.09-0.66)	1.00 (0.43-1.00)	0.26 (0.10-0.71)	0.79 (0.56-1.00)	0.23 (0.13-0.44)	0.84 (0.64-1.00)

3.3.1.3. Predicted hygroscopic parameter κ from particles chemical composition

Figure 3.5 shows 2-h averaged hygroscopic parameters derived from the HTDMA and CCNC measurements together with predictions using the size resolved particle chemical composition from the HR-ToF-AMS and the κ-Köhler theory as described in sect. 3.2.3.3. The hygroscopic parameter of the organic fraction κ_{org} shown in Fig. 3.5b and 3.5d, which was allowed to vary between zero and 0.3, was estimated by matching κ_{CHEM} with $\bar{\kappa}_{HTDMA}$ and κ_{CCN}, respectively. The median values and the range of the estimated κ_{CHEM} and κ_{org} parameters at both sub- and super-saturation conditions for the three sub-periods are shown in Table 3.4.

Table 3.4. Median values and range (in brackets) of the estimated aerosol and organic fraction's, hygroscopic parameters (κ_{CHEM} and κ_{org}) at different saturation (S) conditions in Patras. For the estimation κ_{CHEM} was fitted to the measured hygroscopic parameters of particles having dry mobility diameter of 120 nm by varying κ_{org}.

S	Variable	P1	P2	P3
Sub-saturation	κ_{CHEM}	0.2 (0.12-0.31)	0.17 (0.11-0.33)	0.21 (0.12-0.32)
	κ_{org}	0.00 (0.00-0.18)	0.00 (0.00-0.19)	0.00 (0.00-0.13)
super-saturation	κ_{CHEM}	0.29 (0.16-0.49)	0.27 (0.13-0.47)	0.27 (0.21-0.35)
	κ_{org}	0.10 (0.00-0.30)	0.13 (0.00-0.30)	0.00 (0.00-0.18)

The median value of the hygroscopic parameter of the organic fraction κ_{org} throughout the entire period of the measurements was zero when estimated at sub-saturated conditions (i.e., by fitting κ_{CHEM} to $\bar{\kappa}_{HTDMA}$) in all three sub-periods. Values of κ_{org} higher than 0.1 were estimated only in 15% of the cases during the first and the second sub-period and only in 4% during the third. The corresponding median value of κ_{org} estimated at super-saturated conditions (i.e., by fitting κ_{CHEM} to κ_{CCNC}) was 0.10 and 0.13 during the first and the second sub-period, respectively and zero

during the third. During the first and the second sub-period κ_{org} values of zero were estimated in 37 and 12%, respectively. During the third sub-period values of κ_{org} higher than 0.1 accounted for 18% of the cases.

Differences in the estimated κ_{org} values under different saturation conditions reflect observable deviations between the two methods used in measuring particle hygroscopicity (i.e., HTDMA and CCNC). Although in almost all of the cases κ_{CCN} and κ_{HTDMA} obtained for 120-nm particles were well correlated they exhibited differences, which in some cases reached 35%. Similar deviations have been also observed in other field campaigns (e.g., Irwin et al., 2010, Wu et al., 2013). These deviations could be partially explained by the properties of the measured particles, such as their shape and the surface tension of the resulting droplet. HTDMA derived κ values will be more affected than κ_{CCN} ones in the case that the particle shape is not spherical (Jung et al., 2011). In contrast, the derived κ_{CCN} values are affected, while κ_{HTDMA} values remain practically unaffected, if the surface tension of the resulting droplet defers significantly from that of pure water, which is assumed in κ-Köhler model, due to presence of surface active compounds on the particles (Dusek et al., 2011). However, the most probable explanation for the deviations observed between the κ_{org} values, when derived from HTDMA and CCN measurements seems to be the different hygroscopicity of the organic fraction when exposed to different saturation conditions. For instance, Wex et al. (2009) observed that laboratory generated, secondary organic aerosols (SOAs) exhibited a weak hygroscopic growth when exposed to RH < 90%, but a higher CCN activity than a single and constant hygroscopicity parameter derived from the sub-saturated hygroscopic measurements would suggest. Exposing the particles to sub-saturated conditions ranging from 90 to 99.6% they estimated that particles hygroscopic parameter increased by a factor of 4~6 and continued to increase when particles were exposed to super-saturated conditions. In addition, Henning et al. (2012) found differences in the hygroscopic behavior of soot particles coated with SOAs when the latter were either in a solid or in a dissolved/liquid state. The solubility of the organic compounds may be responsible for their different water up-take characteristics when exposed to sub- and super-saturation conditions (Petters et al., 2009). At sub-saturated conditions (i.e., RH < 90%) the organic compound remains almost undiluted but as the water vapor concentration increases it is gradually dissolved resulting to higher hygroscopicity.

A possible correlation between hygroscopicity of the organic fraction (i.e.,

κ_{org}) and the degree of its oxygenation or O:C ratio, had been proposed in other field and laboratory studies, like Chang et al., (2010) and Kuwata et al., (2013). In our case, however, no correlation was observed between O:C and estimated κ_{org} values. Despite that the organic fraction of the particles was dominated by SOAs as indicated by the HR-ToF-AMS measurements (cf. Fig. S3.4), in many cases we had to use a κ_{org} value of zero to obtain the best closure between the estimated κ_{CHEM} and the measured $\bar{\kappa}_{HTDMA}$ or κ_{CCN}.

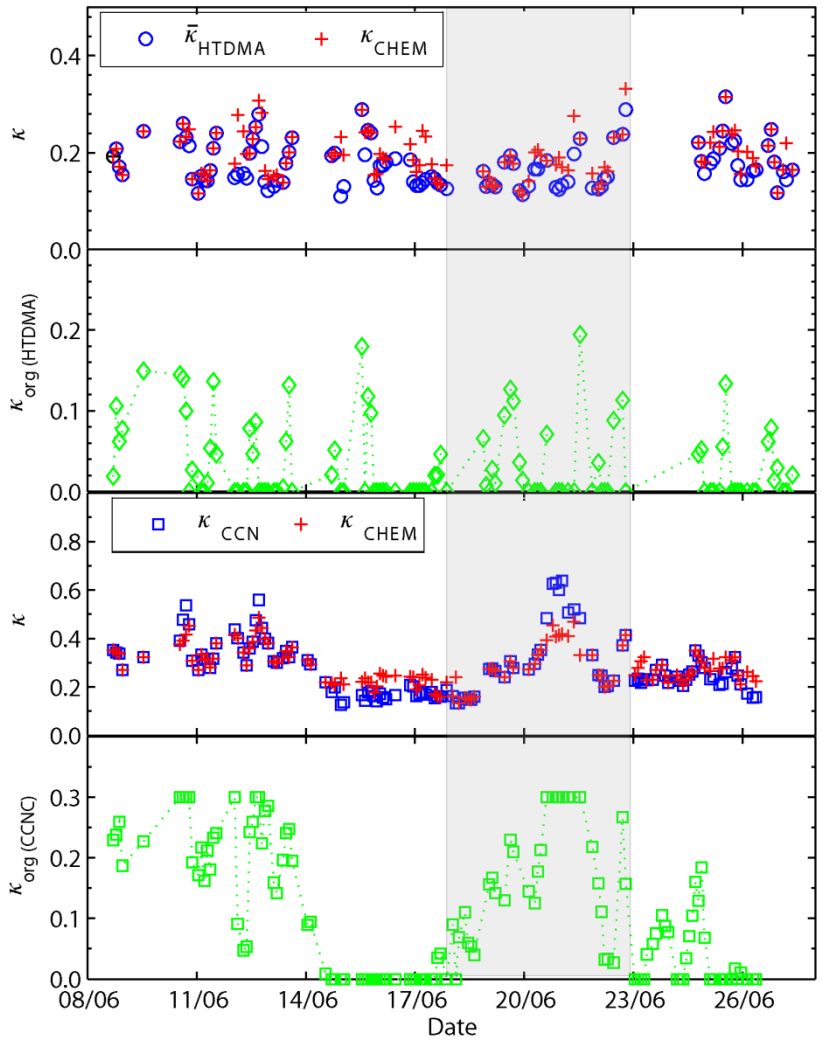

Fig. 3.5. Closure between the predicted κ_{CHEM} from the AMS measurements and κ derived from HTDMA ($\bar{\kappa}_{HTDMA}$) and CCNC measurements (κ_{CCN}) in Patras. κ_{CHEM} was predicted by applying the κ-Köhler theory on the size resolved chemical composition of the particles, while the hygroscopic parameter of the organic fraction (κ_{org}) was allowed to vary from 0.0 to 0.3.

To investigate the consistency of our analysis, estimates of κ_{org} were also made using the chemical composition of $PM_{2.5}$ filter samples collected over 24 h, and the procedure described in sect. 3.2.3.3. In this case κ_{CHEM} predictions were fitted to 24-h

averaged hygroscopic parameters derived from HTDMA and the CCNC measurements (cf. Fig. S3.5 and Table S3.1). The estimated κ_{org} at sub-saturated conditions (i.e., by fitting κ_{CHEM} derived from the filter samples to κ_{HTDMA}) indicated that the organic fraction of the sampled particles was hydrophobic in 42% of the cases during the first sub-period and in more than 66% of the cases during the third and the second sub-periods. At super-saturated conditions the estimated κ_{org} corresponded to slightly and mildly hygroscopic organic species. The estimated κ_{org} values obtained from filter samples indicated that the organic fraction exhibited higher water affinity when exposed to super-saturated conditions, which is similar to the observation made when κ_{org} values were estimated from HR-ToF-AMS measurements.

3.3.2. Measurements in the atmosphere over the suburban site of Athens

Five sub-periods could be distinguished on the basis of the 5-day wind back-trajectories calculated by the NOAA HYSPLIT model. During the first sub-period (4 to 8 July) the air masses had northwestern to northeastern origin, following variable trajectories, mostly over the mainland of Greece. The second sub-period from 9 to 10 July was characterized by the absence of wind, while the fourth sub-period (from 14 to 23 July was characterized by winds crossing the Aegean Sea. During the third and the fifth period (11 to 14 and 24 to 26 July, respectively) the air masses had variable directions that ranged from northeast to west, following trajectories over mainland Greece or over Athens. The following sections provide a discussion of the measurements conducted by taking into account the different wind patterns of each sub-period.

3.3.2.1. Particle Hygroscopicity at sub-saturated conditions (HTDMA measurements)

Figure 3.6 shows the calculated 5-day wind back-trajectories together with the measured growth factor distributions for 60- and 120-nm particles when exposed to 87% RH, for three characteristic days. On 4 July (i.e., representative day of the first sub-period) the air masses reached the sampling site from the northwest or from the north until ca. 12:00, passing above residential areas, while their direction changed to northeastern encountering less populated areas in the afternoon (Fig. 3.6a). The growth factor distributions measured on 4 July (Figs. 3.6d and e) indicate that the aerosol were mainly externally mixed with an increased less hygroscopic fraction at

lower dry mobility diameters (i.e., d_m = 60 nm) until noon, but switched to mostly internally mixed, coinciding with the change in wind direction.

On 13 July (i.e., representative day of sub-periods 3 and 5) the air masses had variable directions, passing above densely populated areas of the city before reaching the sampling site (Fig. 3.6b). Particles were mostly externally mixed until the early evening hours (i.e., around 18:00) and internally mixed afterwards, as indicated by the growth factor distributions (Fig. 3.6f and g). The fraction of the externally mixed samples was higher for the smaller dry particles as indicated by the broader growth factor distributions. On 22 July, which is a representative day of sub-periods 2 and 4, the calculated wind back-trajectories indicated that the air masses had the same paths passing over the Aegean Sea throughout the entire day (Fig. 3.6c). Particles observed on 22 July were in most of the cases internally mixed, exhibiting a decreasing fraction of internally mixtures with decreasing dry mobility diameters (Fig. 3.6h and i). Despite the different wind origins, particles appear to be externally mixed in the early morning hours (from ca. 6:00 to 10:00) in all three characteristic days, probably because of the morning traffic.

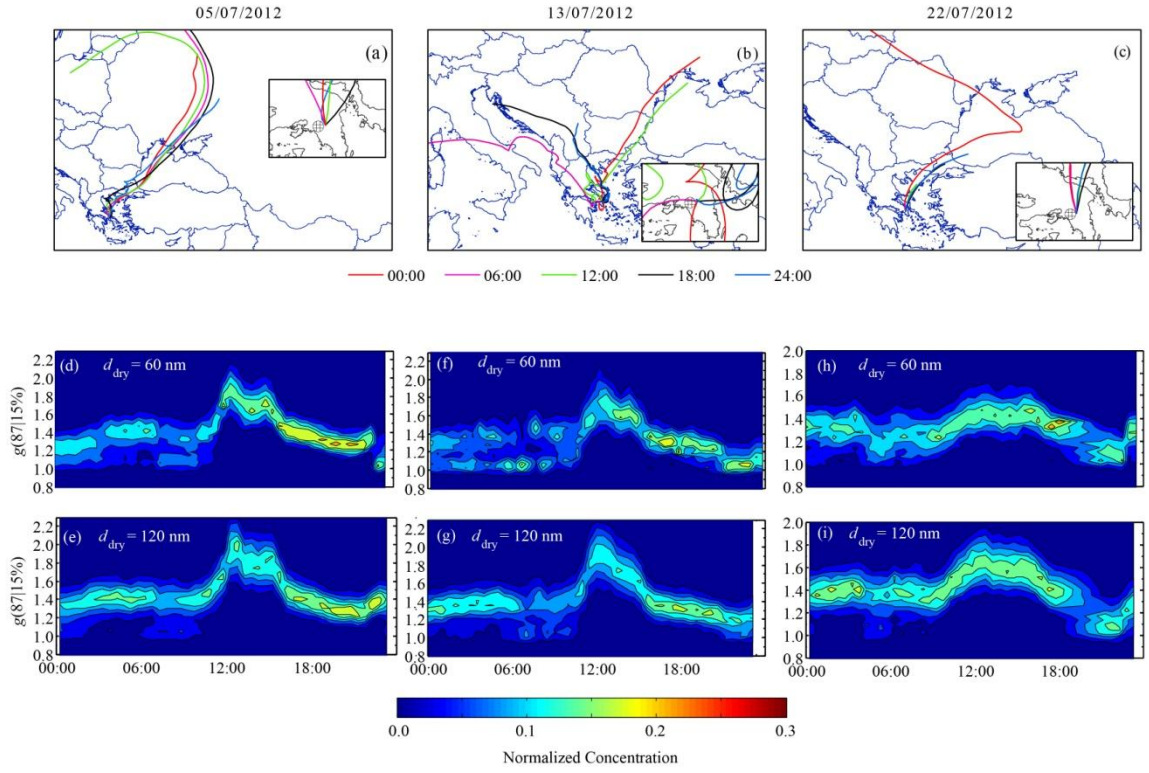

Fig 3.6. Calculated 5-day wind back-trajectories and growth factor distributions of 60- and 120-nm particles, when exposed to 87 ± 2% RH on 5 (**a, d, e**), 13 (**b, f, g**) and 22 (**c, h, i**) July. These days are characteristic and represent distinct sub-periods during the measurements in Athens. Sub-period one is

represented by 5 July, sub-periods 3 and 5 by 13 July and sub-periods 2 and 4 by 22 July.

The 6-hour averaged $g(87|15\%)$ hygroscopic growth factors together with the relative population (i.e., size of circles) of more or less hygroscopic particles during the entire period of the measurements in Athens are shown in Fig. 3.7. The median values and range of the relative populations of the more hygroscopic fraction for each sub-period is summarized in Table 3.5.

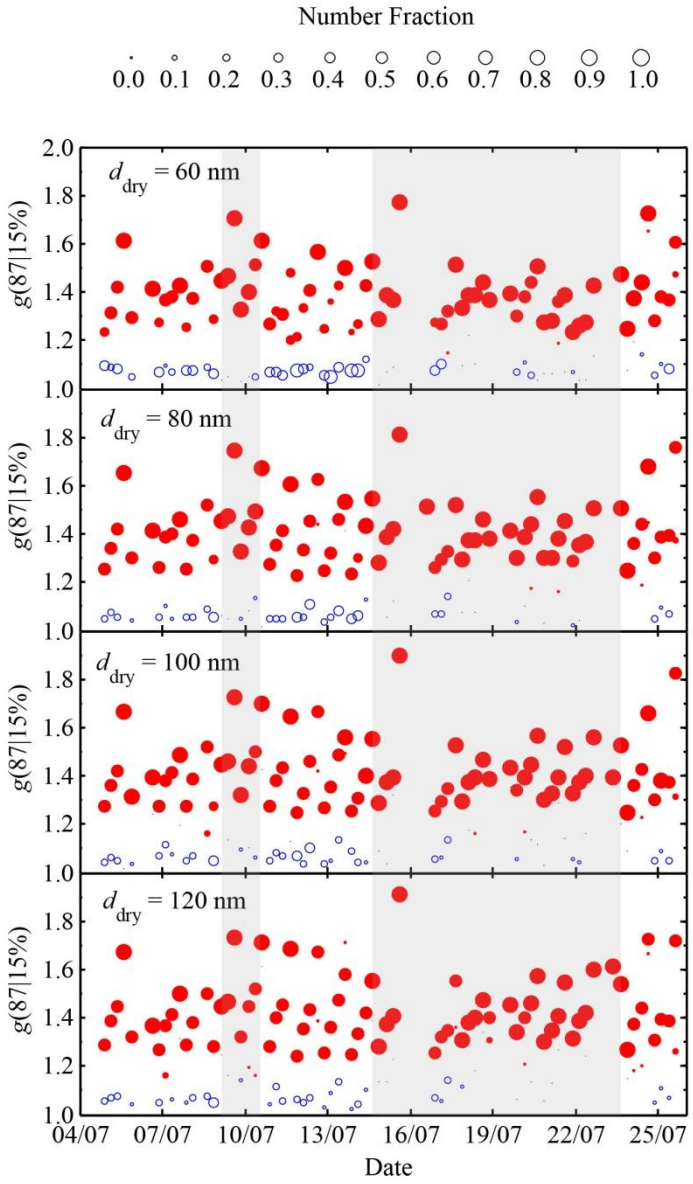

Fig. 3.7: HTDMA measurements of 60-, 80-, 100-, 120-nm particles for the entire period of the measurements in Athens. Particles that exhibit hygroscopic growth factor greater than 1.15 (more hygroscopic are denoted with red solid symbols, where as those with growth factors below 1.15 (less hygroscopic) with open blue circles. The size of the circles is proportional to the number fraction of each mode. The grayed areas mark the second and fourth sub-periods.

Compared to the measurements conducted in Patras, externally mixed particles were observed more often. Overall, the majority of the particles resided in the more hygroscopic mode. Higher fractions of the more hygroscopic group were observed during the second and the fourth sub-periods, when the particles were mostly internally mixed. An extended period of internally mixed aerosol during the fourth sub-period can be explained by the fact that the air masses were following trajectories over the Aegean Sea and thus were less affected by local sources. During the third sub-period a significant fraction (i.e., ca. 34%) of externally mixed 60-nm particles was classified as less hygroscopic, indicating the contribution of polluted city air to their hygroscopicity. Note that, during the third sub period, the air masses followed variable trajectories, with a significant fraction of them passing over Athens.

Table 3.5. Median values and range (in brackets) of the number fractions of particles residing in the more hygroscopic mode (i.e., $g(87|15\%) > 1.15$) during the five different sub-periods (P1 4-8 July; P2 9-10 July; P3 11-14 July; P4 14-23 July; P5 24-26 July) of the measurements in Athens.

d_{dry} (nm)	P1	P2	P3	P4	P5
60	0.81 (0.17-1.00)	1.00 (0.40-1.00)	0.66 (0.14-0.97)	0.98 (0.27-1.00)	0.89 (0.59-1.00)
80	0.88 (0.26-1.00)	0.99 (0.70-1.00)	0.85 (0.45-1.00)	1.00 (0.47-1.00)	0.89 (0.65-1.00)
100	0.88 (0.48-1.00)	1.00 (0.74-1.00)	0.83 (0.52-1.00)	1.00 (0.66-1.00)	0.91 (0.78-1.00)
120	0.90 (0.51-1.00)	0.97 (0.76-1.00)	0.85 (0.55-1.00)	1.00 (0.63-1.00)	0.89 (0.78-1.00)

Interestingly, even during the rest sub-periods (i.e., first, second, fourth and fifth) the fraction of the internally mixed and hygroscopic particles was higher from ca. 12:00 to 16:00. This increased growth factors overlapped with a decrease of the less oxygenated HOA, COA fractions determined by the HR-AMS measurements (cf. sect. 3.2.2.3 and Fig. S3.6). The observations above suggest that the aerosol mixing state could not be attributed to the wind direction alone but also to the contribution of local and distant sources. An increasing fraction of the volatile oxygenated organic

aerosols (V-OOA) in the afternoon was found by Kostenidou et al. (2015), who were conducting HR-AMS measurements at the same site and during the same period. At the same time they observed a reduction in the marine oxygenated aerosol factor (M-OOA) and suggested that the observed increase in the V-OOA is a product of photochemical processing, either in a local or at a regional scale.

Overall, the hygroscopicity of the sampled particles was higher in Athens than in Patras. The particles exhibited the highest hygroscopic behavior during the second sub-period (from 9 to 10 July), while during the rest of the sub-periods their hygroscopicity was similar (cf. Table 3.6). The hygroscopic growth factors of the 60-nm particles were on average similar to the ones reported by Petäjä et al. (2007), who measured particle hygroscopicity in a suburban site in Athens, however their variability and maximum values were higher.

Table 3.6. Median values and range (in brackets) of externally mixed particles classified as less hygroscopic (lh; $g \leq 1.15$) and as more hygroscopic (mh; $g > 1.15$) when exposed to 87% RH, during each sub-period in Athens.

d_{dry} (nm)	P1		P2		P3		P4		P5	
	lh	mh	lh	mh	lh	mh	lh	mh	lh	mh
60	1.08 (1.04-1.13)	1.37 (1.17-1.76)	1.05 (1.03-1.08)	1.44 (1.22-1.87)	1.07 (1.04-1.12)	1.36 (1.20-1.67)	1.07 (1.02-1.15)	1.36 (1.18-1.77)	1.07 (1.04-1.14)	1.38 (1.26-1.92)
80	1.06 (1.04-1.11)	1.38 (1.19-1.82)	1.06 (1.02-1.13)	1.45 (1.23-1.92)	1.06 (1.03-1.15)	1.36 (1.20-1.75)	1.05 (1.01-1.13)	1.36 (1.20-1.81)	1.06 (1.05-1.14)	1.4 (1.27-1.87)
100	1.05 (1.02-1.14)	1.37 (1.22-1.84)	1.09 (1.04-1.11)	1.44 (1.23-1.87)	1.05 (1.03-1.13)	1.37 (1.21-1.80)	1.07 (1.03-1.15)	1.38 (1.22-1.90)	1.05 (1.04-1.14)	1.38 (1.28-1.86)
120	1.06 (1.03-1.15)	1.39 (1.23-1.85)	1.12 (1.04-1.15)	1.45 (1.25-1.87)	1.05 (1.02-1.12)	1.38 (1.20-1.87)	1.08 (1.05-1.14)	1.39 (1.22-1.91)	1.05 (1.05-1.11)	1.39 (1.28-1.89)

In contrast to the observations in Patras, the hygroscopic growth factors of all samples observed in Athens exhibited a strong diurnal variation throughout the entire measuring period. As shown in Fig. 3.8, the hygroscopic growth factors for the 60- and 120-nm exhibited a peak from ca. 12:00 to 16:00 local time. During the same time the particles exhibit highest hygroscopic growths with g(87%|15%) reaching up to ca. 2.0.

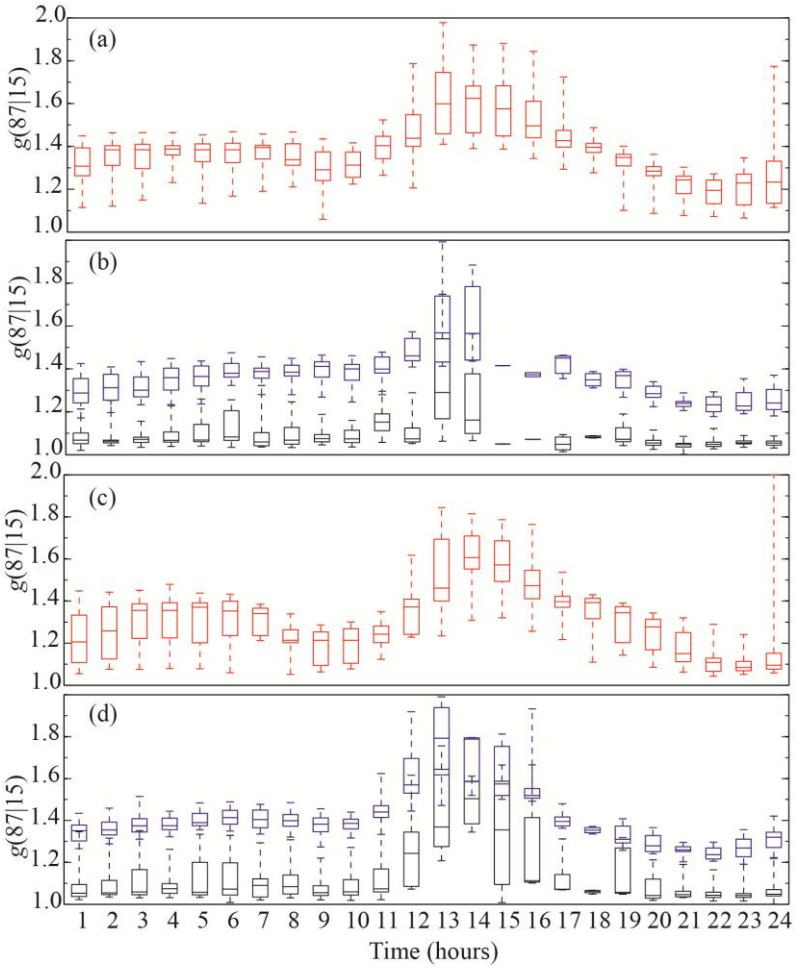

Fig 3.8. Diurnal variation of the hygroscopic growth factors of internally (**a, c**) and externally (**b, d**) mixed, which had dry mobility diameters of 60- (**a, b**) and 120- nm (**c, d**), in Athens.

Such high values have been either associated with sea-salt particles or organic salts such as sodium formate or sodium acetate (Peng and Chan, 2001; Wu et al., 2011). Sodium organic salts have been found to be present in marine environments and are products of sub-micron sea salt particles reacting with organic acids (Kerminen et al., 1998). A correlation (R^2 = 0.47) was found in the increase of V-OOA and the formic acid by Kostenidou et al. (2015), during the same hours. However, in order to observe such high values of hygroscopicity the particles chemical composition should be dominated (i.e., a volume fraction of 50% or more) by these organic salts, something that has never been observed in atmospheric particles. In addition the corroborating wind back trajectories showed that in only 60% of the cases the winds were passing over the Aegean Sea.

3.3.2.2. Particle hygroscopicity at super-saturated conditions (CCNC measurements)

The 6-hour averaged activation fractions and hygroscopic parameters of the monodisperse particles determined by the CCNC are shown in Fig. 3.9 and summarized in Table 3.7.

Compared to the κ_{CCN} values reported from the measurements in Patras, the hygroscopicity of the particles in Athens was higher. The lowest activation fractions were observed for 60-, while the highest for 120-nm particles in all sub-periods. Similarly to the HTDMA measurements, the minimum activation fraction for the 60-nm particles, observed during the third sub period (i.e., most affected by the city pollution) indicates that a significant fraction of these particles is externally mixed and cannot act as CCN, even at 1% super-saturation. In contrast, during the fourth period (i.e., winds mostly from the Aegean Sea) the activation fraction of 60-nm particles remains below 70%, while the HTDMA measurements indicate that 98% of the 60-nm particles exhibit hygroscopic growth factors of more than 1.15. This is indicative that except particle mixing state and chemical composition their size plays also a role in their CCN activity. For example, 120-nm particles exhibit activation fractions of more than 88% in all cases, despite their mixing state (i.e., measured by the HTDMA).

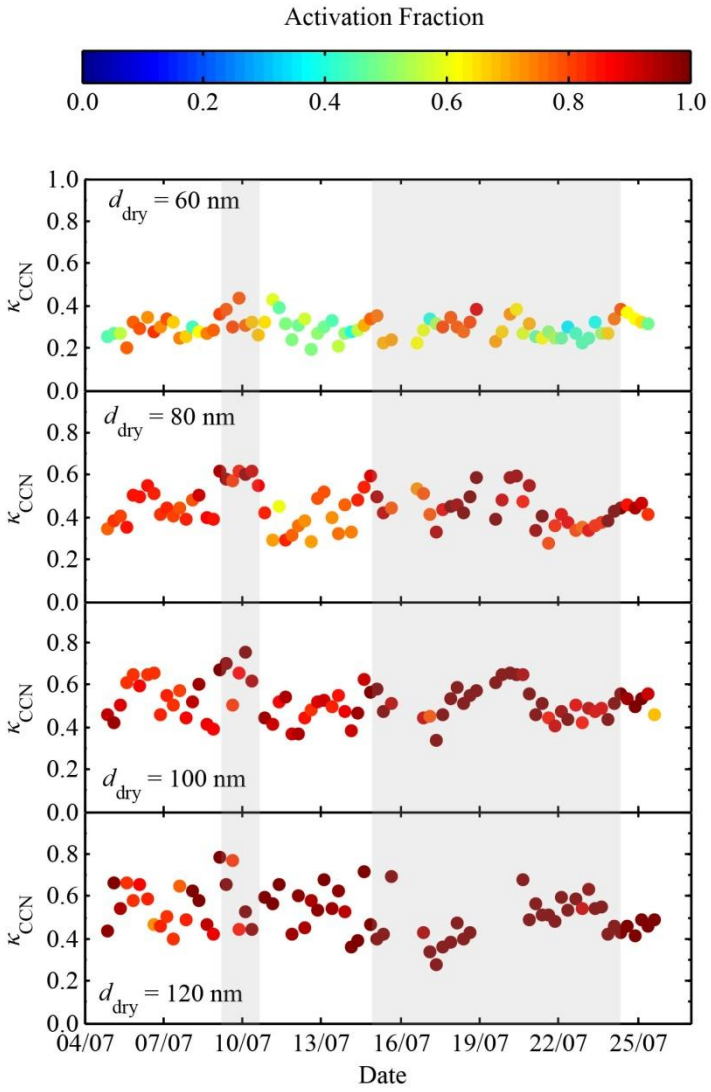

Fig. 3.9. Hygroscopic parameters κ_{CCN} and their activation fractions (Color bar) of 60-, 80-, 100-, 120-nm particles, measured by the CCNC in Athens. The grayed areas mark the second and fourth sub-periods.

Table 3.7. Median values together with the range (in brackets) of hygroscopicity parameters κ and activation fractions R_a of particles having dry mobility diameters of 60, 80, 100 and 120 nm at various super-saturation conditions, rating from 0.1 to 1.0, in Athens suburban sampling site.

d_{dry} (nm)	P1		P2		P3		P4		P5	
	κ_{CCN}	*Ra*	κ_{CCN}	*Ra*	κ_{CCN}	*Ra*	κ_{CCN}	*Ra*	κ_{CCN}	*Ra*
60	0.28 (0.15-0.45)	0.72 (0.26-0.94)	0.33 (0.21-0.52)	0.76 (0.23-0.96)	0.29 (0.14-0.50)	0.49 (0.22-0.93)	0.28 (0.16-0.49)	0.64 (0.13-1.00)	0.35 (0.21-0.49)	0.66 (0.22-0.95)
80	0.44 (0.20-0.67)	0.84 (0.59-1.00)	0.59 (0.30-0.74)	0.94 (0.77-1.00)	0.37 (0.17-0.61)	0.77 (0.46-1.00)	0.42 (0.14-0.70)	0.91 (0.61-1.00)	0.44 (0.27-0.57)	0.93 (0.68-1.00)

100	0.54 (0.15-0.84)	0.87 (0.65-1.00)	0.67 (0.37-0.83)	0.97 (0.81-1.00)	0.47 (0.22-0.69)	0.9 (0.67-1.00)	0.5 (0.24-0.76)	0.99 (0.41-1.00)	0.53 (0.37-0.68)	1 (0.62-1.00)
120	0.53 (0.17-0.81)	0.88 (0.71-1.00)	0.54 (0.32-0.86)	0.99 (0.81-1.00)	0.5 (0.17-0.83)	0.99 (0.83-1.00)	0.45 (0.20-0.80)	1 (0.80-1.00)	0.45 (0.30-0.61)	1 (0.89-1.00)

Although highly hygroscopic particles were observed occasionally during the entire period of the measurements, the highest κ_{CCN} values were systematically observed during the second sub-period. Particles having dry mobility diameters of 60 nm were the less hygroscopic while those having 100- and 120- nm were the most hygroscopic in all sub-periods. The median κ_{CCN} values of the larger particles (i.e., 80 to 120 nm) indicate the presence of highly hygroscopic aerosols, while the maximum measured values were even higher than that of ammonium sulfate (i.e., κ = 0.6 for CCNC measurements). Similar and in some cases higher, values of hygroscopicity were observed also with the HTDMA but only during around noon. In contrast to the HTDMA measurements however, particles hygroscopicity measured at super-saturated conditions did not exhibit diurnal variations. While the presence of highly hygroscopic material (e.g., sea salt, or sodium formate/acetate salts) on the particles could explain the high values of the measured $\kappa_{CCN,}$ their volume fraction on the measured particles should be dominant (i.e., more than 50%), something which is never reported for atmospheric particles of these sizes.

3.3.2.3. Predicted hygroscopic parameter κ from particles chemical composition

Estimations of the hygroscopic parameter of the organic fraction κ_{org} of the 120-nm particles when they were exposed to sub- and super-saturated conditions are shown in Fig. 3.10. The median values and the range of the estimated κ_{CHEM} and κ_{org} parameters at both sub- and super-saturation conditions are shown in Table 3.8.

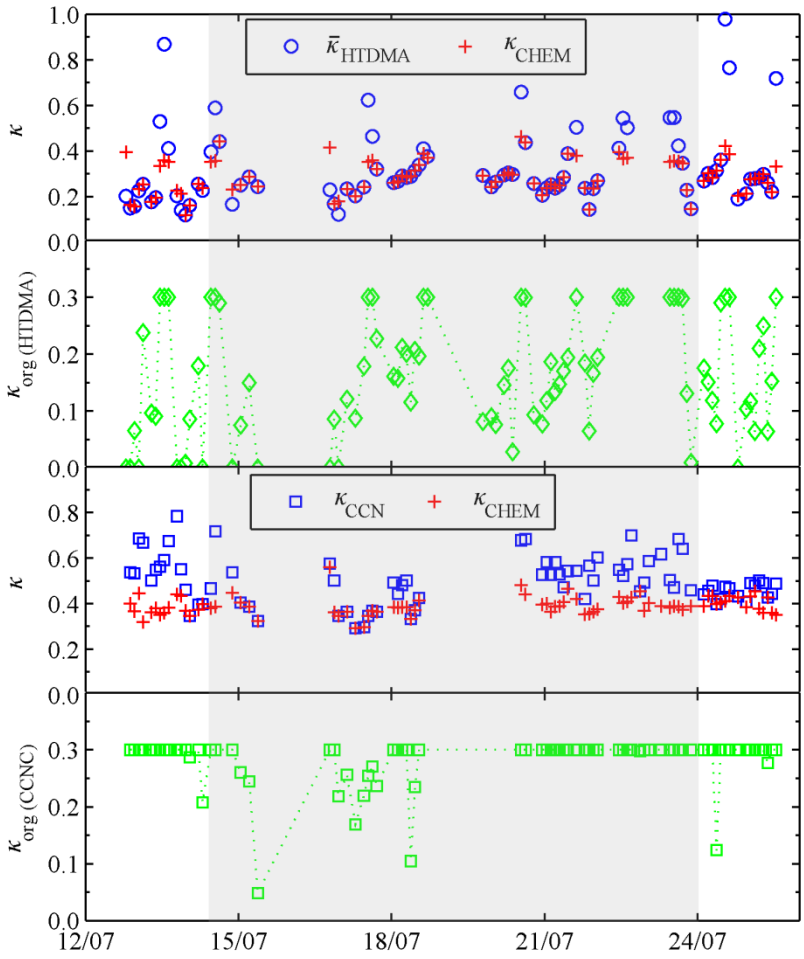

Fig. 3.10. Closure between the predicted κ_{CHEM} from the AMS measurements and κ derived from HTDMA ($\bar{\kappa}_{HTDMA}$) and CCNC measurements (κ_{CCN}) in Athens. κ_{CHEM} was predicted by applying the κ-Köhler theory on the size resolved chemical composition of the particles, while the hygroscopic parameter of the organic fraction (κ_{org}) was allowed to vary from 0.0 to 0.3.The grey area marks the fourth sub-period.

Overall, a better closure was achieved between κ_{CHEM} and the measured $\bar{\kappa}_{HTDMA}$, except during the afternoons, when the HTDMA measured hygroscopicity was significantly higher, even from pure ammonium sulfate. The closure between κ_{CHEM} and the measured κ_{CCN} was poorer with the latter exhibiting in almost all the cases higher values than the particles chemical composition predicted. In order to obtain the best fit between the estimated κ_{CHEM} and the measured $\bar{\kappa}_{HTDMA}$ or κ_{CCN}, in most cases a κ_{org} value of 0.3 had to be used. Higher κ_{org} values would result in a better fitting, but to the best of our knowledge this is the highest value for organic species used in studies of atmospheric relevance. As discussed in sect. 3.3.2.1 and 3.3.2.2 the high hygroscopicity observed with the HTDMA and the CCNC could be attributed to the

presence of sea salt, which cannot be detected by the HR-ToF-AMS, or to organic salts originating from sea salt reacting with organic acids (cf. sect. 3.3.2.1). However the volume fractions of these compounds should account for more than 50% of the particles dry volume, which is never reported neither for sea salt, nor for these organic salts, for atmospheric particles of 120-nm.

Table 3.8. Median values and range (in brackets) of the estimated aerosol and organic fraction's, hygroscopic parameters (κ_{CHEM} and κ_{org}) at different saturation (S) conditions in Athens. For the estimation, κ_{CHEM} was fitted to the measured hygroscopic parameters of particles having dry mobility diameter of 120 nm by varying κ_{org}.

S	Variable	P3	P4	P5
Sub-saturation	κ_{CHEM}	0.24 (0.12-0.39)	0.29 (0.14-0.46)	0.28 (0.20-0.42)
	κ_{org}	0.09 (0.00-0.30)	0.17 (0.00-0.30)	0.15 (0.00-0.30)
Super-saturation	κ_{CHEM}	0.38 (0.32-0.44)	0.39 (0.29-0.56)	0.41 (0.35-0.46)
	κ_{org}	0.3 (0.2-0.30)	0.3 (0.05-0.30)	0.3 (0.12-0.30)

Compared to the κ_{org} values estimated for the measurements conducted in Patras the estimated κ_{org} values in Athens were higher in order to obtain a better closure with the measurements.

The estimated κ_{org} values obtained from the off-line chemical composition measurements (cf. Fig. S3.7 and table S3.2) indicated no significant differences with those obtained from the HR-ToF-AMS, except for the fourth and the fifth sub-period at sub- and super-saturated conditions, respectively. Since the 24-h average hygroscopicity of the organic fraction is not radically affected by either using the filter samples or the HR-ToF-AMS, these measurements also indicate that either the mass concentration of refractory matter is limited and concentrated on specific hours or the organic components are more hygroscopic than the value of 0.30 we assumed. In the

case of significant concentrations of highly hygroscopic refractory matter, only during specific hours of the day, both the HTDMA and CCNC would measure increased hygroscopicities during those hours. However, the measured hygroscopicity by the CCNC does not reveal any temporal trend through the day, in contrast with the measured by HTDMA hygroscopicity, thus the presence of sea salt during specific hours of the day can be excluded. This leaves the possibility of organic material that is more hygroscopic than usually assumed in atmospheric measurements. As previously discussed however (cf. sect. 3.3.2.3) the presence of highly hygroscopic organic salts on 120-nm atmospheric particles with volume fractions of higher than 50% has been never observed.

3.4. Conclusions

In this work we report the mixing state and the hygroscopicity of aerosol particles observed at two suburban sites; one in the cities of Patras and on in Athens. The measurements were performed with dried size-selected particles having diameters from 60 to 120 nm that were exposed to sub- and super-saturated conditions using a combination of an HTDMA and a CCNC. Five-day wind back-trajectories were used to distinguish the measurements in sub-periods depending on whether the air masses arriving at the stations passed over the cities or not. Chemical composition measurements by an HR-ToF-AMS and $PM_{2.5}$ filter samples were used to estimate the hygroscopic parameter of the organic fraction κ_{org}.

Observing the behavior of the particles when exposed to sub-saturated conditions indicated that the aerosols over Athens were more often externally mixed and significantly more hygroscopic than those in Patras. For both stations the majority of the particles resided in the more hygroscopic mode (i.e., g(87%) > 1.15), while the population of the less hygroscopic mode (i.e., g(87%) <1.15) was increased during sub-periods influenced more by the city emissions. At super-saturated conditions the sampled particles were more CCN active and more hygroscopic in Athens. In both sampling sites the lowest κ_{CCN} values and activation fractions were observed for 60-nm particles while the highest for larger particles (i.e., particles having dry mobility diameters of 100 and 120 nm. Smaller (i.e., 60-nm), externally mixed particles were less CCN active during periods of increased pollution (e.g., third sub-period in Athens). In contrast, during the same periods, the larger (i.e., 120-nm), externally

mixed particles, even when composed of less hygroscopic material, were sufficiently acting as CCN, indicating that the particle size, except the particles chemical composition plays a role in their CCN activity.

The hygroscopic parameters of the organic fraction (κ_{org}) estimated by fitting the kappa values determined by the HTDMA and the CCNC measurements to those calculated using the HR-ToF-AMS measurements indicated that the organic compounds on the particles were more hygroscopic in Athens than in Patras. In Patras the organic fraction was in many cases estimated to be hydrophobic when exposed to sub-saturated conditions and never exceeded 0.2. However, employing the HR-ToF-AMS measurements to estimate κ_{org} in Athens resulted in many cases to poor fitting even when the maximum κ_{org} value of 0.3 was used. This can be only explained if a significant fraction (i.e., of more than 50%) of highly hygroscopic refractory (e.g., sea salt) or organic (e.g., sodium formate/acetate) material is present on the particles dry volume.

Using the chemical composition measurements provided by analyzing the filter samples did not radically alter the estimated κ_{org} values. This suggests either a significant fraction of highly hygroscopic refractory matter (e.g., NaCl), present only for a short period around noon during the day, or of organic compounds that are more hygroscopic than we assumed. For the first hypothesis (i.e., presence of significant amounts of refractory and matter during a short period of the day) both the CCNC and the HTDMA should measure increased hygroscopicity. However, a strong diurnal variation of the measured hygroscopicity, peaking during noon, was only observed in the HTDMA measurements, excluding this hypothesis. The presence of organic material in the atmosphere that is more hygroscopic than usually assumed cannot be excluded. However, the associated volume fractions in the particle phase should dominate in order to explain the measured hygroscopicities, which are highly uncommon and have never been reported at field measurements in the past.

Acknowledgements

This research has been co-financed by the European Union (European Social Fund – ESF) and Greek national funds through the Operational Program "Education and Lifelong Learning" of the National Strategic Reference Framework (NSRF) - Research Funding Program: THALES. Investing in knowledge society through the European Social Fund.

References

Aiken, A.C., Decarlo, P.F., Kroll, J.H., Worsnop, D.R., Huffman, J.A., Docherty, K.S., Ulbrich, I.M., Mohr, C., Kimmel, J.R., Sueper, D., Sun, Y., Zhang, Q., Trimborn, A., Northway, M., Ziemann, P.J., Canagaratna, M.R., Onasch, T.B., Alfarra, M. R., Prévôt, A.S.H., Dommen, J., Duplissy, J., Metzger, A., Baltensperger, U., and Jimenez, J.L.: O/C and OM/OC ratios of primary, secondary, and ambient organic aerosols with high-resolution time-of-flight aerosol mass spectrometry, Environ. Sci. Technol., 42, 4478–4485, 2008.

Bezantakos, S., Barmpounis, K., Giamarelou, M., Bossioli, E., Tombrou, M., Mihalopoulos, N., Eleftheriadis, K., Kalogiros, J., Allan, J. D., Bacak, A., Percival, C. J., Coe, H. and Biskos, G.: Chemical composition and hygroscopic properties of aerosol particles over the Aegean Sea, Atmos. Chem. Phys., 13, 11595–11608, 2013, doi:10.5194/acp-13-11595-2013.

Biskos, G., Paulsen, D., Russell, L.M., Buseck, P.R., Martin, S.T.: Prompt deliquescence and efflorescence of aerosol nanoparticles. Atmos. Chem. Phys. 6, 4633-4642, 2006a.

Bougiatioti, A., Fountoukis, C., Kalivitis, N., Pandis, S. N., Nenes, A. and Mihalopoulos N.: Cloud condensation nuclei measurements in the marine boundary layer of the eastern Mediterranean: CCN closure and droplet growth kinetics, Atmos. Chem. Phys., 9, 7053–7066, 2009.

Bougiatioti, A., Nenes, A., Fountoukis, C., Kalivitis, N., Pandis, S. N. and Mihalopoulos N.: Size-resolved CCN distributions and activation kinetics of aged continental and marine aerosol, Atmos. Chem. Phys., 11, 8791–8808, 2011, doi:10.5194/acp-11-8791-2011.

Chang, R. Y.-W., Slowik, J. G., Shantz, N. C., Vlasenko, A., Liggio, J., Sjostedt, S. J., Leaitch, W. R. and Abbatt, J. P. D.: The hygroscopicity parameter (κ) of ambient organic aerosol at a field site subject to biogenic and anthropogenic influences: relationship to degree of aerosol oxidation, Atmos. Chem. Phys., 10, 5047–5064, 2010, doi:10.5194/acp-10-5047-2010.

Clegg, S.L., Brimblecombe, P., Wexler, A.S.: Thermodynamic model of the system H^+- NH_4^+ - SO_4^{2-} - NO_3^- - H_2O at tropospheric temperatures. J. Phys. Chem. A, 102, 2137-2154, 1998b.

DeCarlo, P., Worsnop, D. R., Slowik, J. G., Davidovits, P., and Jimenez, J. L.: Characterizing Particle Morphology and Density Effects by Combining

Mobility and Aerodynamic Diameter Measurements. Aerosol Sci. Technol., 38, 1206–1222, 2004.

DeCarlo, P.F., Kimmel, J. R., Trimborn, A., Northway, M. J., Jayne, J. T., Aiken, A. C., M. Gonin, Fuhrer, K., Horvath, T., Docherty, K., Worsnop, D. R., and Jimenez, J. L.: Field-deployable, high-resolution, time-of-flight aerosol mass spectrometer. Analytical Chemistry, 78: 8281-8289, 2006.

Draxler, R.R., and G.D. Hess: Description of the HYSPLIT_4 modeling system. NOAA Tech. Memo. ERL ARL-224, NOAA Air Resources Laboratory, Silver Spring, MD, 24 pp, 1997

Draxler, R.R., and G.D. Hess: An overview of the HYSPLIT_4 modeling system of trajectories, dispersion, and deposition. Aust. Meteor. Mag., 47, 295-308, 1998

Draxler, R.R.: HYSPLIT4 user's guide. NOAA Tech. Memo. ERL ARL-230, NOAA Air Resources Laboratory, Silver Spring, MD, 1999.

Dusek, U., Frank, G. P., Massling, A., Zeromskiene, K., Iinuma, Y., Schmid, O., Helas, G., Hennig, T., Wiedensohler, A., and Andreae, M. O.: Water uptake by biomass burning aerosol at sub-and supersaturated conditions: closure studies and implications for the role of organics. Atmos. Chem.Phys. 11, no. 18, 9519-9532, 2011.

Fountoukis, C. and Nenes, A.: ISORROPIA II: a computationaly efficient thermodynamic equilibrium model for K^+-Ca^{2+}-Mg^{2+}- NH_4^+-SO_4^{2-}-NO_3^--Cl^--H_2O aerosols. Atmos. Chem. Phys., 7, 4639-4659, 2007.

Gysel, M., Crosier, J., Topping, D.O., Whitehead J.D.: Closure study between chemical composition and hygroscopic growth of aerosol particles during TORCH2. Atmos. Chem.and Phys., 7, 6131-6144, 2007.

Haywood, J. and Boucher, O.: Estimates of the direct and indirect radiative forcing due to tropospheric aerosols: a review. Rev. Geophys., 38, 513–543, 2000.

Henning, S., Ziese, M., Kiselev, A., Saathoff, H., Möhler, O., Mentel, T. F., Buchholz, A., Spindler, C., Michaud, V., Monier, M., Sellegri, K. and Stratmann, F.: Hygroscopic growth and droplet activation of soot particles: uncoated, succinic or sulfuric acid coated, Atmos. Chem. Phys., 12, 4525–4537, 2012, doi:10.5194/acp-12-4525-2012

Jung, J., Kim, Y. J., Aggarwal, S. G., Kawamura, K.: Hygroscopic property of water-soluble organic-enriched aerosols in Ulaanbaatar, Mongolia during the cold winter of 2007. Atmos. Environ. 45, 2722-2729, 2011

Irwin, M., Good, N., Crosier, J., Choularton, T. W. and McFiggans, G.: Reconciliation of measurements of hygroscopic growth and critical supersaturation of aerosol particles in central Germany, Atmos. Chem. Phys., 10, 11737–11752, 2010, doi:10.5194/acp-10-11737-2010.

Kerminen, V. M., Teinila, K., Hillamo, R., and Pakkanen, T.: Substitution of chloride in sea-salt particles by inorganic and organic anions, J. Aerosol Sci., 29, 929–942, 1998.

Knutson, E.O., Whitby, K.T.: Aerosol classification by electric mobility: Apparatus, theory, and applications. J. Aerosol Sci., 6, 443-451, 1975.

Kreidenweis, S.M., Petters, M.D., DeMott, P.J.: Single parameter estimates of aerosol water content, Environ. Res. Lett., 3, 035002, 2008.

Kostenidou, E., Pathak, R. K., and Pandis, S. N.: An algorithm for the calculation of secondary organic aerosol density combining AMS and SMPS data, Aerosol Sci. Technol., 41, 1002–1010, 2007.

Kostenidou, E., Florou, K., Kaltsonoudis, C., Tsiflikiotou, M., and Pandis, S. N., Sources and Chemical Processing of Organic Aerosol during the Summer in the Eastern Mediterranean. Atmos. Chem. Phys., 15, 11355-11371, 2015.

Kuwata, M., Shao, W., Lebouteiller, R. and Martin, S. T.: Classifying organic materials by oxygen-to-carbon elemental ratio to predict the activation regime of Cloud Condensation Nuclei (CCN), Atmos. Chem. Phys., 13, 5309–5324, 2013

Lanz, V. A., Alfarra, M. R., Baltensperger, U., Buchmann, B., Hueglin, C., and Prevot, A. S. H.: Source apportionment of submicron organic aerosols at an urban site by factor analytical modeling of aerosol mass spectra, Atmos. Chem. Phys., 7, 1503–1522, 2007.

Liu, X and Wang, j.: How important is organic aerosol hygroscopicity to aerosol indirect forcing?, Environ. Res. Lett., 5, 044010 (10pp), 2010, doi:10.1088/1748-9326/5/4/044010

Moore, Richard H., and Nenes, A.: Scanning flow CCN analysis - A method for fast measurements of CCN spectra. Aerosol Sci. Tech. 43.12, 1192-1207, 2009.

Moore, R.H., Cerully, K., Bahreini, R., Brock, C.A., Middelbrook, A.M., and Nenes, A.: Hygroscopicity and composition of California CCN during summer 2010, J. Geophys. Res., 117, D00V12, doi:10.1029/2011JD017352, 2012a.

Moore, R.H., Raatikainen, T., Langridge, J.M., Bahreini, R., Brock, C.A., Holloway, J.S., Lack, D.A., Middlebrook, A.M., Perring, A.E., Schwarz, J.P., Spackman, J.R., and Nenes, A.: CCN spectra, hygroscopicity, and droplet activation kinetics of Secondary Organic Aerosol resulting from the 2010 Deepwater Horizon oil spill, Environ. Sci. Technol., 46, 3093-3100, 2012b.

Ogren, J., Charlson, J.: Implications for models and measurementsof chemical inhomogeneities among cloud droplets, Tellus B, 44, 489–504, 1992.

Paatero, P. and Tapper, U.: Positive matrix factorization – a nonnegative factor model with optimal utilization of error-estimates of data values, Environmetrics, 5, 111–126, 1994.

Peng C. and Chan, C. K.: The water cycles of water-soluble organic salts of atmospheric importance, Atmos. Environ. 35, 1183-1992, 2001.

Petäjä, T., Kerminen, V.-M., Dal Maso, M., Junninen, H., Koponen, I. K., Hussein, T., Aalto, P. P., Andronopoulos, S., Robin, D., Hämeri, K., Bartzis, J. G., Kulmala, M.: Sub-micron atmospheric aerosols in the surroundings of Marseille and Athens: physical characterization and new particle formation, Atmos. Chem. Phys., 7, 2705–2720, 2007.

Petters, M.D. & Kreidenweis S.M.: A single parameter representation of hygroscopic growth and cloud condensation nucleus activity, Atmos. Chem. Phys., 7, 1961-1971, 2007.

Pringle K. J., Tost, H., Pozzer, A., Pöschl, U. and Lelieveld, J.: Global distribution of the effective aerosol hygroscopicity parameter for CCN activation, Atmos. Chem. Phys., 10, 5241-5255, 2010.

Rader, D.J., McMurry P.H.: Application of the tandem differential mobility analyzer to studies of droplet growth or evaporation, J. Aerosol Sci., 17, 771-787, 1986.

Roberts, G. C., and Nenes, A.: A continuous-flow streamwise thermal-gradient CCN chamber for atmospheric measurements. Aerosol Sci. Tech. 39.3, 206-221, 2005.

Stein, A.F., Draxler, R.R, Rolph, G.D., Stunder, B.J.B., Cohen, M.D., and Ngan, F.: NOAA's HYSPLIT atmospheric transport and dispersion modeling system, Bull. Amer. Meteor. Soc., 96, 2059-2077, 2015

Stock, M., Cheng, Y.F., Birmili, W., Massling, A., Wehner, B., Müller, T., Leinert, S., Kalivitis, N., Mihalopoulos, N. and Wiedensohler, A.: Hygroscopic properties of atmospheric aerosol particles over the Eastern Mediterranean: implications for regional direct radiative forcing under clean and polluted conditions, Atmos. Chem. Phys., 11, 4251-4271, 2011.

Stolzenburg, M. R. and McMurry, P.H.: TDMAFIT User's Manual, Particle Technology Laboratory, Department of Mechanical Engineering, Univercity of Minnesota, Minneapolis, 1-61, 1988.

Stolzenburg, M.R. & McMurry, P.H.: An ultrafine aerosol Condensation Nucleus Counter, Aerosol Sci. Technol., 14, 48-65, 1991.

Sueper, D.: ToF-AMS high resolution analysis software – Pika, online available at: http://cires.colorado.edu/jimenez-group/ ToFAMSResources/ToFSoftware, 2011.

Ulbrich, I. M., Canagaratna, M. R., Zhang, Q., Worsnop, D. R., and Jimenez, J. L.: Interpretation of organic components from positive matrix factorization of aerosol mass spectrometric data, Atmos. Chem. Phys., 9, 2891–2918, 2009.

Wex, H., Petters, M. D., Carrico, C. M., Hallbauer, E., Massling, A., McMeeking, G. R., Poulain, L., Wu, Z., Kreidenweis, S. M. and Stratmann, F.: Towards closing the gap between hygroscopic growth and activation for secondary organic aerosol: Part 1 – Evidence from measurements, Atmos. Chem. Phys., 9, 3987–3997, 2009.

Wu, Z. J., Nowak, A., Poulain, L., Herrmann, H., Wiedensohler, A.: Hygroscopic behavior of atmospherically relevant water-soluble carboxylic salts and their influence on the water uptake of ammonium sulfate, Atmos. Chem. Phys., 11, 12617–12626, 2011, doi:10.5194/acp-11-12617-2011.

Wu, Z. J., Poulain, L., Henning, S., Dieckmann, K., Birmili, W., Merkel, M., van Pinxteren, D., Spindler, G., Müller, K., Stratmann, F. Herrmann, H. and Wiedensohler A.: Relating particle hygroscopicity and CCN activity to chemical composition during the HCCT-2010 field campaign, Atmos. Chem. Phys., 13, 7983–7996, 2013, doi:10.5194/acp-13-7983-2013.

Supplement

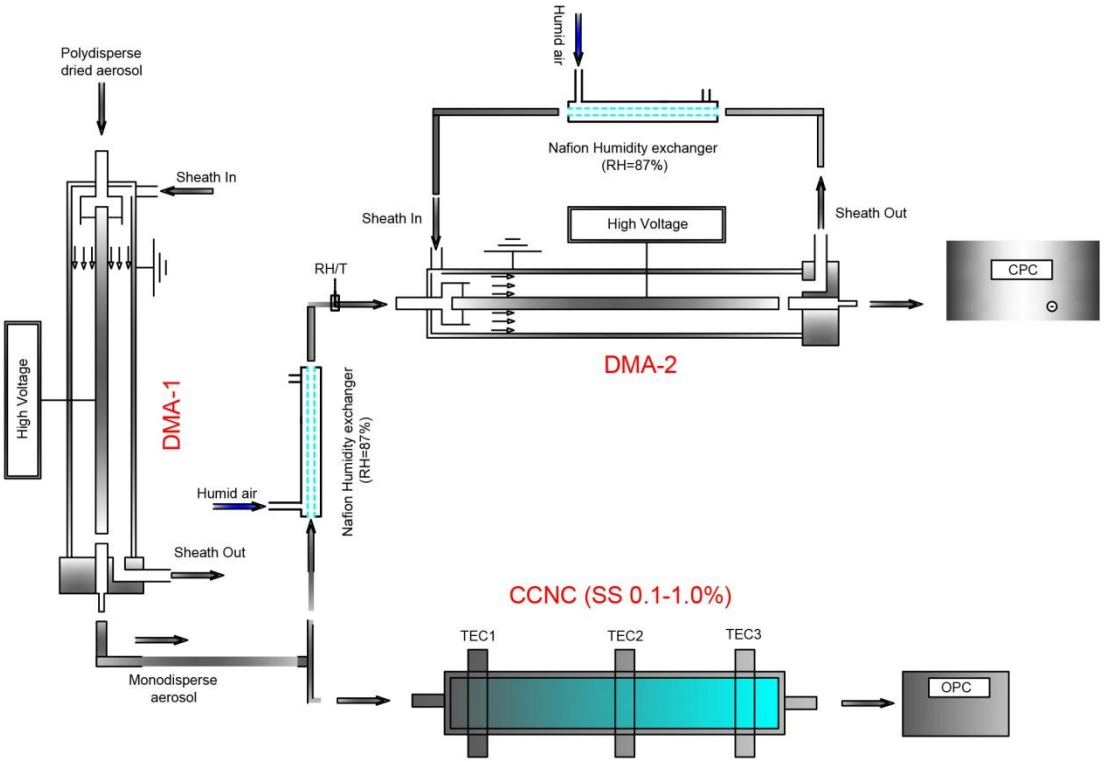

Fig S3.1. Experimental setup of HTDMA-CCNC combo. In brief, ambient air was sampled at a rate of 1.8 lpm. Particles passed through a drier, a ^{85}Kr neutralizer and DMA-1, where particles of 40, 60, 80, 100 and 120 nm were selected. 0.3 lpm of the monodisperse flow downstream DMA-1 was passed through a nafion humidifier, where its RH was increased to 87 ±2%, before measured by DMA-2 and the CPC. The rest of the monodisperse flow (1.5 lpm) was directed through the CCNC, where it was super-saturated from 0.1 to 1.0% with water vapors. Particles that activated as Cloud Condensation Nuclei were detected downstream by an Optical Particle Counter.

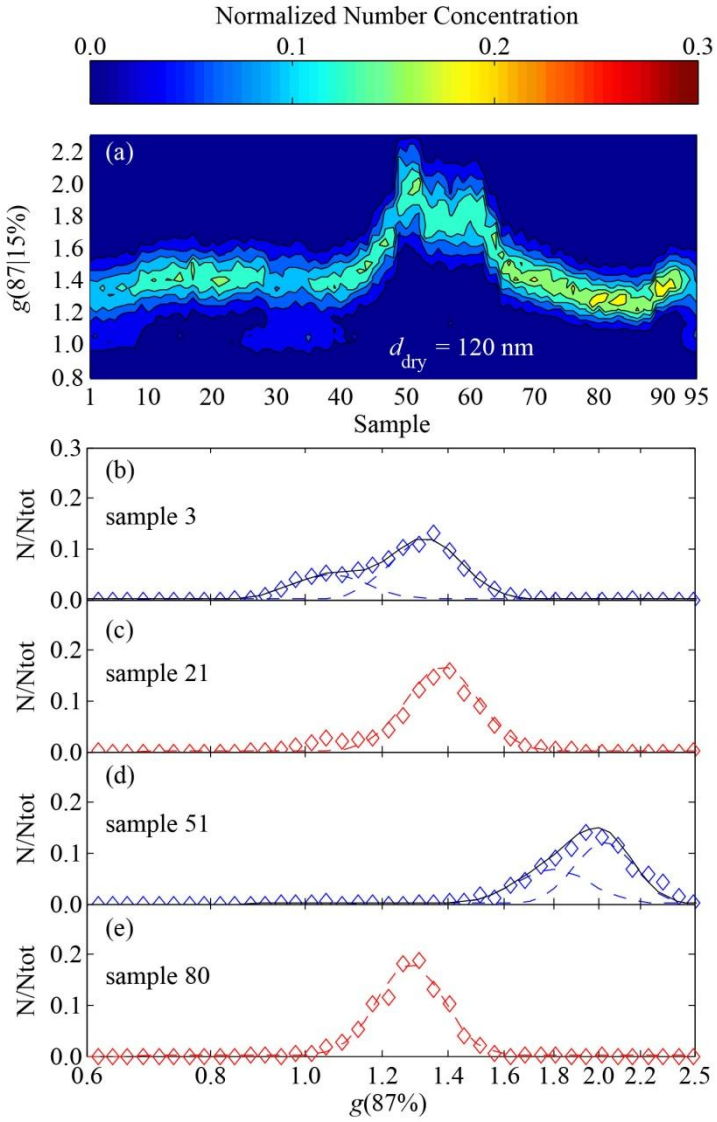

Fig S3.2. Examples of growth factor distributions of sampled particles having 120 nm dry mobility diameters, when exposed at 87±2% RH inside the HTDMA (**a**) and results of the inversion algorithm for selected samples (**b-e**).

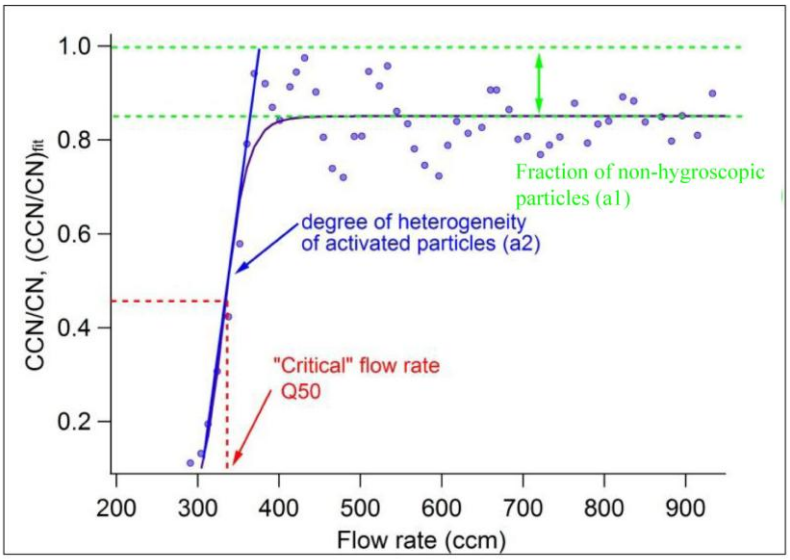

Fig S3.3. Example of CCN activation ratio for monodisperse particles of 120 nm dry mobility diameters, when exposed at super-saturated conditions ranging from 0.1 to 1.0 inside the CCN.

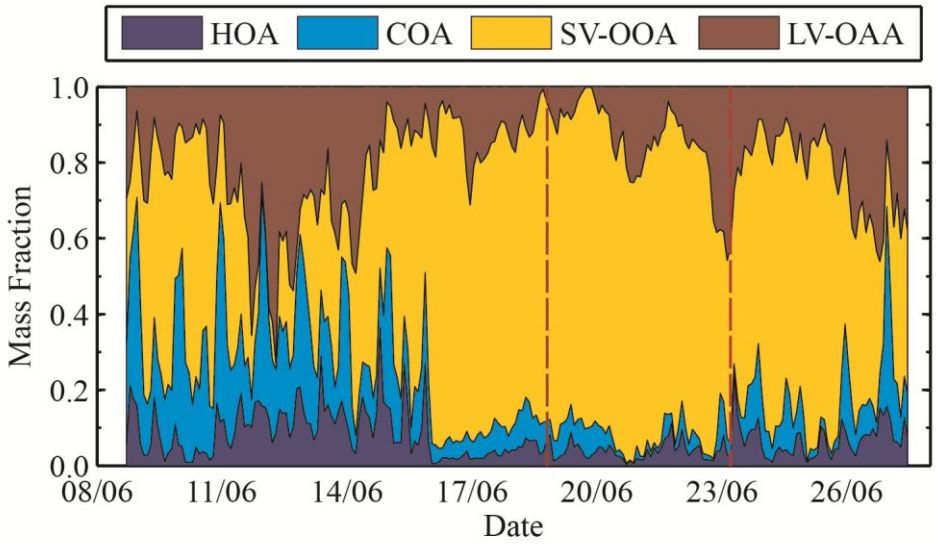

Fig S3.4. Relative mass fractions of the organic material measured by the HR-ToF-AMS categorized according to the Positive Matrix Factorization (PMF) in Patras. HOA, COA, SV- and LV- OOA stands for hydrocarbon like organic aerosol, cooking organic aerosol, semi-volatile oxygenated organic aerosol and low volatility organic aerosol. Red dashed lines indicate the end of the first and the start of the third sub-period, respectively.

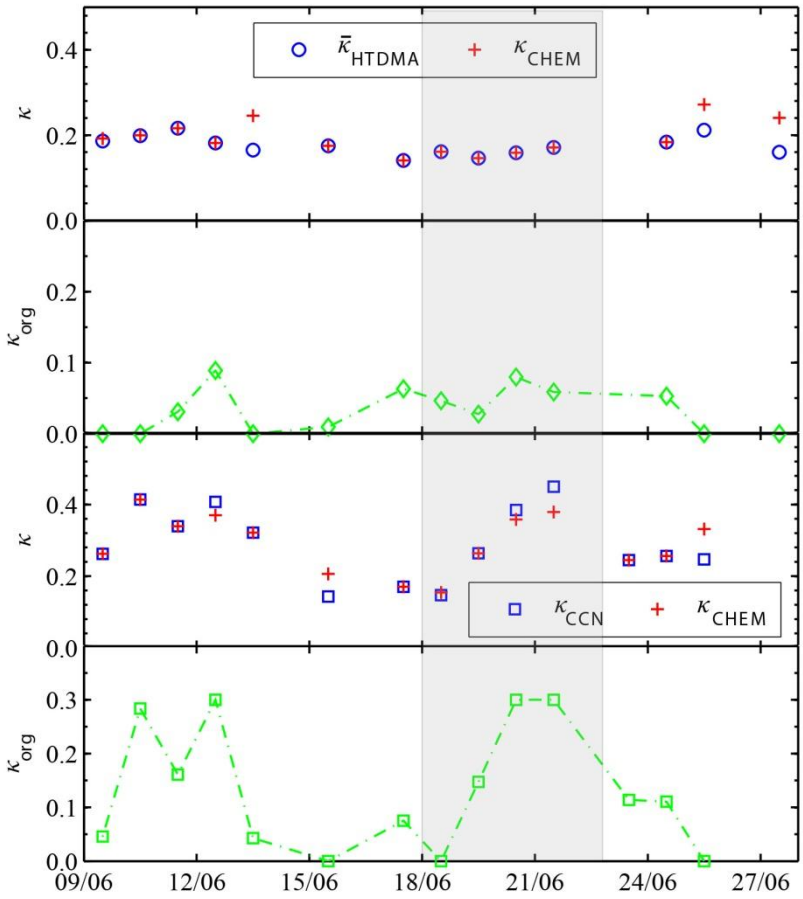

Fig S3.5. Comparison between predicted κ_{CHEM} determined by the filter samples with measured $\bar{\kappa}_{HTDMA}$ and κ_{CCN} in Patras. κ_{CHEM} was predicted by applying the κ-Köhler theory on the bulk chemical composition of the $PM_{2.5}$ particles. The hygroscopic parameter of the organic fraction (κ_{org}) was estimated by fitting the predicted κ_{CHEM} values to the measurements by varying κ_{org} from 0.0 to 0.3. The grayed area marks the second sub-period.

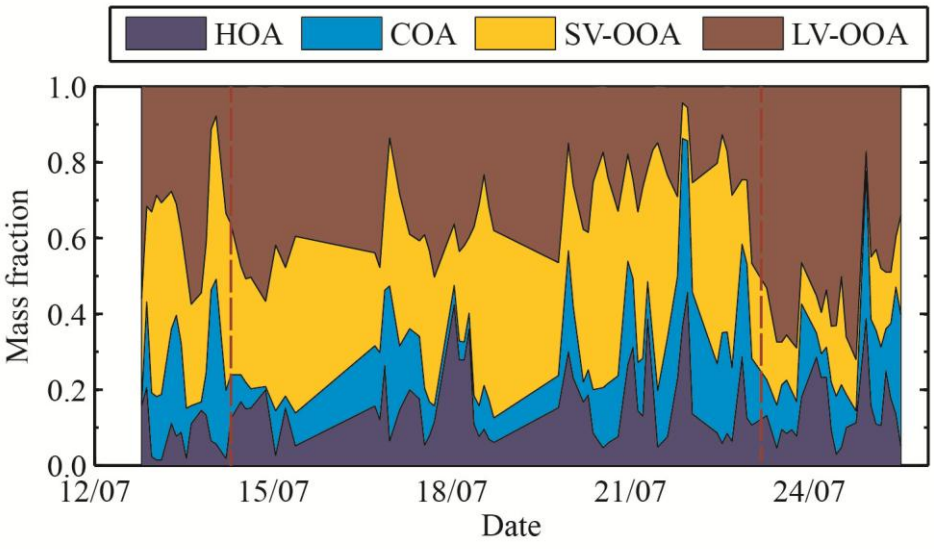

Fig S3.6. Relative mass fractions of the organic material measured by the HR-ToF-AMS, categorized according to the Positive Matrix Factorization (PMF) in Athens. HOA, COA, SV- and LV- OOA stands for hydrocarbon like organic aerosol, cooking organic aerosol, semi-volatile oxygenated organic aerosol and low volatility organic aerosol. Red dashed lines indicate the end of the third and the start of the fifth sub-period, respectively.

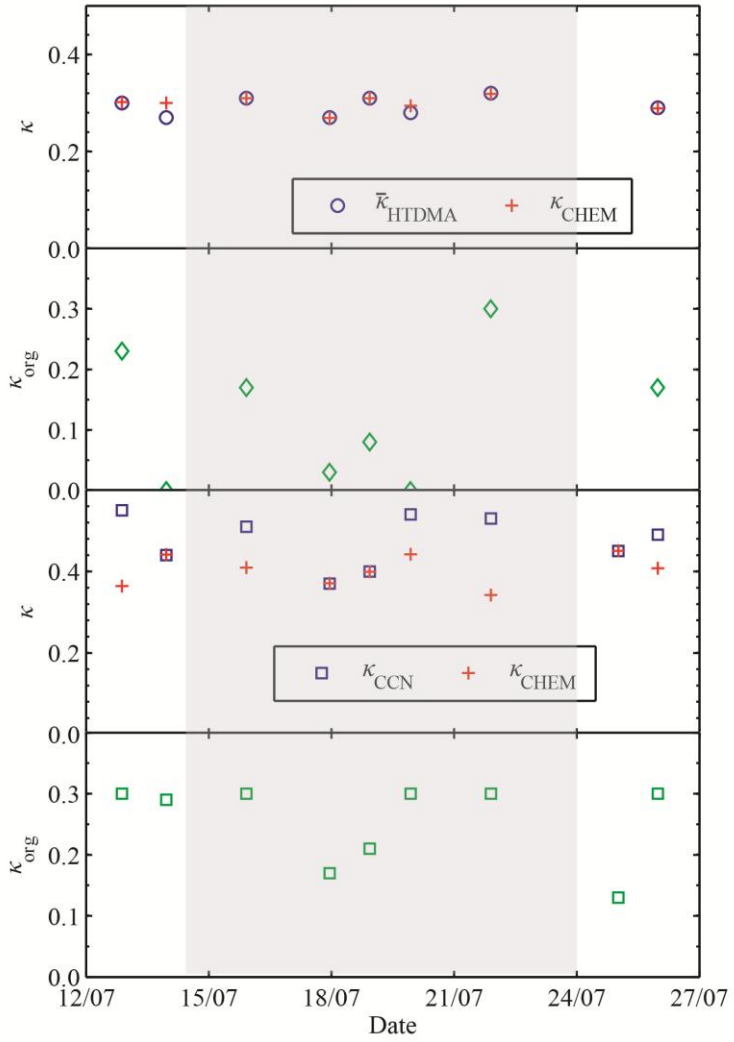

Fig S3.7. Comparison between predicted κ_{CHEM} determined by the filter samples with measured $\bar{\kappa}_{HTDMA}$and κ_{CCN} in Athens. κ_{CHEM} was predicted by applying the κ-Köhler theory on the bulk chemical composition of the $PM_{2.5}$ particles. The hygroscopic parameter of the organic fraction (κ_{org}) was estimated by fitting the predicted κ_{CHEM} values to the measurements by varying κ_{org} from 0.0 to 0.3. The grayed area marks the fourth sub-period.

Table S3.1. Median values and range (in brackets) of the estimated aerosol and organic fraction's, hygroscopic parameters (κ_{CHEM} and κ_{org}) at different saturation (*S*) conditions in Patras. For the estimation, κ_{CHEM} was fitted to the measured hygroscopic parameters of particles having dry mobility diameter of 120 nm by varying κ_{org}.

S	Variable	P1	P2	P3
sub-saturation	κ_{CHEM}*	0.19 (0.14-0.25)	0.16 (0.15-0.18)	0.24 (0.18-0.27)
	κ_{org}*	0.02 (0.00-0.09)	0.05 (0.03-0.08)	0.00 (0.00-0.05)
Super-saturation	κ_{CHEM}*	0.29 (0.15-0.41)	0.26 (0.15-0.38)	0.29 (0.26-0.33)
	κ_{org}*	0.06 (0.00-0.30)	0.13 (0.00-0.30)	0.05 (0.00-0.11)

*Estimation using off-line chemical composition measurements of $PM_{2.5}$ (24-h filters).

Table S3.2. Median values and range (in brackets) of the estimated aerosol and organic fraction's, hygroscopic parameters (κ_{CHEM} and κ_{org}) at different saturation (*S*) conditions in Athens. For the estimation, κ_{CHEM} was fitted to the measured hygroscopic parameters of particles having dry mobility diameter of 120 nm by varying κ_{org}.

S	Variable	P3	P4	P5
sub-saturation	κ_{CHEM}*	0.30 (0.30-0.30)	0.31 (0.27-0.32)	0.35 (0.29-0.41)
	κ_{org}*	0.12 (0.00-0.23)	0.08 (0.00-0.30)	0.17 (0.17-0.17)
Super-saturation	κ_{CHEM}*	0.40 (0.36-0.44)	0.40 (0.34-0.44)	0.43 (0.41-0.45)
	κ_{org}*	0.30 (0.29-0.30)	0.30 (0.17-0.30)	0.22 (0.13-0.30)

*Estimation using off-line chemical composition measurements of $PM_{2.5}$ (24-h filters).

PART II: Development of Techniques for the Improvement of the Methods Used for Determining Aerosol Physicochemical Properties

4. Relative Humidity Non-Uniformities in Hygroscopic Tandem Differential Mobility Analyzer Measurements

S. Bezantakos[1,2], L. Huang[3], K. Barmpounis[3], S. T. Martin[4] and G. Biskos[,5,6*]

[1]*Department of Environment, University of the Aegean, Mytilene 81100, Greece*

[2]*Institute of Nuclear Technology and Radiation Protection, NCSR Demokritos, 15310 Ag. Paraskevi, Attiki, Greece*

[3]*Faculty of Applied Sciences, Delft University of Technology, Delft 2628-BL, The Netherlands*

[4]*School of Applied Sciences, Harvard University, Cambridge, Massachusetts, USA*

[5]*Faculty of Civil Engineering and Geosciences, Delft University of Technology, Delft 2628-CN, The Netherlands*

[6]*Energy Environment and Water Research Center, The Cyprus Institute, Nicosia 1645, Cyprus*

Email: G.Biskos@tudelft.nl

Submitted: December 2015

Journal of Aerosol Science

*To whom correspondence should be addressed

Abstract

Hygroscopic Tandem Differential Mobility Analyzers (HTDMAs) are widely used to measure the water uptake characteristics of aerosol particles. As has been shown experimentally in the past, potential differences in the relative humidity (RH) between the aerosol and the sheath flow of the second Differential Mobility Analyzer (DMA) can lead to erroneous estimates of the apparent hygroscopic behavior of the sampled particles. A prompt phase transition, for example, may become smeared and be erroneously interpreted as non-prompt. Using a particle-tracking model, here we simulate the trajectories and the state of the particles classified in a DMA with non-uniform RH and temperature profiles. Our simulations corroborate earlier observations proving that such an experimental artifact can induce particle growth within the second DMA. Given the importance of maintaining uniform RH and temperature inside the second DMA of HTDMA systems and the limitations of existing RH and temperature sensors, we further provide suggestions for the operation of HTDMA systems.

4.1. Introduction

The extent to which atmospheric particles can take up water (i.e., their hygroscopicity) affects their optical behavior and in turn the radiative properties of the atmosphere (Haywood and Boucher, 2000; Ogren and Charlson, 1992). In addition, hygroscopicity can influence the health effects of inhaled particles by changing their size and therefore their deposition patterns in the human respiratory system (Chen and Lee, 1999). Knowledge of the hygroscopicity of airborne particles is thus of particular importance for determining their environmental impacts (Anastasio et al., 2001).

Many techniques have been employed to measure the hygroscopic properties of aerosol particles (cf. McMurry, 2000). Electrodynamic Balances (EDBs; Peng and Chan, 2001) measure changes in the mass of micron-sized particles as a function of the aerosol relative humidity (RH). The water uptake characteristics of ultrafine particles can be probed by using Tandem Differential Mobility Analyzers (TDMAs; Rader and McMurry, 1986), which can measure changes in the electrical mobility of the particles with high precision when exposed to different conditions. Apart from the amount of water that the particles can take up at any given RH, these systems can also determine the deliquescence and the efflorescence RH (DRH and ERH, respectively; Martin, 2000) of the sampled particles (e.g. Biskos et al., 2006a, 2006b).

The hygroscopic properties of inorganic aerosol particles having diameters larger than 50 nm were determined in several laboratory studies (e.g. Tang et al., 1977; Tang et al., 1978; Tang and Munkelwitz, 1993; Tang et al., 1997). In these studies, the observed phase transitions were prompt (i.e. spontaneous), while the measured hygroscopic growth factors agreed within experimental uncertainty with theoretical predictions. Hämeri et al. (2000), who was the first to measure the hygroscopic properties of sub-50-nm $(NH_4)_2SO_4$ particles using an HTDMA, reported that they did not spontaneously transform from the solid/dry to the aqueous solution state but instead exhibited a gradual increase of their size when exposed to increasing RHs close to their DRH value. Mirabel et al. (2000) provided a possible theoretical explanation on the non-prompt deliquescence of inorganic salt nanoparticles by assuming coexistence of the solid with the aqueous phase during the transition. The non-prompt particle deliquescence, however, did not agree with predictions by thorough theoretical models developed later by Djikaev et al. (2001), Russell and Ming (2002), and Topping et al. (2005). In view of this disagreement, Biskos et al. (2006b), Park et al. (2009) and Hu et al. (2010) provided new sets of HTDMA

measurements with sub-50-nm $(NH_4)_2SO_4$ particles, which in contrast to the observations reported by Hämeri et al. (2000) showed that their phase transitions are prompt. The main difference between the HTDMA measurements reported in these two experimental studies was the matching between the RH of the aerosol and that of the sheath flow in the second classifier.

Here, we investigate the effects of RH and temperature non-uniformities by predicting the hygroscopic growth of the particles within the second DMA of the HTDMA system. To do so we calculate temperature and RH profiles within the second DMA and use a particle-tracking model, coupled with a module for predicting the size of the particles along their migration paths within the DMA. The results of the simulations are compared with earlier experimental observations.

4.2. The Hygroscopic Tandem DMA

Figure 4.1 shows the main components of the HTDMA system for the dataset collected by Biskos et al. (2006b). It consisted of two Differential Mobility Analyzers (DMAs; Knutson and Whitby, 1975), a flow humidification system, and an ultrafine Condensation Particle Counter (uCPC; Stolzenburg and McMurry, 1991).

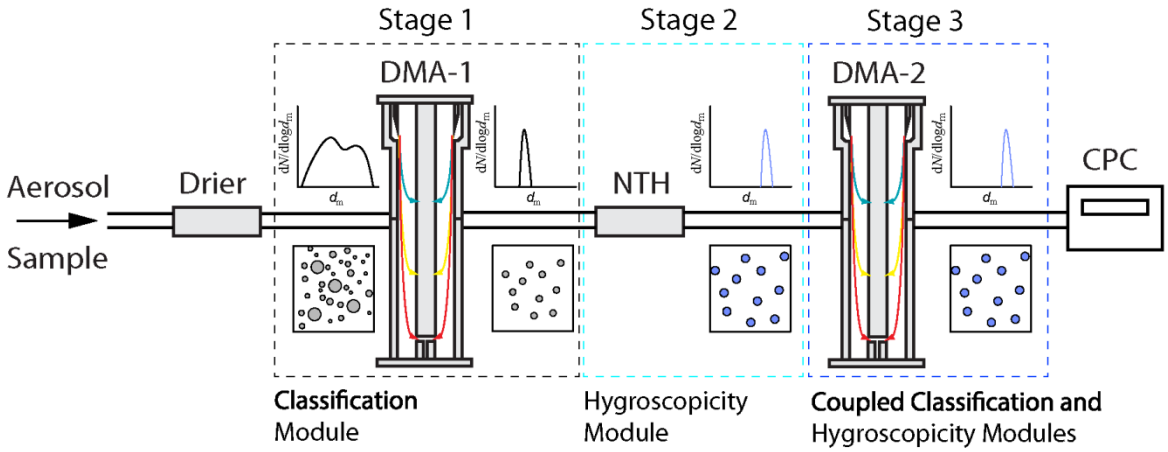

Fig. 4.1: Schematic layout of the HTDMA system and the associated modules of the numerical model.

The particles in the sample flow were initially dried and passed through a bipolar charger before entering the first DMA (DMA-1). The monodisperse aerosol flow downstream DMA-1 was then exposed to elevated RH conditions inside the humidifier. The second DMA (DMA-2), which was also operated with a sheath flow of elevated RH, and the uCPC were used for measuring the size distribution of the

particles downstream the humidifier. Consequently, any changes in the size of the particles caused by water uptake, could be detected and quantified (cf. sect. 4.3.1).

To avoid changes in particle size due to water evaporation or condensation, the RH of the aerosol should remain constant downstream the aerosol humidifier. Without special care, however, the RH of the aerosol (RH_a) and that of the sheath (RH_{sh}) flow can become mismatched, yielding a non-uniform RH profile within DMA-2. RH non-uniformities can also be caused by temperature variations within the second DMA. To minimize non-uniformities in the experimental setup during the measurements, heat-isolating materials (e.g., Biskos et al., 2006), covering the DMAs with heating jackets (e.g., Hämeri et al., 2000), or immersing them in liquid baths (e.g., Hennig et al., 2005) can be used.

4.3. Numerical model

The HTDMA system and the numerical model simulating its performance can be separated into three stages (cf. Fig. 4.1):

1. the selection of monodisperse aerosol particles by DMA-1;

2. the humidification of the monodisperse aerosol by the humidification system; and

3. the measurement of the mobility distribution of the monodisperse/humidified particles by DMA-2 and the uCPC.

Because the first DMA is operated at dry conditions, no particle water uptake takes place, and the theoretical transfer function can be used to predict the electrical mobility distribution of the aerosol particles at the outlet. The singly charged particles downstream DMA-1 have almost the same size, with a midpoint electrical mobility Z_m^* given by (Flagan, 2001):

$$Z_m^* = \frac{(Q_{\mathrm{sh}} + Q_{\mathrm{ex}}) \times ln\left(\frac{r_2}{r_1}\right)}{4\pi V L}, \tag{4.1}$$

where r_1, r_2, and L are the characteristic geometric dimensions of DMA-1, Q_{sh} and Q_{ex} are respectively the sheath and exhaust flows (which in our case are the same with those on DMA-2; cf. Table 4.1), and V is the voltage required for DMA-1 to select particles of any given mobility diameter. To estimate the diameter of the particles selected by the DMA one needs to equate Eq. 4.1 with (Hinds,1999):

$$Z_p = \frac{neC_c}{3\pi\eta d_{\mathrm{p}}}. \tag{4.2}$$

Here n is the number of elementary charges, e is electron charge (1.6×10^{-19} C), η is the air viscosity (1.81×10^{-5} kg/ms), d_p is the desired particle diameter, and C_c is the Cunningham slip correction factor (cf. supplement sect. S4.1).

Table 4.1: Experimental Parameters used in the numerical model

Type	Parameter	Value	Unit
Design Parameters	r_2	1.905	[cm]
	r_1	0.937	[cm]
	L	4.987	[cm]
Operation Parameters	Q_{sh}	15	[lpm]
	Q_a	1.5	[lpm]
	$\mathrm{RH_{sh}}$	$73 - 86$	[%]
	$\mathrm{RH_a}$	$\mathrm{RH_{sh}} = \mathrm{RH_a} + 3\%$	$[-]$

The RH of the monodisperse aerosol downstream DMA-1 is increased to a fixed value by passing the flow through a nafion-tube humidity exchanger (i.e., deliquescence-mode experiments; cf. Biskos et al., 2006b). To predict the amount of water taken up by the particles at RH values below the DRH we employ an adsorption model, while for RH ≥ DRH we use Köhler theory. Details of these models are provided in sect. 4.3.1.

While being classified through DMA-2, the monodisperse/humidified particles can change in size due to water uptake or release induced by differences in the RH conditions they are exposed to, which in turn depend on temperature variances within the column. As a result, the particles classified by DMA-2 can exhibit an apparent size that is between their size at the entrance and that just before they exit through the monodisperse particle slit of the classifier. To simulate the simultaneous classification and water uptake/release of the particles within DMA-2 we developed a particle-tracking model to capture changes in particle size (due to water uptake and release) along their migration path (cf. sect. 4.3.1).

The flow, temperature, and RH profiles within DMA-2 were simulated by a 2D axisymetric numerical model developed using COMSOL Multiphysics® (cf. supplement sect. S4.2). The voltage of DMA-2 in the model was stepwise changed. This is representative of DMAs operated in a scanning mode when the residence time of the particles in the classification zone of the DMA (i.e., 0.15 s here) is much shorter than the total scanning time (i.e.120 s, used in Biskos et al., 2006b). For the cylindrical DMA used in the simulation, the axial electric field strength (E_z) was

assumed to be zero, while its radial component (E_r) was calculated for each operating voltage (V) by:

$$E_r = \frac{V}{r ln\left(\frac{r2}{r1}\right)}, \quad (4.3)$$

where r_2 and r_1 are respectively the outer and inner radii of the DMA and r is the radial position of each particle within DMA-2.

The incremental steps on the trajectories of the diffusing particles inside DMA-2 operated with fixed voltage and flows were calculated as follows:

$$\Delta_r = \left(u_r(r,z) + Z_p\, E_r(r,z)\right)\Delta t + l_{diff,r} \quad (4.4)$$

$$\Delta_z = \left(u_z(r,z)\right)\Delta t + l_{diff,z} \quad (4.5)$$

where r and z denote the radial and axial space components, respectively, Z_p is the electrical mobility of the particles (cf. Eq. 4.2), while $l_{diff,r}$ and $l_{diff,z}$ are the radial and axial displacements of the particles from their deterministic trajectories due to diffusion during the calculation time step Δt. This diffusional displacement is estimated by (cf. Hagwood 1999 for more details):

$$l_{diff,r}, l_{diff,z} \sim Norm\left(0, \sqrt{2D_p\,\Delta t}\right), \quad (4.6)$$

where D_p is the particle diffusion coefficient in air (cf. supplement).

The number of particles that exit through the monodisperse outlet of DMA-2 at every stepping voltage in the simulations was used to determine the geometric mean mobility diameter of the humidified aerosol particles.

4.3.1 Particle Hygroscopicity Module

For RH ≥ DRH, the aerosol particles take up water and spontaneously become aqueous solution droplets the diameter of which can be predicted by Köhler theory. For large dry particles (i.e., d_p > 100 nm), the size of the resulting droplets can be predicted by (Biskos et al., 2006a):

$$d_p(\mathrm{RH}) = \left(\frac{100\rho_s}{w_t(a_w)\rho(w_t(a_w))}\right)^{1/3} d_{p,dry}, \quad (4.7)$$

where ρ_s is the density of the solid particle, w_t is the weight percent of solute in the aqueous particle, ρ is the density of the droplets, and $d_{p,dry}$ is the size of the dry

particles. The terms w_t and ρ depend on water activity a_w, taken as a_w = RH/100, neglecting any curvature effects. Surface tension effects become important for droplets having diameters smaller than ca. 100 nm, and therefore a correction is made to the relationship between water activity and RH, as follows:

$$a_w = \frac{RH}{100} \times \exp\left(\frac{4M_w\sigma_{aq}(w_t(a_w))}{RT\rho_w d_p(\mathrm{RH})}\right). \quad (4.8)$$

Here, σ_{aq} is the surface tension of the aqueous droplet, M_w is the molar weight of water, R is the universal gas constant, and T is the absolute temperature. The parameters for ρ_s, w_t, T, M_w, and ρ_w , as well as expressions for a_w, ρ_w and σ_{aq}, used in Eqs. 4.7 and 4.8 are provided in Table 4.2.

Table 4.2: Computational Parameters used in the numerical model

Type	Para-meter	Description	Value	Unit
Physical Parameters	w_t	weight percent of solute in the aqueous particle	10-90	[%]
	R	Universal gas constant	8.3145	[J K^{-1} mol $^{-1}$]
	T	Absolute temperature	290-296	[K]
	M_w	Molar weight of water	18	[gr mol $^{-1}$]
	ρ_s	Density of solid $(NH_4)_2SO_4$	1770	[kg m^{-3}]
	ρ_w	Density of water	$\rho_w = 997.1 + \sum A_i w_t^i$	[kg m^{-3}]
	a_w	Water activity	$A_1 = 5.920$ $A_2 = -5.036 \times 10^{-3}$ $A_3 = 1.024 \times 10^{-5}$ $a_w = 1.0 + \sum C_i w_t^i$ $C_1 = -2.715 \times 10^{-3}$ $C_2 = 3.113 \times 10^{-5}$ $C_3 = -2.336 \times 10^{-6}$ $C_4 = 1.412 \times 10^{-8}$	[−]
	σ_{aq}	Surface tension of aqueous droplet	$\sigma_{aq} = 0.072 + \frac{0.0234 w_t}{100 - w_t}$	[N m^{-1}]
Particle Parameters	$d_{m,dry}$	Electrical mobility diameter of dry particle	10	[nm]
	χ	Particle shape factor	1.02	[−]
	DRH	Deliquescence Relative Humidity	79.9%	[−]
FHH adsorption	A		0.2491	[−]
	B		0.1500	[−]

Parameters	$d_{w,ml}$	Water monolayer thickness	0.19	[nm]

At RH values below the DRH, the particles grow slightly due to the amount of water adsorbed on their surface. To predict the number of water monolayers we use the Frenkel-Halsey-Hill (FHH) isotherm, which was parameterized using our experimental observations when $RH_a = RH_{sh}$. The FHH isotherm is given by:

$$\ln\left(\frac{1}{RH/100}\right) = \frac{A}{\Theta^B}, \quad (4.9)$$

where Θ is the number of adsorbed water monolayers (surface coverage), which is not necessarily an integer. Terms A and B = 0.1500 are constants that are estimated to be respectively 0.2491 and 0.01500 when fitting Eq. 4.9 to the HTDMA measurements using the 10-nm particles. The predicted particle growth at RH < DRH is then determined by:

$$d_p(RH) = d_{p,dry} + \left(\Theta \times 2d_{w,ml}\right) \quad (4.10)$$

where $d_{w,ml}$ = 0.19 nm is the water monolayer thickness reported for NaCl nanoparticles by Stöckelmann and Hentschke (1999) and assumed to be valid for $(NH_4)_2SO_4$ particles.

One way to express the change in particle size caused by water uptake is the hygroscopic growth factor, given by:

$$g(RH) = \frac{d_p(\mathrm{RH})}{d_{p,dry}}. \quad (4.11)$$

The aqueous droplets after deliquescence are considered to have spherical shape. Dry salt particles are crystalline and can have a polyhedron shape depending on production conditions (Wang et al., 2010). To take possible shape changes into account when estimating the hygroscopic growth factor using Eq. 4.11, the measured dry mobility diameter $d_{m,dry}$ needs to be converted to a volume equivalent dry diameter $d_{p,dry}$, using:

$$d_{p,dry} = \frac{d_{m,\mathrm{dry}}\, C_\mathrm{c}\left(Kn(d_{p,dry})\right)}{\chi\, C_\mathrm{c}\left(Kn(d_{m,dry})\right)}, \quad (4.12)$$

where χ is the dynamic shape factor, C_c is the Cunningham slip correction factor, and *Kn* is the Knudsen number. For spherical particles (i.e., for the resulting droplets when RH > DRH), by definition $\chi = 1$.

4.4. Results and Discussion

The particle trajectories of initially dry 10-nm $(NH_4)_2SO_4$ particles classified through DMA-2 operated with sheath and aerosol flow rates of 15 and 1.5 lpm, respectively, and $RH_{sh} = RH_a + 3\%$ (i.e., mismatched RHs) were simulated first. The DRH of $(NH_4)_2SO_4$ particles was assumed to be 79.9% (Tang and Munkelwitz, 1993), whereas a shape factor of 1.02 is used to take into account their slightly non-spherical shape at dry conditions, apparently resulting in marginally smaller spherical particles at intermediate RH conditions due to restructuring caused by water adsorption (Biskos et al., 2006b). Mixing a sheath and an aerosol flow with different RHs yields a non-uniform RH profile within DMA-2, and therefore the particles can experience size changes as they migrate along the classification region of the tube (cf. Fig. 4.2).

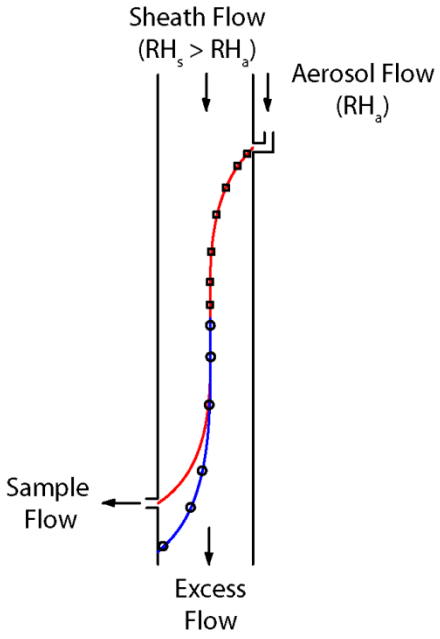

Fig. 4.2: Illustration of the trajectories of aerosol particles exposed to a non-uniform RH profile in DMA-2. Particles are in a solid state (square symbols) until they are exposed to RH > DRH conditions, at which point they transform into droplets (circle symbols).

Figure 4.3 shows the estimated hygroscopic growth factors *g* from the simulations considering mismatched RH between the aerosol and sheath flow (i.e.,

RH_{sh} = RH_a + 3%) and uniform temperature within DMA-2, in comparison with respective measurements reported by Biskos et al. (2006b). Although the non-prompt deliquescence behavior is captured by these first simulations, to improve agreement between predicted and measured growth factors we had to consider a variable temperature difference between the inner and the outer electrode of DMA-2 (cf. Fig. 4.3b), which further enhanced RH non-uniformity compared to the first simulations. More specifically, we assumed that the temperature difference between the inner rod and the outer electrode of DMA-2 varied according to $\Delta T = 0.49 \times RH_{sh} - 40$. Deviations of ± 0.8 K in this RH_{sh}-dependent temperature difference were allowed for matching the simulated to the experimental results within less than 2% difference. The theoretical deliquescence-mode hygroscopicity curve for 10-nm $(NH_4)_2SO_4$ particles having a shape factor of 1.02 is also shown in Fig. 4.3a for comparison (cf. black dashed line). These predictions correspond to the ideal case of RH_{sh} = RH_a and uniform temperature within DMA-2.

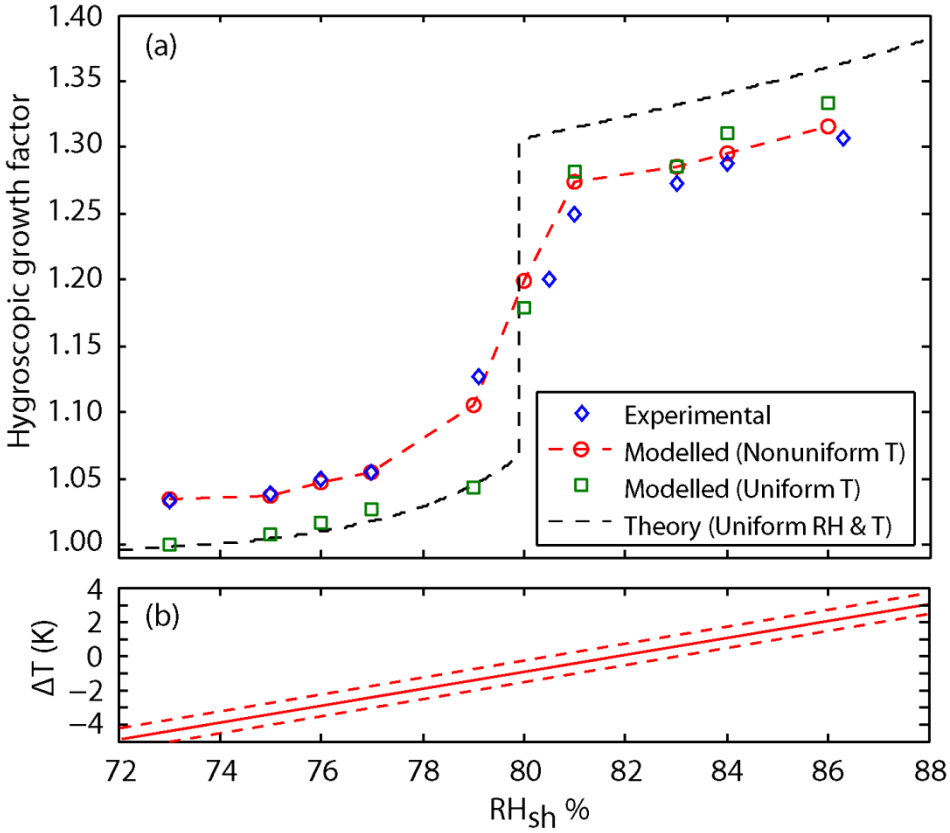

Fig. 4.3: Calculated mobility-diameter hygroscopic growth factors of 10-nm ammonium sulfate particles in comparison with experimental observations of Biskos et al. (2006a), when RH_{sh} = RH_a + 3%. The theoretical (i.e., FHH isotherm and Köhler theory) hygroscopic growth curve for uniform RH

and temperature conditions is also provided as a reference. Predictions correspond to uniform and non-uniform temperature conditions inside DMA-2 (**a**), while in the latter case the temperature of its inner electrode changes with respect to RH following the linear equation $\Delta T = 0.49 \times RH_{sh} - 40$ (**b**). Deviations from linearity of the order of ± 0.8 K (dashed lines) were allowed for better matching (i.e., less than 2% of accuracy) to the experimental results.

In the case of mismatched RHs and uniform temperature conditions, the hygroscopic growth factors predicted by the numerical model at RH < DRH are ca. 2 to 3% lower than the measurements reported by Biskos et al. (2006b). At RH conditions near the DRH, however, this difference increases to more than 5%. It decreases to 3% or less above the DRH. Comparing the numerical predictions with the theoretically predicted growth factors (black dashed line in Fig. 4.3a) indicates that small RH non-uniformities within DMA-2 can lead to significant deviations of measured *g* from reality only at RH values around and above the DRH.

At mismatched RHs and non-uniform temperature conditions, the simulated *g* values are fitted better to the experimental observations (i.e., within less than 2% difference), throughout the entire RH range (i.e., below and above the DRH). In contrast to the first simulations (i.e., mismatched RH and uniform temperature), a steeper increase of *g* with respect to RH at values below and in the vicinity of the DRH is observed. This better agreement between simulations and measurements can be attributed to the specifics of the RH profiles inside DMA-2. For example, when RH_{sh} = 80% and RH_a = 77% under uniform temperature conditions, particles start experiencing a non uniform RH profile only close to the inlet (cf. Fig. S4.3a). On the other hand, when a temperature difference of 1 K between the inner and outer electrodes of DMA-2 is applied, particles experience a non uniform RH not only close to the inlet but also close to inner electrode and particularly in the vicinity of the monodisperse outlet (cf. Fig. S4.3b).

Temperature differences between the two electrodes of the DMA resulting from environmental disturbances are considered here to illustrate the effect of temperature non-uniformities within DMA-2. Several other reasons, such as temperature differences between other parts of the DMA (e.g., the top and bottom of the classification column) or the sheath and the sample aerosol streams, can also induce similar temperature and RH non-uniformities. Such temperature differences are possible even in well-insulated DMAs or systems having active temperature

control, and a considerable amount of time (of the order of 30 min or even more) can be required to reduce them. This time period is demonstrated by the simulations of the evolutions of the temperature profiles inside a DMA (cf. Fig. S4.4 and associated discussion in the sect. S4.3 of the supplement), and shown by experimental tests (Dupplissy et al., 2009).

RH non-uniformities caused by either deliberately or accidentally caused mismatched RH conditions due to temperature non uniformities result in more pronounced apparent non-prompt deliquescence for the smaller particles classified through the DMA. The smaller particles are more diffusive and have a higher probability of crossing areas of higher RH than the nominal (i.e., measured RH) during deliquescence-mode experiments. For example, the diffusion coefficient of a 10-nm particle is ca. 22.5 times higher than that of a 50-nm particle (cf. Eqs. S4.1 and S4.2 in sect. S4.1 of the supplement). For the 10-nm particles, the resulting distribution describing particle diffusional displacement indicates that there is a 32% probability (i.e., more than 1 standard deviation) that they deviate from their deterministic trajectories by more than 0.13 mm. At mismatched RH conditions near the DRH and when temperature non-uniformities are of the order of 1 K, the 10-nm particles have a 32% probability of being exposed to ≥ 0.4% higher or lower RH compared to what they would be exposed to if they followed the deterministic trajectory. This RH variance can result in a significant apparent change of the particle size because a good fraction of their population can deliquesce into droplets. In a similar manner, 50-nm particles exhibit a diffusional displacements of only more than 0.03 mm, which for the same conditions (i.e., mismatched RHs and 1 K difference between the inner and outer electrode) leads to a 32% probability of being exposed to ≥ 0.1% higher or lower RH compared to what they would have been exposed if they were to follow their deterministic trajectory. As a result, the apparent non-prompt phase transition is significantly less evident compared to that of the 10-nm particles.

Maintaining a uniform humidity profile within the DMA is the key to avoiding phase transitions of particles within the DMA-2 and thus to potential erroneous interpretation of apparent non-prompt deliquescence. Ensuring that the RH conditions between the sheath and the sampled aerosol flow are matched and that the system has reached a thermal stability before starting the measurements is therefore essential for avoiding any experimental artifacts. In addition, one needs to ensure that any local RH

gradients within the classification column that are caused by external disturbances, are minimal. Probing these RH gradients within the classification zone of DMA-2 is impossible without disturbing the flows. Duplissy et al. (2009) have suggested that the temperature is measured simultaneously at the sheath flow inlet and excess flow outlet, and that it should be maintained within less that 0.1 K. However, even doing so may not exclude temperature non-uniformities within the classification section as demonstrated by heat transfer calculations (cf. Figs. S4.4 and S4.5 and associated discussion in sect. S4.3 of the supplement).

Given that most RH/T sensors have an accuracy of ± 2% in RH and 0.3 K in temperature and that the sheath flow is the dominant flow affecting the RH inside DMA-2, using a higher sheath-to-aerosol flow rate ratio would be advisable in order to smooth out potential RH non-uniformities. Alternatively, assuming that temperature variances are negligible, using deliberately $RH_{sh} < RH_a$ can avoid observations of apparent non-prompt phase transitions due to the experimental conditions. Particle deliquescence in this case definitely takes place before entering the DMA-2. The droplets can slightly shrink due to evaporation without changing particle phase (i.e., hysteresis in phase transitions) within DMA-2. Attention, however, should be paid to which RH to use (i.e., RH_a or RH_{sh}) when interpreting the results.

Figure 4.4 shows simulated results for $RH_{sh} = RH_a - 2\%$ for 10-nm $(NH_4)_2SO_4$ particles, together with the associated theoretical hygroscopicity curve (also shown in Fig. 4.3a). Evidently, RH_a (blue circles) should be used only for determining the DRH of the particles, while RH_{sh} (red squares) should be used for expressing their hygroscopicities for the entire RH range apart from the small region of $DRH - 2\% \leq RH_{sh} < DRH$. For instance, at $RH_{sh} = 77\%$ and $RH_a = 79\%$ the 10-nm $(NH_4)_2SO_4$ particles have a g value of 1.05 before entering DMA-2. When the particles enter the classification section of DMA-2, they are exposed to RH close to 77% for most of the time on their trajectory, thus shrinking and exhibiting a hygroscopic growth factor of ca. 1.03, which is less than 1% lower compared to the theoretical g for RH = 77%. At $RH_a = 80\%$ (i.e., > DRH) the 10-nm particles deliquesce and grow by 32% (i.e., g = 1.32) before entering DMA-2, but the measured growth factor is 1.29 due to shrinking at $RH_{sh} = 78\%$ within DMA-2. The range $78\% \leq RH_{sh} < DRH$ (grey area in Fig. 4.4),

should be avoided for determining *g* in deliquescence-mode experiments under these specific conditions, since the particles become droplets only because they have been exposed at RH_a > DRH upstream DMA-2 (i.e., the values of RH_{sh} do not justify phase transition). For RH_{sh} higher than the DRH, the RH_{sh} can be again used for expressing particle hygroscopicity, within less than 1% accuracy.

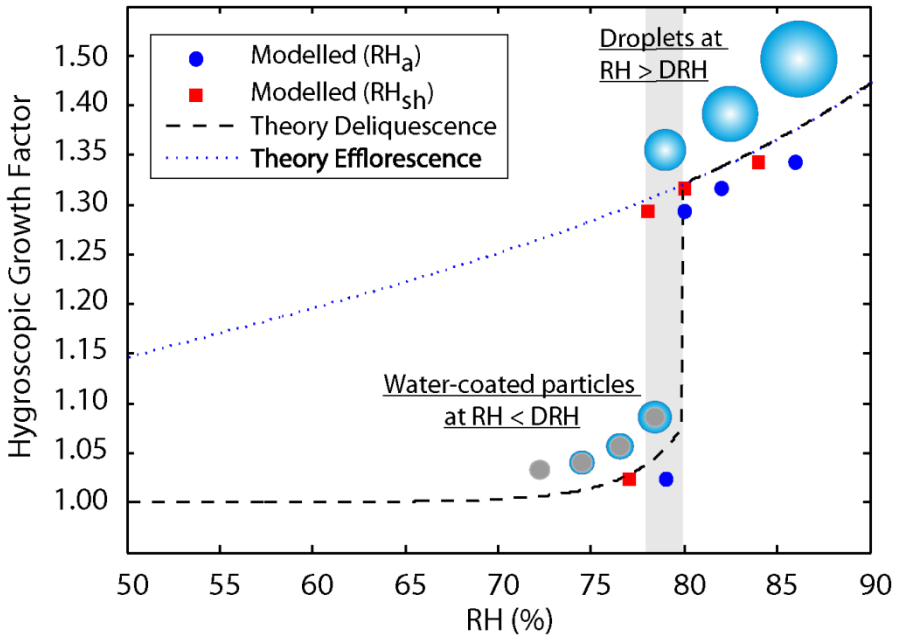

Fig. 4.4: Calculated mobility-diameter hygroscopic growth factors of 10-nm ammonium sulfate particles in comparison with their theoretical deliquescence and efflorescence curves (i.e., FHH isotherm and Köhler theory) when RH_{sh} = RH_a - 2%. Prediction are expressed in terms of RH_a (blue circles) and RH_{sh} (red squares).

4.5. Conclusions

The apparent non-prompt deliquescence of inorganic aerosol nanoparticles in HTDMA measurements, where the RH of the aerosol (RH_a) is lower than that of the sheath flow (RH_{sh}) in the second DMA, can be attributed to RH non-uniformities within the second DMA of the system (i.e., DMA-2). This interpretation has been demonstrated experimentally in the past (Biskos et al. 2006b), and corroborated with numerical predictions in this work. The simulations under the operating condition of DMA-2 where RH_{sh} = RH_a + 3% reproduce the experimental observations within 5% difference. To further improve the agreement between the simulated and observed particle hygroscopicities (i.e,. within 2% difference), we also assumed temperature non-uniformities inside DMA-2. Such temperature non-uniformities may occur accidentally even in well insulated systems.

The model findings provide additional evidence that the phase transition of inorganic nanoparticles is prompt and highlight the importance of keeping uniform RH conditions to the degree that this is technically possible for accurately determining the DRH and the associated particle hygroscopic growth factors. Considering that the uncertainty of typical RH/T sensors is in the order of 2% in RH and 0.3 K in temperature, however, small differences between RH_a and RH_{sh} and thermal instabilities inside the DMA are unavoidable. To avoid any erroneous result arising from these uncertainties, the recommendation is to use a higher sheath flow rate together with active temperature control of the DMA columns, as well as allowing for adequate time to ensure stable conditions. Alternatively, an RH_{sh} that is slightly smaller than RH_a can be used in a thermally uniform and stable DMA-2. In this case the observed particle deliquescence is prompt, ensuring a minor (up to 1%) difference from the real hygroscopic growth with respect to RH_{sh}, except for a narrow RH range below the DRH of particles, equal to the RH difference between the aerosol and sheath streams.

References

Anastasio, C., Martin, S. T., (2001). Atmospheric nanoparticles, Nanoparticles and the Environment, 44, 293-349

Biskos, G., Russel, L. M., Buseck, P. R., Martin, S. T., (2006a). Nanosize effect on the hygroscopic growth factor of aerosol particles, Geophysical Research Letters, 33, L07801.

Biskos, G., Paulsen, D., Russell, L. M., Buseck, P. R., and Martin, S. T., (2006b). Prompt deliquescence and efflorescence of aerosol nanoparticles, *Atmospheric Chemistry and Physics*., *6*, 4633–4642.

Chen, Y.-Y., & Lee, W.-M. G. (1999). Hygroscopic properties of inorganic-salt aerosol with surface-active organic compounds. *Chemosphere*, 2431–2448.

COMSOL. (2014). COMSOL Multiphysics Finite Element Analysis Software - Products. Retrieved from COMSOL Multiphysics Finite Element Analysis Software - Official site: http://www.comsol.com/

Djikaev, Y. S., Bowles, R., Reiss, H., Hameri, K., Laaksonen, A., and Vakeva, M. (2001). Theory of size dependent deliquescence of nanoparticles: Relation to heterogeneous nucleation and comparison with experiments. *The Journal of Physical Chemistry B*, 105, 7708–7722.

Duplissy, J., Gysel, M., Sjogren, S., Meyer, N., Good. N., Kammerman, L., Michaud, V., Weigel, R., Martins dos Santos, S., Gruening, C., Villani, P., Laj, P., Sellegri, K., Metzger, A., McFiggans, G. B., Wehrle, G., Richter, R., Dommen, J., Ristovski, Z., Baltensperger, U., and Weingartner, E. (2009). Intercomparison study of six HTDMAs: results and recomendations. *Atmospheric Measurement Technology*, 2, 363-378.

Flagan, R. C., (2001). Electrical Techniques. In , P. A. Baron & K. Willeke (Eds.), *Aerosol Measurement. Principles, Techniques and Applications* (2nd ed., pp. 553). New York: John Willey & Sons, Inc.

Hämeri, K., Väkevä, M., Hanson, H.-C., and Laaksonen, A. (2000): Hygroscopic growth of ultrafine ammonium sulphate aerosol measured using an ultrafine tandem differential mobility analyzer. *Journal of Geophysical Research*, 105, 22 231–22 242.

Hagwood, C. (1999). The DMA Transfer Function with Brownian Motion a Trajectory/Monte-Carlo Approach. *Aerosol Science and Technology*, 40-61.

Haywood, J. and Boucher, O. (2000). Estimates of the direct and indirect radiative forcing due to tropospheric aerosols: a review. *Review of Geophysics*, 38, 513–543.

Hennig, T., Massling, A., Brechtel, F. J., Wiedensohler, A., (2005). A Tandem DMA for highly temperature-stabilized hygroscopic particle growth measurements between 90% and 98% relative humidity. *Journal of Aerosol Science*, 36, 1210-1223

Hinds, W. C., (1999). *Aerosol Technology: Properties, Behavior, and Measurement of Airborne Particles.* (2nd ed.). New York: John Willey & Sons, Inc., (Chapter 15)

Hu, D., Qiao, L., Chen, J., Ye, X., Yang, X., Cheng, T., Fang, W., (2010). Hygroscopicity of Inorganic Aerosols: Size and Relative Humidity Effects on the Growth Factor. *Aerosol and Air Quality Research*, 10, 255-264.

Knutson, E. O. and Whitby, K. T. (1975). Aerosol classification by electric mobility: apparatus, theory, and applications. *Journal of Aerosol Science*, 6, 443–451.

Martin, S. T., (2000). Phase transitions of aqueous atmospheric particles. *Chemical Reviews*, 2000, 100(9), 3403-3454.

McMurry, P. H. (2000). A review of atmospheric aerosol measurements. *Atmospheric Environment* 34, 1959-1999.

Mirabel, P., Reiss, H., and Bowles, R. K.(2000): A theory for the deliquescence of small particles. *The Journal of Chemical Physics*, 113, 8200–8205.

Ogren, J. and Charlson, J. (1992). Implications for models and measurements of chemical inhomogeneities among cloud droplets, *Tellus B*, 44, 489–504.

Park, K., Kim, J. S., Miller, A. L., (2009). A study on effects of size and structure on hygroscopicity of nanoparticles using a tandem differential mobility analyzer and TEM. *Journal of Nanoparticle Research*, 11, 175-183.

Peng, C. G. and Chan, C. K. (2001). The water cycles of water-soluble organic salts of atmospheric importance. *Atmospheric Environment* 35, 1183–1192.

Rader, D. J. and McMurry, P. H. (1986). Application of the Tandem Differential Mobility Analyzer to Studies of Droplet Growth or Evapouration. *Journal of Aerosol Science* 17, 771–787.

Russell, L. M. and Ming, Y. (2002). Deliquescence of small particles. *The Journal of Chemical Physics,* 116, 311–321.

Stöckelmann E. and Hentschke R. (1999). A molecular-dynamics simulation study of water on NaCl(100) using a polarizable water model. *Journal of Chemical Physics*, 110 N24, 12097-12107.

Stolzenburg, M. R. and McMurry, P. H.(1991). An ultrafine aerosol Condensation Nucleus Counter. *Aerosol Science and. Technology*, 14, 48–65.

Tang I. N., Munkelwitz, H. R., Davis J. G. (1977). Aerosol Growth Studies - II. Preparation and growth measurements of monodisperse salt aerosols. *Journal of Aerosol Science*, 8, 149-159.

Tang I. N., Munkelwitz, H. R., Davis J. G. (1978). Aerosol Growth Studies - IV. Phase transformation of mixed salt aerosols in a moist atmosphere. *Journal of Aerosol Science*, 9, 505-511.

Tang I. N., Munkelwitz, H. R. (1993). Composition and temperature dependence of the deliquescence properties of hygroscopic aerosols. *Atmospheric Environment 27A*, 4, 467-473.

Tang, I. N., Tridico, A. C., and Fung, K. H. (1997). Thermodynamic and optical properties of sea salt aerosols. *Journal of Geophysical Research*, 102, 23 269–23 275.

Topping, D. O., McFiggans, G. B., and Coe, H. (2005): A curved multi-component aerosol hygroscopicity model framework: Part 1 – Inorganic compounds. Atmospheric Chemistry and Physics, 5, 1205–1222.

Wang, Z., King, S. M., Freney, E., Rosenoern, T., Smith, M. L., Chen, Q., Kuwata, M., Lewis, E. R., Pöschl, U., Wang, W., Buseck, P. R., Martin, S. T., (2010). The Dynamic Shape Factor of Sodium Chloride Nanoparticles as Regulated by Drying Rate. *Aerosol Science and Technology*, 44:11, 939-953.

Supplement

Relative Humidity Non-Uniformities in HTDMA Measurements

S. Bezantakos, L. Huang, K. Barmpounis, S. T. Martin and G. Biskos

S4.1. Supporting Equations for the Classification Module

The diffusion coefficient of the particles suspended in a gas is given by (Hinds 1999):

$$D_{\mathrm{p}} = \frac{kTCc}{3\pi\eta d_p},$$

(S4.1)

where k is the Boltzmann constant (1.38×10^{-23} J/K), T is the absolute temperature, η is the air viscosity (1.81×10^{-5} kg/ms), d_{p} is the particle diameter and C_c is the Cunningham slip correction factor given by:

$$Cc = 1 + \frac{\lambda}{d_p} \times \left(2.34 + 1.05 \times exp\left(-0.39 \times \frac{d_p}{\lambda}\right)\right).$$

(S4.2)

Here λ is the air mean free path (66×10^{-9} m at atmospheric pressure).

S4.2. Finite Element Model for Predicting the Flow Velocity, the RH and the Temperature Fields within the DMA

A 2D axisymetric numerical model created in COMSOL Multiphysics® was employed to simulate the profiles of the flow, temperature (T) and Relative Humidity (RH) within DMA-2. A simplified design of the nano-DMA (TSI Model 3085) was used in this model, which incorporated all its main features and dimensions (cf. Fig. S4.1, herein and Table 4.1 in the manuscript). The *Non-Isothermal Flow* module of COMSOL Multiphysics® was used to calculate the laminar flow and temperature profiles inside the DMA. More specifically, heat is transferred between the inner electrode and the top/bottom DMA structure (joints and support points) by conduction (thermal contact) and between the inner electrode and the air which flows around it by convection/conduction. The bottom part of the inner electrode is connected to the DMA base by a plastic electrical insulator, while a relatively small surface is in contact with the rest of the column at the top part, limiting the conductive heat transfer at these points. The equation describing the heat transfer by conduction and/or convection has the form of:

$$\rho C_{\mathrm{p}} u \nabla T = \nabla(k \nabla T) + Q, \quad \text{(S4.3)}$$

where ρ and C_{p} are respectively the density and the heat capacity of the materials, which in our model are stainless steel and air, Q is the total heat source, T is the absolute temperature and u the laminar flow velocity vector, which in relation to the temperature is given by:

$$\rho(\mathrm{u}\nabla)\mathrm{u} = \nabla\left[-p\mathrm{I} + \mu(\nabla u + (\nabla u)^T) - \frac{2}{3}\mu(\nabla u)\mathrm{I}\right] + \mathrm{F}. \quad \text{(S4.4)}$$

Here μ is the dynamic viscosity of air, p the absolute pressure and F the body force vector. Viscous heating and pressure work are omitted because they are negligible for laminar flows inside DMAs. Heat transfer by radiation was also insignificant for the temperature range of our simulations (i.e., from 290 to 294 K) and therefore omitted.

The *Transport of Diluted Species* module of COMSOL Multiphysics® was employed to calculate the water vapor concentration using the mass balance equation, which can be expressed as:

$$\nabla(-D_{\mathrm{w}} \nabla c_{\mathrm{w}}) + u \nabla c_{\mathrm{w}} = 0. \quad \text{(S4.5)}$$

Here u represents the laminar flow velocity vector within the DMA (cf. Fig. S4.2), D_{w} is the diffusion coefficient of water vapor in air, which for the operating conditions used in the experiments is 2.47×10^{-5} m^2 s^{-1} (Merlivat 1978), and c_{w} is the water vapor concentration which can be determined as follows:

$$c_{\mathrm{w}} = \frac{p_{\mathrm{w}}}{RT}. \quad \text{(S4.6)}$$

Here $p_{\mathrm{w}} = \frac{\mathrm{RH}(T)}{100}\, p_{\mathrm{sat}}(T)$ is the partial pressure of water vapor with $p_{\mathrm{sat}}(T)$ being the saturated vapor pressure at temperature T, and R the ideal gas constant. Given that the pressure along the classification column does not vary significantly from 1 atm in typical HTDMA systems, $p_{\mathrm{sat}}(T)$ can be calculated using the polynomial fit available in the literature (Lowe and Ficke 1974; Eq. 6.1 and constants provided therein). The profiles of the laminar flow velocities and RH were exported and used in the particle trajectory model described in the manuscript.

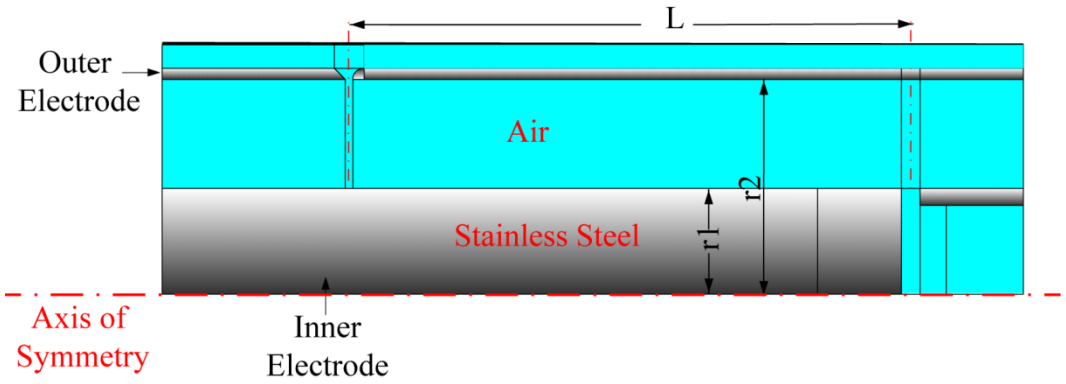

Fig. S4.1: Simplified geometry resembling the TSI nano-DMA and the materials used for the numerical simulations of the flow, temperature and RH fields.

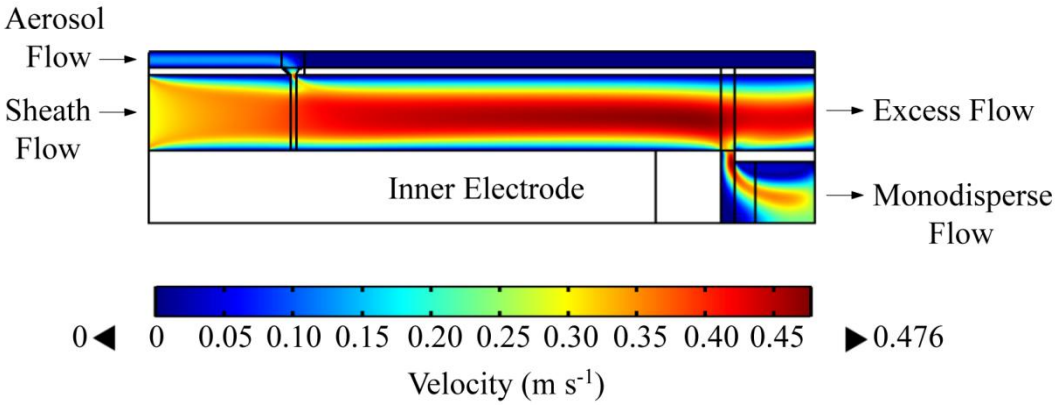

Fig. S4.2: Simulated velocity profiles inside DMA-2 when the sheath and aerosol flow are 15 and 1.5 lpm, respectively.

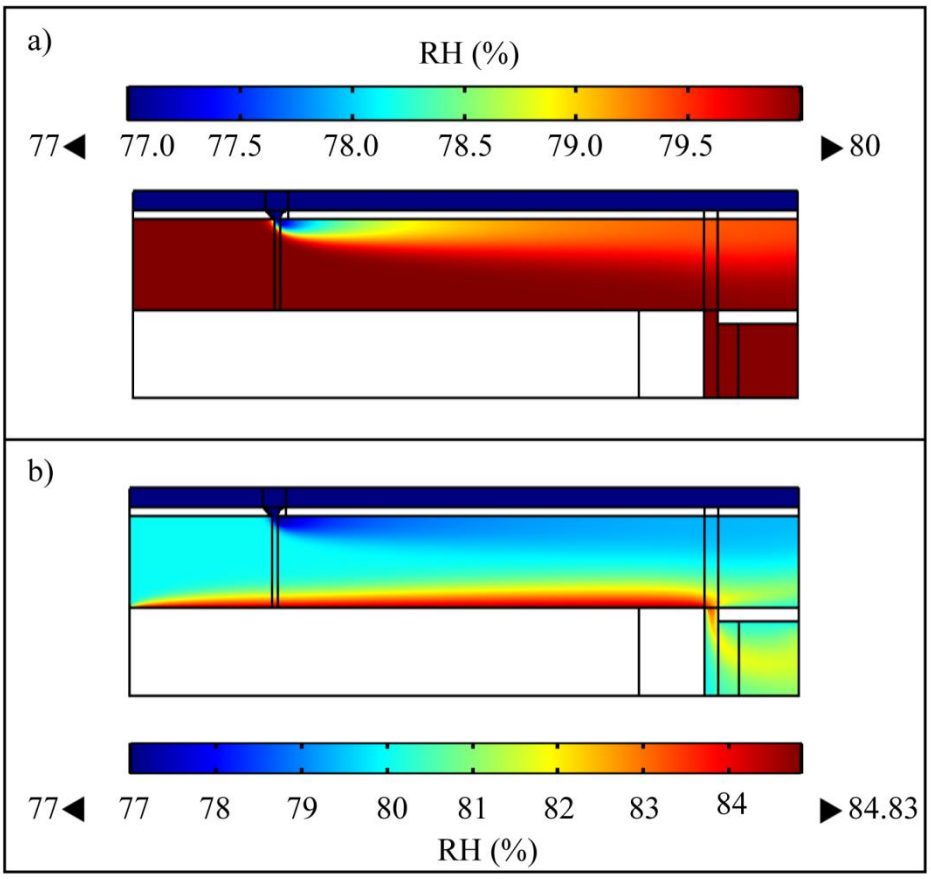

Fig. S4.3: RH profiles when RH_{sh} = 80% and RH_a = 77% under uniform temperature conditions **(a)** and when a temperature difference of 1 K is assumed between the inner electrode and the rest of the DMA parts (**b**).

S4.3. Simulations for Predicting the Time Required for Temperature to Equilibrate

The model described above was used in a time dependent simulation to provide more information on the evolution of temperature inside DMA-2, when the outside electrode temperature is increased by 4 K (i.e., from 290 to 294 K), assuming that both the aerosol and sheath flows are at the same temperature (i.e. 294 K). Such conditions would occur in practice during the initial stages of deliquescence-mode experiments or when the environmental temperature rapidly increases. The simulations show that there is a time delay of ca. 2800 sec (not shown) until the inner electrode equilibrates with the air stream temperature (i.e., 294 K). The time needed for the increase of the inner electrode temperature is caused by the different heat capacities of the air flowing in the DMA and the material (stainless steel) of the column. The heat transferred between the air stream and the inner electrode results in

a noticeable temperature gradient inside DMA-2, in the vicinity of the inner electrode and especially near the monodisperse outlet. The temperature non-uniformities of the air stream decay with time and after approximately 1800 sec reaches a minimum point of less than 0.1 K (cf. Fig. S4.4).

Figure S4.5 shows the temporal evolution of the average temperature at the excess flow outlet for the above simulated conditions, which would correspond to the readings of a temperature sensor downstream the DMA (something that is commonly used in HTDMA systems). The average excess flow outlet temperature fails to capture the actual extend of the localized temperature non-uniformities shown in Fig. S4.4. These discrepancies are more pronounced in the initial stages of the transitional phenomenon, but tend to minimize as the system approaches thermal equilibrium. As a result probing the temperature and RH downstream is not advisable for expressing the actual conditions inside the DMA and should be used with caution for verifying the thermal stability of the system.

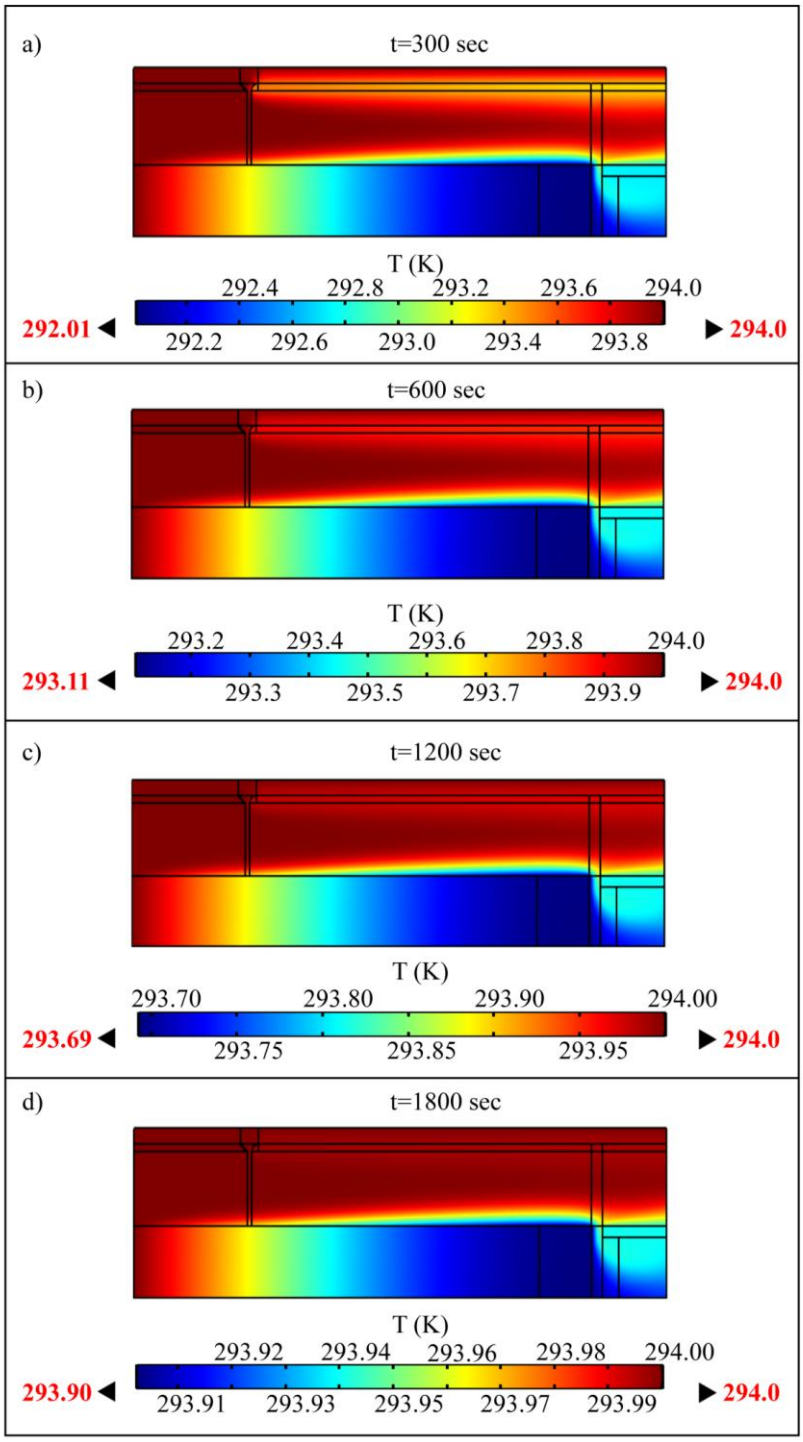

Fig. S4.4: Evolution of the temperature profile inside the DMA when initially (t = 0 s) the outside electrode temperature is 4 K higher than that of the inner electrode (i.e., from T_{in} = 290 K and T_{out} = 294 K), assuming that both the aerosol and sheath flow have the same temperature (i.e. 294 K). Note that the range of the colorbar is changing (bold red numbers) with time.

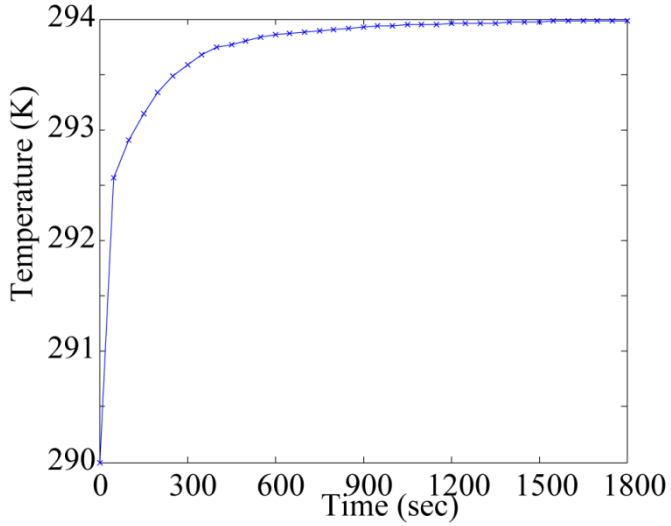

Fig. S4.5: Evolution of the average temperature at the excess flow outlet of the DMA, when the outside electrode temperature is increased by 4 K (i.e. from 290 to 294 K) at t = 0 sec, assuming that both the aerosol and sheath flow have the same temperature (i.e. 294 K).

References

COMSOL® multiphysics version 4.3b. *Reference manual*. Stockholm, Sweden: COMSOL AB

Hinds, W. C., (1999). Aerosol Technology: Properties, Behavior, and Measurement of Airborne Particles. (2nd ed.). New York: John Willey & Sons, Inc., (Chapter 7)

Lowe, P. R. and Ficke, J. M., (1974): The Computation of Saturation Vapor Pressure, *Environmental Prediction Research Facility, Naval Postgraduate School*, Monterey, California 93940, Technical Paper No. 4-74.

Merlivat, L., (1978): Molecular diffusivities of $H_2{}^{16}O$, $HD^{16}O$, and $H_2{}^{18}O$ in gases, *Journal of Chemistry and Physics*, 69, 2864

5. Modification of the TSI 3081 Differential Mobility Analyzer to include three Monodisperse Outlets : Comparison between experimental and theoretical performance

S. Bezantakos[1,2], M. Giamarelou[1], L. Huang[3], K. Barmpounis[2], J. Olfert[4] and G. Biskos[2,3,5*]

[1]*Department of Environment, University of the Aegean, Mytilene 81100, Greece*

[2]*Energy Environment and Water Research Center, The Cyprus Institute, Nicosia 1645, Cyprus*

[3]*Faculty of Applied Sciences, Delft University of Technology, Delft 2628-BL, The Netherlands*

[4]*Department of Mechanical Engineering, University of Alberta, Edmonton T6G 2R3, Canada.*

[5]*Faculty of Civil Engineering and Geosciences, Delft University of Technology, Delft 2628-CN, The Netherlands*

Email: g.biskos@tudelft.nl;

Submitted: April 2016

Aerosol Science and Technology

*To whom correspondence should be addressed

Abstract

Differential Mobility Analyzers (DMAs) are widely used for determining the size of aerosol particles or for probing their size-dependent physicochemical properties when two are employed in tandem (i.e., TDMAs). A limitation of TDMAs is their long measuring cycle when the properties of more than one monodisperse populations need to be probed. In this work we propose a simplified modification of a classical cylindrical DMA with three monodisperse outlets in its central electrode (3MO-DMA), with the objective of using it as first DMA in TDMA systems for reducing their measuring cycle. The performance of the 3MO-DMA at different flow conditions was evaluated in laboratory conditions, and compared with theoretical predictions using the generic DMA transfer function provided by Giamarelou et al. (2012). The theory predicted accurately (i.e., within 3%) the geometric mean diameters of the three distinct populations, as well as the resolutions of the first and the third outlet, under all experimental conditions. Despite that the geometric standard deviation of the monodisperse aerosol from outlet #2 corresponded to a monodisperse aerosol (σ_g of up to 1.08 at 8.0 lpm sheath and 1.5 lpm aerosol flow), the resolution of this outlet was 10 to 74% lower than that predicted theoretically depending on the sheath-to-aerosol flow ratio. Despite the lower resolution of the 2nd monodisperse particle outlet compared to the rest, the 3MO-DMA designed and tested in this work can be used as a first DMA in TDMA systems. Doing so provides simultaneously three distinct monodisperse particle populations with accurately defined geometrical median diameters, thereby reducing the measuring cycle of the entire system when used to probe the size-dependent properties of particles of different size.

5.1. Introduction

Particle size is a key parameter for understanding the processes through which atmospheric aerosols can affect human health and climate (Hinds, 1999). This is because it affects the ability of aerosols to scatter and absorb incoming solar radiation, which in turn defines the visibility and radiative properties of the atmosphere (Haywood and Boucher, 2000). In addition the size of atmospheric particles affects their ability to act as cloud condensation nuclei, thus changing the cloud properties and indirectly affecting climate at a regional and global scale (Ogren and Charlson, 1992). The size of atmospheric aerosol particles changes during their lifetime in the atmosphere by processes of condensation, evaporation, and coagulation (Seinfeld and Pandis, 2006). As a result, measuring the variability in the size of atmospheric particles is important for understanding their climate impacts (McMurry, 2000).

Early methods for sizing aerosol particles were based on size-dependent properties such as their diffusivity (for small particles) and inertia (for bigger particles). For instance, diffusion batteries were used for classifying small particles (e.g., Gormley and Kennedy, 1949), while impactors (e.g., Marple 1970) and cyclones (e.g., Leith and Mehta, 1973) for sizing large segregated particles. While simple and easy to construct, deploy, and maintain, these instruments have limited resolution and measuring size range. Knutson and Whitby (1975) introduced the Differential Mobility Analyzer (DMA), which exploits the motion of charged particles in a flowing aerosol under an electric field, for determining their electrical mobility and from that their size. This approach provided a significant improvement in sizing resolution and extended the range of particle sizes that a single instrument could classify.

Despite being more complex in design and construction than diffusion batteries and inertia classifiers, DMAs are still the most effective tools for sizing aerosol particles. The most popular DMA design consists of two concentric cylinders between which a high potential difference is applied to establish a uniform electrostatic field. A particle free, sheath flow is introduced between the two cylindrical electrodes, while charged polydisperse aerosol particles are introduced at the inner circumference of the outer electrode. Depending on their electrical mobility, particles follow different trajectories and land at different positions along the inner electrode. Particles having electrical mobilities

within a very narrow range exit the classifier through a monodisperse outlet slit located at a distance *L* downstream the polydisperse aerosol inlet.

For a specific DMA design, the range of particle mobilities in the monodisperse flow depends on the operating conditions (i.e., flow rates and applied voltage between the two cylindrical electrodes). The probability of particles of different electrical mobility to exit the DMA under specific operating conditions is described by its transfer function. For large particles the transfer function can be derived from their deterministic trajectories inside the classification zone of the DMA (Knutson and Whitby, 1975), while for smaller particles the effects of the Brownian motion has to be taken into account (Stolzenburg, 1988).

DMAs are employed in systems that measure the size distribution of particles by either step-increasing (Differential Mobility Particle Sizer; DMPS; Keady et al., 1983) or continuously scanning the potential between the two electrodes (Scanning Mobility Particle Sizer; SMPS; Wang and Flagan, 1990). In addition they are used in tandem (i.e., tandem DMA systems; Rader and McMurry, 1986) for probing particle size-dependent properties such as hygroscopicity (e.g., Bezantakos et al., 2013) volatility (e.g., Giamarelou et al., 2016) and charge probability (e.g., Biskos et al., 2005). Several DMA designs have been proposed for covering the needs and applications of the variety of systems they are used into. The classical, cylindrical, long DMA (TSI Model 3081), which was based on the design of Knutson and Whitby (1975), is employed for classifying particles having diameters from ca. 7 nm and up to ca. 1 μm depending on the operating flow rates (typically from 3 to 15 lpm sheath flow rate). For smaller particles the operation of the classical DMA is limited by the high diffusivity of the particles, which on the one hand increases their losses to the walls of the tubing at the inlet and outlet of the DMA and on the other deviates the particles significantly from their deterministic trajectories in the classification zone. To reduce the limitations of particle diffusivity in the sub-10-nm particles Chen et al. (1996) and Chen et al. (1998) introduced a cylindrical DMA which has a similar design with that proposed by Knutsen and Whitby (1975), but a significantly shorter classification column (i.e., Nano-DMA). Doing so (and using typical sheath flow rates ranging from 3 to 15 lpm) improves the resolving power of the DMA for particles having sizes in the vicinity of 3-5 nm. The ability to classify particles residing in the sub-5-nm range with high resolution and

low particle losses has also been considered. In this direction, de Juan and de la Mora (1998) proposed the high-flow DMAs to classify aerosols particles having sizes in the nanometer and sub-nanometer range. Recent advances in the high-flow DMAs have also allowed measurements of nanoparticles and atomic clusters with high accuracy and resolution (Attoui et al., 2013). In addition, a parallel plate DMA (IONER X1) was designed by Santos et al. (2009) for measuring the electrical mobility spectra of ions with increased resolution or for producing monomobile ions. Other designs, like for example radial DMAs (Zhang et al., 2007) have the advantage of being more compact than their cylindrical counterparts. Along these lines Barmpounis et al. (2016) proposed new manufacturing methods (using mold casting or 3D printing) for building DMAs out of polyurethane (namely the PU-DMAs) or other polymers, resulting in a significant weight loss without sacrificing the classification capabilities when compared to classical DMAs.

With the objective to reduce the time needed for scanning over different operating conditions to determine the size distributions of the particles with SMPS or DMPS systems, Chen et al., (2007) designed and characterized a DMA with three monodisperse particle outlets located along the outer cylinder. Results from this study were used to validate the generalized theoretical transfer function for DMAs with multiple monodisperse outlets (i.e., MMO-DMA; Giamarelou et al., 2013). Apart using it as a classifier in a DMPS or an SMPS system, an MMO-DMA can also be used as a first DMA in TDMA systems. The advantage of that is that it can allow simultaneous measurements of the properties of 3 monodisperse particle populations from the sampled polydipserse aerosol, thereby reducing significantly the measuring cycle of the system. Using the 3MO-DMA design proposed by Chen et al. (2007) (i.e., with the monodisperse outlet slits along the outer electrode) as the first DMA in TDMA configurations, however, would require the use of three single outlet DMAs and an equal number of condensation particle counters (CPCs; Agarwal and Sem, 1980) downstream each monodisperse particle outlet, leading to an expensive and bulky system.

Here we describe a simple 3MO-DMA by including three monodisperse outlets along the central electrode of a classical cylindrical DMA (namely a TSI Model 3081 DMA). The resulting DMA yields a single monodisperse aerosol flow including three distinct populations of monodisperse aerosol particles, making it ideal for use as a first DMA in TDMA systems. The performance of the 3MO-DMA is tested under different

operating conditions (i.e., flows and voltages) and compared with predictions from the model provided by Giamarelou et al. (2012).

5.2. Experimental

5.2.1 Design of the 3MO-DMA

The 3MO-DMA described here was designed with the objective to use it as the first DMA (DMA-1) in a TDMA system. The classifier is a modified TSI Model 3081 DMA in which we replaced the inner electrode with one that includes three monodisperse outlet slits. As a result, all three monodisperse particle populations are included in one flow (i.e., the monodisperse outlet flow of the 3081 DMA). The position of each monodisperese slit (i.e., on the inner electrode) was defined so that particles having electrical mobility diameters more than twice larger compared to those classified by the outlet immediately upstream are selected by the intermediate and the last outlet along the column at a nominal pressure of 1 atm. and temperature of 25 ºC. The mobility diameter ratio between the consequent outlets of the 3MO-DMA (i.e., the midpoint mobility diameter of the particles classified by each outlet divided with that of the upstream outlet) ranges from 2.1 to 3.3, depending on the operating flow rates and voltage. For example, when the 3MO-DMA is operated with sheath and aerosol flows of 3.0 and 0.3 lpm, respectively, the midpoint mobility diameters of the classified particles will be 34.72, 99.77 and 247.68 nm, when the inner electrode voltage is 2 kV. This feature is necessary for distinguishing particle populations of different hygroscopic properties as their size distributions measured by the second DMA (i.e., DMA-2, operated at a scanning or stepping mode), will not overlap even if their hygroscopic growth factors are up to 2 when exposed to relative humidity (RH) conditions typically used in HTDMA systems (in the vicinity of 90%).

Figure 5.1 provides a schematic layout of the 3MO-DMA including the details of the inner electrode and the resulting particle size distributions upstream the inlet and downstream each of the 3 monodisperse particle outlets.

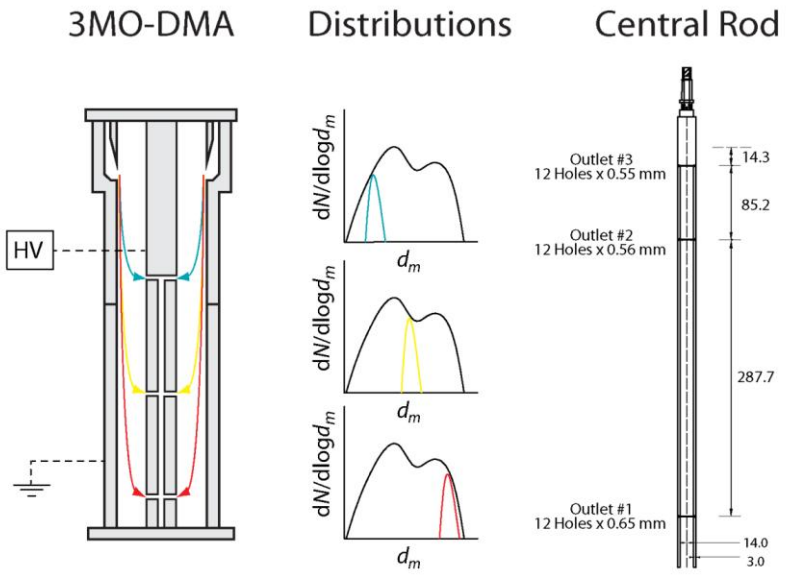

Fig. 5.1. Schematic diagram of the 3MO-DMA, operating principle and details of the design.

The top part of the inner electrode, which includes the sheath flow inlet, the threads for connecting the inner electrode to the main body of the DMA and the connection to the high voltage cable, was the same as that of the TSI Model 3081 long DMA. The inner electrode was designed as a cylindrical tube having wall thickness of 3 mm and an outer radius of 10 mm (instead of 9.37 mm of the original TSI design). The three monodisperse outlet slits were located at 14.3, 95.0 and 397.0 mm downstream the polydisperse aerosol inlet. These distances were determined by (Giamarelou et al., 2012):

$$L_i = \frac{\left(Q_{\mathrm{sh}_i}+Q_{\mathrm{m}_i}\right)\ln\left(\frac{\mathrm{R}_1}{\mathrm{R}_2}\right)}{4\pi V Z^*_{\mathrm{p}_i}}, \tag{5.1}$$

where R_1 and R_2 are respectively the inner and outer radii of the 3MO-DMA, V is the voltage of the inner electrode, whereas Q_{sh_i} is the sheath flow and Q_{m_i} the excess flow of each monodisperse outlet i given by:

$$Q_{\mathrm{sh_i}} = \begin{cases} Q_{\mathrm{sh}} \text{ for } i = n \\ Q_{\mathrm{m}_{i+1}} \text{ for } 1 \le i \le n-1 \end{cases}, \tag{5.2}$$

and

$$Q_{\mathrm{m_i}} = \begin{cases} Q_{\mathrm{sh}} + Q_{\mathrm{a}} - Q_{\mathrm{s}_i} \text{ for } i = n \\ Q_{\mathrm{m}_{i+1}} - Q_{\mathrm{s}_i} \text{ for } 1 \le i \le n-1 \end{cases}. \tag{5.3}$$

Here n is the total number of monodisperse particle outlets. Following the notation of Giamarelou et al. (2012), the numbering of the outlet starts from the one furthest from the polydisperse aerosol inlet (i.e., outlet #1 is the furthest while outlet #3 is the closest to the inlet). In the equations above, Q_{sh} and Q_{a} are respectively the initial sheath and aerosol flows (i.e., before entering the 3MO-DMA), while $Q_{\mathrm{s_i}}$ is the sample flow through each monodisperse outlet i. For reasons of simplicity, in order to determine the positions of each monodisperse particle outlet we assumed that $Q_{si} = 1/3Q_{\mathrm{a}}$. In Eq. 5.1 $Z^*_{\mathrm{p}_i}$ is the midpoint electrical mobility of the particles classified at each monodisperse particle outlet at a given set of operating conditions (i.e., flows and voltage) which is associated to the midpoint mobility diameter $d^*_{\mathrm{p}_i}$ of the particles through (Hinds, 1999):

$$Z^*_{\mathrm{p}_i} = \frac{n_{\mathrm{e}} e C_c}{3\pi\eta d^*_{\mathrm{p}_i}}. \quad (5.4)$$

Here, n_{e} and e are respectively the number of elementary charges and the electron charge, whereas η is the air viscosity and C_c the Cunningham sleep correction factor (cf. sect. S5.1 in the supplement for details). Each outlet slit was designed with 12 holes, the diameter of which were 0.54 for outlet #3, 0.55 mm for outlet #2, and 0.65 mm for outlet #1 (cf. Fig 5.1). Doing so allowed for a reduced sample flow through the outlet closest to the aerosol inlet (i.e., outlet #3) in an attempt to reduce flow disturbances caused by this outlet, due to its proximity (i.e., 14.3 mm) to the aerosol inlet. Using these dimensions, sample flow rates of approx. 26, 33 and 41% of the total aerosol flow were estimated for outlets #3, #2, and #1, respectively.

5.2.2 Characterization of the 3MO-DMA

5.2.2.1 Experimental setup

A tandem DMA system (cf. Fig. 5.2) was employed to determine the performance of the 3MO-DMA. In brief, polydisperse ammonium sulfate (AS) particles were produced by atomizing (using a TSI Model 3076 atomizer) a 0.1 w/v AS solution using N_2 (99% purity) as carrier gas. The polydisperse aerosol particles were dried to less than 10% RH using two silica gel diffusion driers in series, and charge neutralized by passing them through a ^{85}Kr aerosol neutralizer (TSI Model 3077). A custom-made single outlet DMA (cf. Table 5.1),

employing a recirculating sheath flow system (cf. Biskos et al., 2006 for details) and a built-in High Voltage (HV) power supply (Spellman Model V6A10N30), was used to provide a monodisperse aerosol flow. The mobility distributions of the monodisperse particles were then measured by the 3MO-DMA that was coupled with an ultrafine Condensation Particle Counter (uCPC; TSI Model 3025; Stolzenburg and McMurry, 1991). In all experiments, the HV of the central electrode of the 3MO-DMA was stepwise increased with each step having a duration of 50 s. The average particle number concentration at each voltage was obtained from the uCPC during the last 5 s of each step. The first 45 s were allowed for the concentration to stabilize from that corresponding to the previous voltage settings.

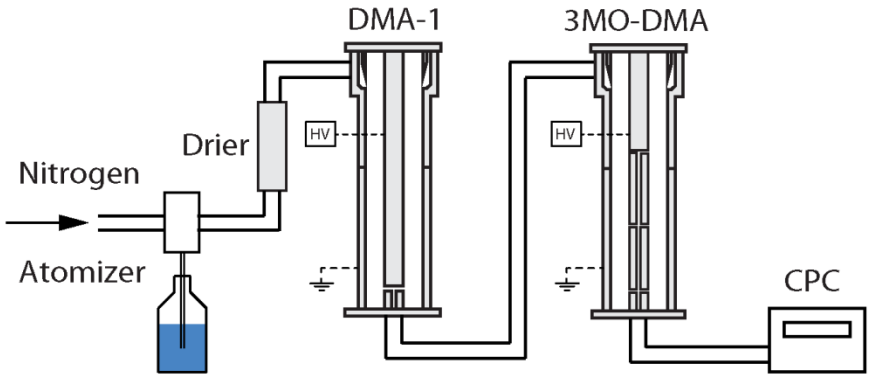

Fig. 5.2. Experimental tandem DMA setup for determining the resolution of the 3MO-DMA at various operating conditions.

The sheath and aerosol flows of both DMAs were measured before each experiment using a bubble flow meter (Sensidyne Gilibrator 2) in order to confirm that the flow controllers were operating within ± 1% of their setpoint values. Adequate drying (i.e., less than 10% RH) of the polydisperse aerosol upstream the neutralizer was verified using a Relative Humidity/Temperature sensor (Rotronic Model HC2-05). The operating voltages of both DMAs were frequently monitored for ensuring that the HV power supplies were operating within ± 1% accuracy.

Table 5.1: Dimensions of all the DMAs used in this work.

Type	Symbol	Description	Value	Unit
Custom single Outlet DMA	L_c	Effective length	374.00	mm
	R_c	Outer radius	19.58	mm
	r_c	Inner radius	9.35	mm
TSI 3081 Long DMA	L_T	Effective length	443.69	mm
	R_T	Outer radius	19.61	mm
	r_T	Inner radius	9.37	mm
Custom 3MO-DMA	L_1	Effective length outlet #1	14.30	mm
	L_2	Effective length outlet #2	95.00	mm
	L_3	Effective length outlet #3	397.00	mm
	R	Outer radius	19.61	mm
	r	Inner radius	10.00	mm

5.2.2.2 Data processing

The size distributions of the monodisperse particles measured by TDMA systems are predominantly defined by the size distribution of the sampled polydisperse aerosol, the transfer functions of the two DMAs employed and the detection efficiency of the particle detector. Assuming that the number concentration of the polydisperse aerosol upstream DMA-1, the detection efficiency of the CPC and the transport particle losses in the tubing of the entire TDMA are constant, the response of the system can be expressed as (Barmpounis et al., 2016):

$$\frac{N_2}{N_1} = \frac{\int_0^{+\infty} \Omega_1(Z_p, Z_{p_1}^*)\Omega_2(Z_p, Z_{p_2}^*)dz_p}{\int_0^{+\infty} \Omega_1(Z_p, Z_{p_1}^*)dz_p}. \quad (5.5)$$

Here, N_1 and N_2 are respectively the particle number concentrations upstream and downstream DMA-2, Ω_1 and Ω_2 are the transfer functions whereas $Z_{p_1}^*$ and $Z_{p_2}^*$ the central electrical mobility of particles classified by DMA-1 and DMA-2, respectively. The theoretical transfer function of the cylindrical, single outlet DMA (DMA-1 in this case) considering the diffusivity of the particles is given by (Stolzenburg, 1988):

$$\Omega_1(\tilde{Z}_{p1}) = \frac{\tilde{\sigma}_1}{\sqrt{2}\,\beta_1(1-\delta_1)}\left[\varepsilon\left(\frac{\tilde{Z}_{p1}-(1+\beta_1)}{2\sqrt{\tilde{\sigma}_1}}\right) + \varepsilon\left(\frac{\tilde{Z}_{p1}-(1-\beta_1)}{2\sqrt{\tilde{\sigma}_1}}\right) - \varepsilon\left(\frac{\tilde{Z}_{p1}-(1+\delta_1\beta_1)}{2\sqrt{\tilde{\sigma}_1}}\right) - \varepsilon\left(\frac{\tilde{Z}_{p1}-(1-\delta_1\beta_1)}{2\sqrt{\tilde{\sigma}_1}}\right)\right]. \quad (5.6)$$

Here $\tilde{Z}_{\mathrm{p1}}$ is the dimensionless particle electrical mobility, β_1 and δ_1 are the dimensionless flow parameters, and $\tilde{\sigma}_1$ is the dimensionless diffusional broadening parameter. Expressions of the above parameters and of function ε are provided in the supplement (cf. sect. S5.1). Eq. 5.6 can be extended to predict the transfer function of DMAs with multiple monodisperse particle outlets as follows (Giamarelou et al., 2012):

$$\Omega_{2i}\left(\tilde{Z}_{\mathrm{p}_{2i}}\right) = \frac{\tilde{\sigma}_{2i}}{\sqrt{2}\,\beta_{2i}(1-\delta_{2i})}\left[\varepsilon\left(\frac{\tilde{Z}_{\mathrm{p}2_i}-(1+\beta_{2i})}{2\sqrt{\tilde{\sigma}_{2i}}}\right)+\varepsilon\left(\frac{\tilde{Z}_{\mathrm{p}_{2i}}-(1-\beta_{2i})}{2\sqrt{\tilde{\sigma}_{2i}}}\right)-\varepsilon\left(\frac{\tilde{Z}_{\mathrm{p}_{2i}}-(1+\delta_{2i}\beta_{2i})}{2\sqrt{\tilde{\sigma}_{2i}}}\right)-\right.$$

$$\varepsilon\tilde{Z}\mathrm{p}\,2i-1-\delta 2i\beta 2i2\sigma 2i,$$

(5.7)

where i denotes the number of monodisperse outlets, which are numbered starting from the one furthest from the polydisperse aerosol inlet.

Adjustable broadening parameters can be introduced in Eq. 5.7 for treating disparities between the theoretical and measured transfer functions, resulting into (Giamarelou et al., 2013):

$$\Omega_{2,i}{}'\left(\tilde{Z}_{\mathrm{p}_{2i}}\right) = \frac{\tilde{\sigma}_{2i}{}'}{\sqrt{2}\,\beta_{2i}{}'(1-\delta_{2i}{}')}\left[\varepsilon\left(\frac{\tilde{Z}_{\mathrm{p}_{2i}}-(1+\beta_{2i}{}')}{2\sqrt{\tilde{\sigma}_{2i}{}'}}\right)+\varepsilon\left(\frac{\tilde{Z}_{\mathrm{p}_{2i}}-(1-\beta_{2i}{}')}{2\sqrt{\tilde{\sigma}_{2i}{}'}}\right)-\varepsilon\left(\frac{\tilde{Z}_{\mathrm{p}_{2i}}-(1+\delta_{2i}{}'\beta_{2i}{}')}{2\sqrt{\tilde{\sigma}_{2i}{}'}}\right)-\right.$$

$$\varepsilon\tilde{Z}\mathrm{p}\,2i-1-\delta 2i'\beta 2i'2\sigma 2i'.$$

(5.8)

The adjustable parameters $\beta_{2i}{}'$and $\delta_{2i}{}'$ represent corrections in the flow rates (cf. sect. S5.1 in the supplement), while $\tilde{\sigma}_{2i}{}'^2$ is the total adjusted spread parameter given by:

$$\tilde{\sigma}_{2i}{}'^2 = f_{G_i}G_i + \sigma^2_{\mathrm{mix}i}\,, \tag{5.9}$$

where $\sigma^2_{\mathrm{mix}i}$ accounts for additional broadening of the transfer function caused by non-ideal mixing of the flows inside the MMO-DMA, while f_{G_i} is a factor accounting for any errors in the estimation of the unique geometric- and flow-condition-dependent parameter G_i (cf. sect. S5.1 in the supplement). The $\sigma^2_{\mathrm{mix}i}$ parameter, together with the adjusted flow parameters $\beta_{2i}{}'$ and $\delta_{2i}{}'$ determines the resolution in the non-diffusing limit, $R'_{nd_i}(\beta_{2i}{}', \delta_{2i}{}', \sigma^2_{\mathrm{mix}i})$. Note that the theoretical (i.e., without using any broadening parameters) non-diffusing limit of the transfer function is given by:

$$R_{nd_i} = \frac{1}{\beta_i(1+|\delta_i|)}\,. \tag{5.10}$$

The discrepancy between the theoretical and the measured/adjusted resolution can be expressed as the ratio:

$$f_{R_{nd_i}} = \frac{R'_{nd_i}}{R_{nd_i}}. \tag{5.11}$$

If the measured transfer function for a specific outlet *i* is broader than that predicted from theory, $f_{R_{nd_i}}$ will be lower than unity.

The parameter f_{G_i} adjusts the asymptotic behavior of the 3MO-DMA resolution at the diffusing limit, which theoretically (i.e., without using any broadening parameters) is given by:

$$R_{diff_i} = \frac{1}{2\sqrt{2ln2}} \times \frac{1}{\sigma_i^*} = \frac{1}{2\sqrt{2ln2}} \left[\frac{neV}{kTG_i \ln\left(\frac{R_1}{R_2}\right)} \right]^{1/2}. \tag{5.12}$$

Here, σ_i^* is the total spread parameter of the transfer function of the *i*th outlet with a midpoint mobility diameter $Z_{\mathrm{p}_i}^*$, *k* is the Boltzmann constant and *T* the absolute temperature. When the parameter f_{G_i} is used, Eq. 5.12 changes to:

$$R_{diff_i}{}' = \frac{1}{2\sqrt{2ln2}} \times \frac{1}{\sigma_i'^*} = \frac{1}{2\sqrt{2ln2}} \left[\frac{neV}{kTf_{G_i}G_i \ln\left(\frac{R_1}{R_2}\right)} \right]^{1/2}, \tag{5.13}$$

where $\sigma_i'^*$ is now the total adjusted spread parameter. In a similar fashion with Eq. 5.11, a factor for comparing the measured versus the theoretical resolution in the non-diffusing limit is defined as:

$$f_{R_{diff_i}} = \frac{R_{diff_i}{}'}{R_{diff_i}}. \tag{5.14}$$

In this case, if the measured transfer function of the *i*th outlet is broader than that predicted by theory, f_{G_i} will be higher than unity, while $f_{R_{diff_i}}$ smaller.

Similarly to the comparison described in Giamarelou et al. (2013), a non-linear least square fitting algorithm based on the interior-reflective Newton method (Coleman and Li, 1994, 1996) was employed for comparing the measurements with the theory (i.e., Eq. 5.5). The flow rates (i.e., sheath, excess, aerosol in and sample out), the pressure and temperature of both DMAs and the voltages of DMA-1, were allowed to vary within ± 1% of the measured values, accounting for the associated experimental uncertainty. Larger variation (up to 30%) was allowed for the particle number concentrations upstream DMA-2 (i.e., N_1), to account for any instabilities in the particle generator and diffusional losses in the tubing

connecting the single DMA with the 3MO-DMA and the latter to the uCPC. The diffusional losses of the sampled monodisperse particles inside the inner electrode of the 3MO-DMA were taken into account as they affect the particle number concentration coming through each outlet. The total adjustable spread parameter of the transfer function $\tilde{\sigma}_{2i}{}'^2$ was fitted once by varying f_{G_i} and once by modifying $\sigma^2_{\mathrm{mix}i}$.

The experimental resolution of the 3MO-DMA was expressed as the inverse of the Full Width Half Maximum (FWHM) of the fitted transfer function normalized by the centroid mobility of each outlet.

5.3. Results and Discussion

The performance of the 3MO-DMA was evaluated using monodisperse particles of different sizes (see discussion below), when operated with aerosol flows ranging from 0.3 to 1.5 lpm and sheath flows from 3.0 to 8.0 lpm (cf. Table 5.2, for more details). The aerosol flow was controlled by the uCPC, while the maximum sheath flow-rate by the sheath recirculating system.

Table 5.2: Ratio between measured and theoretical resolutions of each outlet of the 3MO-DMA at the diffusive (f_{Rdiff}) and the non-diffusive (f_{Rnd}) limit, when operated at different flow conditions (cf. Eq. 5.11 and 5.14).

Q_{sh} (lpm)	Q_a (lpm)	Outlet	f_{Rdiff}	f_{Rnd}
3.0	0.3	3	1.00	0.991
		2	0.490	0.461
		1	0.987	0.981
6.0	0.6	3	-	0.984
		2	0.553	0.526
		1	1.05	0.997
8.0	0.3	3	0.992	0.978
		2	0.398	0.257
		1	0.939	0.970
8.0	1.5	3	-	0.998
		2	0.882	0.895
		1	0.987	0.996

Figure 5.3 shows an example of the measured size distributions and the predictions from Eq. 5.5, using the theoretical 3MO-DMA transfer function without and with using

broadening parameters (i.e., using Eqs. 5.7 and 5.8, respectively). In the latter case the fitting procedure was able to reproduce the observed mobility distributions with a normalized root mean square error (NRMSE) of less than 3% in 82% of the experimental data, whereas the maximum observed NRMSE (i.e., worst case of fitting) was approximately 6.2%. The fitted sample flow-rates of each outlet corroborated our design calculations, based on which 24% of the sample flow comes out of outlet #3, 33% out of outlet #2, and 43% out of outlet #1 (cf. sect. 5.2.1).

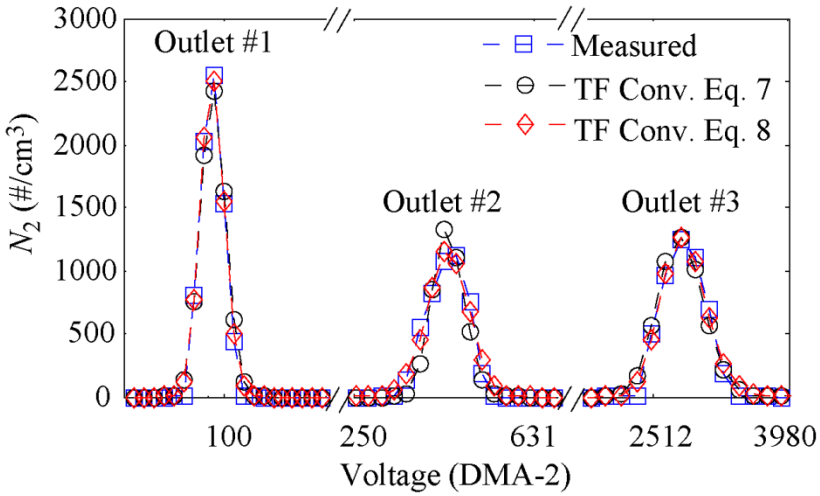

Fig. 5.3: Example of measured, as well as theoretically predicted without (i.e., using Eq. 5.7) and with (i.e., using Eq. 5.8) broadening parameters, particle number concentrations downstream the 3MO-DMA, for 40-nm particles at 3.0, 0.3 lpm of sheath and aerosol, respectively.

As shown in Fig. 5.4, the fitting procedure (cf. sect. 5.2.2.2) reproduced the experimental results in terms of the midpoint mobility diameters within 3% accuracy in all the cases, even without using any broadening parameters. This suggests that for a fixed geometry and operating conditions Eq. 5.1 can be re-arranged to predict the midpoint electrical mobility for each outlet.

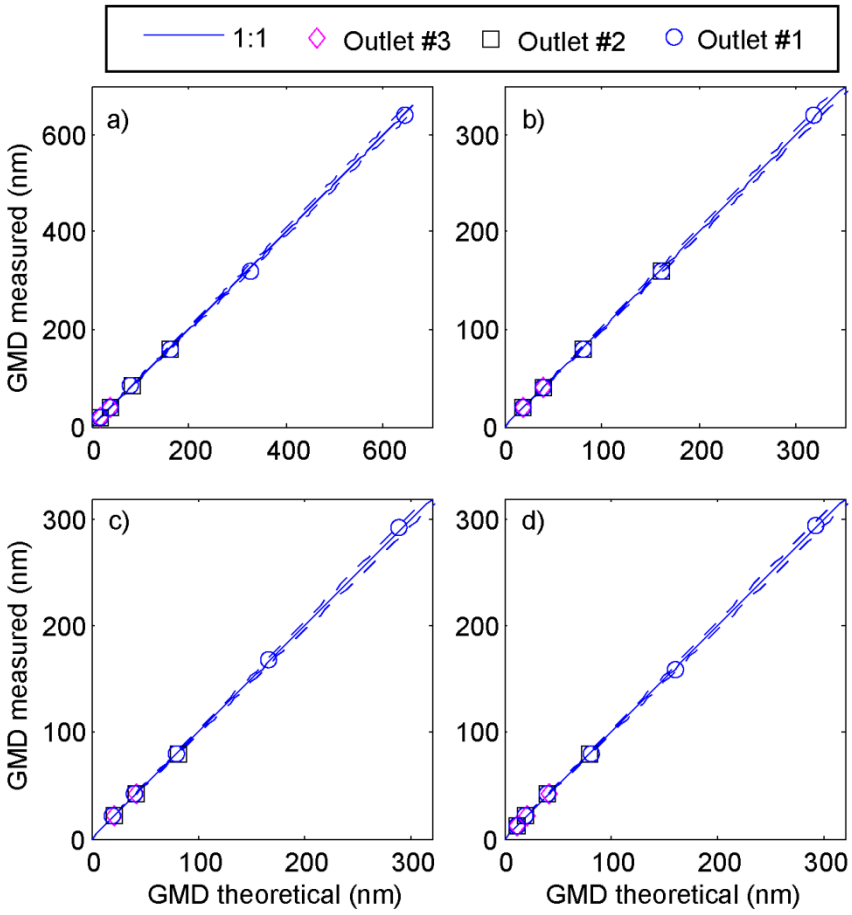

Fig 5.4: Measured vs. theoretically predicted geometrical mean diameters (GMD) of particles classified by the 3MO-DMA, when operated with 3 and 0.3 (**a**), 6 and 0.6 (**b**), 8 and 0.3 (**c**), 8 and 1.5 (**d**), sheath and aerosol flow rates, respectively.

Figure 5.5 shows the measured and predicted resolution without and with using the broadening parameters for each outlet of the 3MO-DMA. Table 5.2 also provides the median values of $f_{R_{diff_i}}$ and $f_{R_{nd_i}}$ for each set of flow rates, obtained by dividing the resolutions determined from the measurements/fits with the ones calculated from the theory, at the diffusing and non-diffusing limits, respectively. Overall, as theory predicts, the measured resolution of each outlet increased as the sheath to aerosol ratio increased. For outlets #1 (i.e., the one furthest from the aerosol inlet) and #3 (i.e., the one closest to the aerosol inlet) the ratios of the measured and the theoretical resolutions at the diffusing (i.e., $f_{R_{diff_i}}$) and at the non-diffusing limit (i.e., $f_{R_{nd_i}}$) differ by less than 6% (cf. Table 5.2).

This indicates that under all tested flow conditions the theory can accurately predict the width of the transfer functions and thus the resolutions of these two outlets of the 3MO-DMA when particles of different sizes are classified.

In contrast, the measured resolution for outlet #2 differs significantly from that predicted theoretically. More specifically, when the 3MO-DMA is operated with a sheath to aerosol ratio of 10 (i.e., 3.0 or 6.0 lpm sheath flow and respectively 0.3 or 0.6 lpm aerosol flow) the resolution of this outlet reduces by 54-47% (cf. Table 5.2). At a sheath to aerosol ratio of 26.7 (i.e., 8.0 and 0.3 lpm, sheath and aerosol, respectively) the measured resolution of outlet #2 deviates by almost 74%. Better agreement (i.e., within 12%) with the theoretical resolution of outlet #2 was achieved when the 3MO-DMA was operated with a sheath to aerosol ratio of 5.33 (i.e., 8.0 and 1.5 lpm, sheath and aerosol, respectively).Similar deviations between the measured and the theoretical resolution of outlet #2 were also obtained for the diffusing limit.

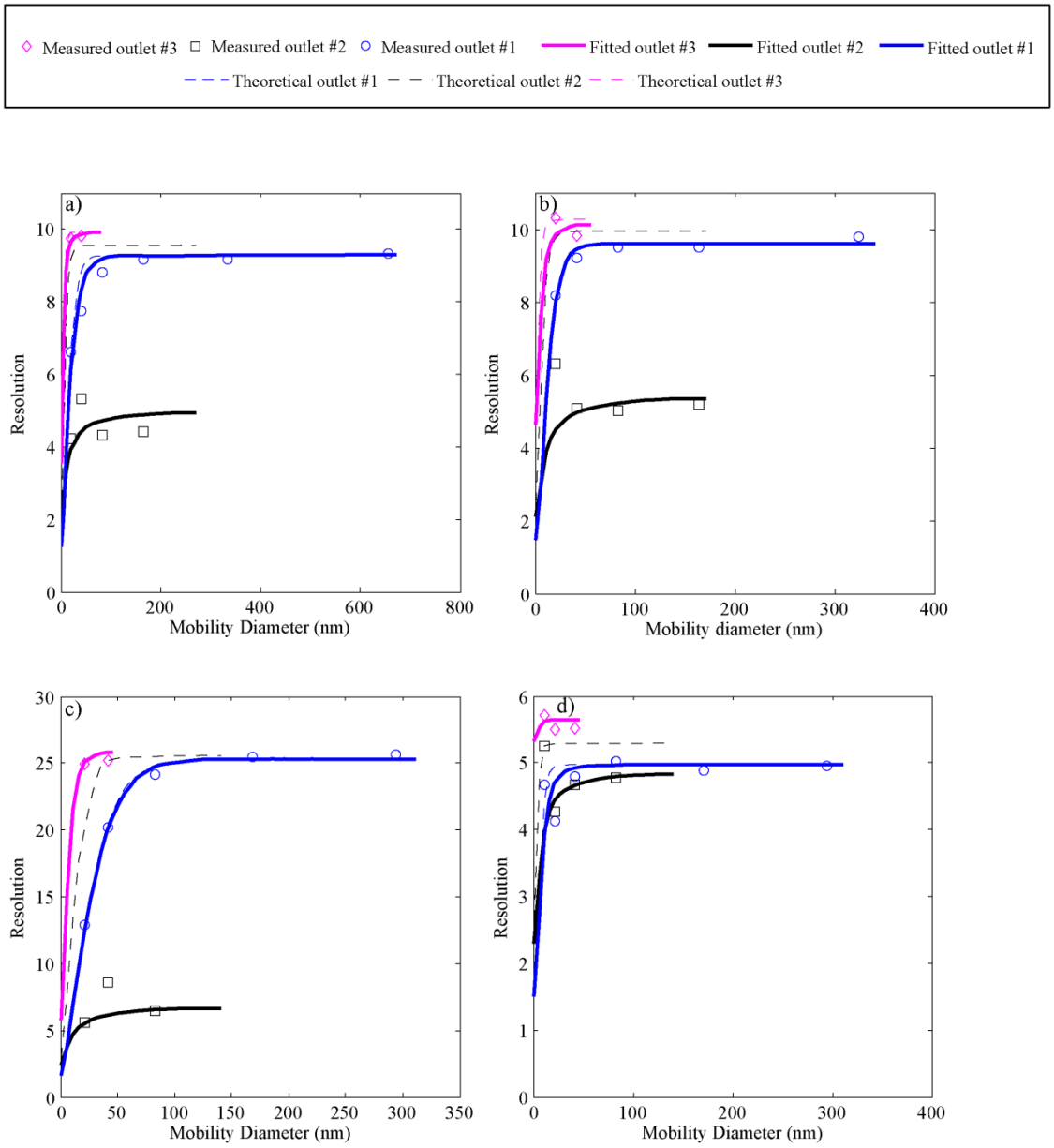

Fig. 5.5. Resolution (1/FWHM) of each outlet of the 3MO-DMA, when operated at 3.0 and 0.3 (**a**), 6.0 and 0.6 (**b**), 8.0 and 0.3 (**c**), 8.0 and 1.5 (**d**) lpm, of sheath and aerosol flows. The resolutions were estimated by convoluting the transfer functions of the DMAs used in the experimental setup, using fitted adjustable broadening parameters (i.e., f_{G_i} or $\sigma^2_{\mathrm{mix}i}$) for the 3MO-DMA transfer function (i.e. Eq. 5.8) for matching the experimentally obtained size distributions (cf. sect. 5.2.2.2 and Fig. 5.3). The theoretical resolutions (dashed lines) of each outlet of the 3MO-DMA are obtained using Eq. 5.7. Fitted resolutions are obtained using the median values of the broadening parameters which were obtained from each data set (sheath/aerosol flow rates) in Eq. 5.8.

As discussed above, the measured resolution of outlet #2 was significantly lower than that predicted theoretically and even less than that of outlet #3 in all cases, despite the contradicting theoretical predictions (cf. Giamarelou et al., 2012). Strangely, the measured resolution is closer to the theoretical resolution of this outlet when the 3MO-DMA was operated with a sheath to aerosol flow ratio of 5.33 (i.e., sheath 8 and aerosol 1.5 lpm, cf. Fig 5.5d). This indicates that the reduced resolution of outlet #2 is not a result of significant flow disturbances in the classification zone of the 3MO-DMA. CFD simulations (cf. sect. S5.2 in the supplement) corroborate this indication, whereas experiments during which outlet #3 of 3MO-DMA was tapped (data not shown here), also showed that the presence of the outlet does not affect the performance of outlet #2.

Despite the reduced resolution of the middle outlet, the spread of the measured size distributions obtained from this outlet in terms of their geometric standard deviations (σ_g), was sufficiently monodisperse for TDMA measurements. In general, the σ_g values obtained for all the outlets at all operated conditions, were below 1.09. More specifically, at the highest tested sheath to aerosol ratio (i.e., 26.7) the σ_g values obtained for the outlets #1 and #3 were 1.03, while that obtained for outlet #2 was 1.05. At the lowest tested sheath to aerosol ratio (i.e., 5.33) the respective σ_g values were 1.09, 1.08 and 1.06 for outlets #1-3.

5.4. Conclusions

We designed, built and tested a 3MO-DMA with the 3 outlets located on the central rod of a classical cylindrical DMA (TSI Model 3081), which opens new opportunities for tandem DMA measurements. To achieve this, we replaced the inner electrode of the TSI DMA, with one having three monodisperse outlets. The mobility diameters of these populations are easily distinguishable when their size distributions are measured by a second, single monodisperse outlet DMA operated in voltage scanning mode. Such a DMA can reduce the measuring cycle of size resolved measurements.

The performance of this 3MO-DMA was tested using a tandem DMA configuration at four different flow conditions. The measurements were compared with predictions from the model derived by Giamarelou et al. (2012). The results show that the theory can accurately (within 3%) predict the geometric mean diameter of the sampled particles for all the outlets. The resolution (i.e., the inverse FWHM) of each outlet was estimated by using

fitted, adjustable broadening parameters for the diffusing and non-diffusing limits of the transfer function. Both measurements and predictions show that the resolution of each outlet increased as the sheath to aerosol ratio increased. The measured resolutions of the first and the third outlet are in good agreement with the theoretically predicted ones (i.e., less than 6% difference). However, the measured resolutions of the second outlet were lower than what the theory predicts, without being affected by significant flow disturbances in the classification zone of the 3MO-DMA. Higher deviations from the theory in terms of resolution were observed at higher sheath to aerosol ratios, ranging from approx. 10% to 74% at ratios 5.33 and 26.67, respectively. Despite these discrepancies the geometric standard deviation of the size distributions of the particles classified from this outlet were not broader than 1.08 and can be used for determining the hygroscopic properties of these particles.

References

Agarwal, J. K. and Sem, G. J. (1980). Continuous flow, single-particle-counting condensation nucleus counter. *J. Aerosol Sci.*, 11:343–357.

Attoui, M., Paragano, M., de la Mora, J. F. (2013).) Tandem DMA Generation of Strictly Monomobile 1–3.5 nm Particle Standards, *Aerosol Sci. Technol*, 47:5, 499-511.

Barmpounis, K., Maisser, A., Schmidt-Ott, A., Biskos, G. (2016). Lightweight differential mobility analyzers: Toward new and inexpensive manufacturing methods. *Aerosol Sci. Technol.* 50:1, 2-5.

Bezantakos, S., Barmpounis, K., Giamarelou, M., Bossioli, E., Tombrou, M., Mihalopoulos, N., Eleftheriadis, K., Kalogiros, J., Allan, J. D., Bacak, A., Percival, C. J., Coe, H. and Biskos, G. (2013) Chemical Composition and Hygroscopic Properties of Aerosol Particles over the Aegean Sea. *Atmos. Chem. Phys.* 13: 11595-11608.

Biskos, G., Reavell, K. and Collings, N. (2005). Unipolar Diffusion Charging of Aerosol Particles in the Transition Regime. *J. Aerosol Sci.*, 36: 247–65.

Biskos, G., Paulsen, D., Russell, L. M., Buseck, P. R. and Martin, S. T. (2006). Prompt Deliquescence and Efflorescence of Aerosol Nanoparticles. *Atmos. Chem. Phys.*, 6: 4633–4642.

Chen, D., Pui, D. Y. H. Hummes, D., Fissan, H., Quant, F. R. and Sem, G. J. (1996). Nanometer differential mobility analyzer (Nano-DMA): design and numerical modeling. *J. Aerosol Sci*. 27: S137-S138.

Chen, D., Pui, D. Y. H. Hummes, D., Fissan, H., Quant, F. R. and Sem, G. J. (1998). Design and evaluation of a nanometer aerosol differential mobility analyzer (Nano-DMA), *J. Aerosol Sci*. 29 (5/6): 497-500.

Chen, D. R., Li, W., and Cheng, M. D. (2007). Development of a Multiple-Stage Differential Mobility Analyzer (MDMA). *Aerosol Sci. Technol*., 41:217–230.

Coleman, T. F., and Li, Y. (1994). On the Convergence of Reflective Newton Methods for Large-Scale Nonlinear Minimization Subject to Bounds. *Math. Program.*, 67:189–224.

Coleman, T. F., and Li, Y. (1996). An Interior, Trust Region Approach for Nonlinear Minimization Subject to Bounds. *SIAM J. Optimiz.*, 6:418–445.

Giamarelou, M., Stolzenburg, M., and Biskos, G. (2012). The Multiple Monodisperse Outlet Differential Mobility Analyzer: Derivation of its Transfer Function and Resolution. *Aerosol Sci. Technol.*, 46:951–965.

Giamarelou, M., Stolzenburg, M., Chen., D. R. and Biskos, G. (2013). Comparison Between the Theoretical and Experimental Performance of a Differential Mobility Analyzer with Three Monodisperse-Particle Outlets, *Aerosol Sci. Technol.*, 47: 406-416

Giamarelou, M., Eleftheriadis, K., Nyeki, S., Tunved, P., Torseth, K. and Biskos, G. (2016). Indirect Evidence of the Composition of Nucleation Mode Atmospheric Particles in the High Arctic. *J. Geophys. Res.-Atmos.* 121: 965–975.

Gormley, P.G., Kennedy, M. (1949). Diffusion from a stream flowing through a cylindrical tube. *P. Roy. Irish Acad*. 52: 163-169.

Haywood, J. and Boucher, O., (2000). "Estimates of the direct and indirect radiative forcing due to tropospheric aerosols: A review", *Rev. Geophys*., 38: 513–543.

Hinds, W. C. (1999). *Aerosol Technology: Properties, Behavior, and Measurement of Airborne Particles*. 2nd ed., John Willey & Sons, Inc.

Juan, L. & de la Mora, J. F. (1998). High resolution size analysis of nanoparticles and ions:

Running a Vienna DMA of near optimal length at Reynolds numbers up to 5000. *J. Aerosol Sci.*, 29 , 617.626.

Keady, P.B., 1987. Development and field testing of a sulfur aerosol and gas monitor using a pulsed precipitator. University of Minnesota.

Knutson, E.O., Whitby, K.T. (1975). Aerosol classification by electric mobility: Apparatus, theory, and applications. *J. Aerosol Sci*., 6: 443-451.

Leith, D., Mehta, D., 1973. Cyclone performance and design. *Atmos. Environ.* 7: 527-549.

Marple, V.A., 1970. A fundamental study of inertial impactors, Ph.D. Thesis, Department of Mechanical Engineering, University of Minnesota, Minneapolis, MN.

McMurry, P. H. (2000). A review of atmospheric aerosol measurements. *Atmos. Environ*., 34:1959-1999.

Ogren, J. and Charlson, J. (1992). Implications for models and measurements of chemical inhomogeneities among cloud droplets, *Tellus*, 44B, 489–504.

Rader, D., J. and McMurry P., H. (1986). Application of the tandem differential mobility analyzer to studies of droplet growth or evaporation. *J. Aerosl Sci.* 17: 771-787.

Santos, J. P., Hontañón, E., Ramiro, E., Alonso, M. (2009). Performance evaluation of a high resolution parallel-plate differential mobility analyzer. *Atmos. Chem. Phys.*, 9: 2149-2429.

Seinfeld J., H. and Pandis S., N. (2006). *Atmospheric Chemistry and Physics.* 2nd ed., John Willey & Sons, Inc.

Stolzenburg, M. (1988). An Ultrafine Aerosol Size Distribution Measuring System. Ph.D. Thesis, University of Minnesota, St. Paul, MN.

Stolzenburg, M. R. and McMurry, P. H., (1991). An Ultrafine Aerosol Condensation Nucleus Counter, *Aerosol Sci. Technol*, 14: 48-65.

Wang, C. S., Flagan C. R. (1990). Scanning Electrical Mobility Spectrometer, *Aerosol Sci. Tech*. 13: 230-240.

Zhang, S. H., Akutsu, Y., Russell, L. M., Flagan, R. C., Seinfeld J. H. (2007). Radial Differential Mobility Analyzer, *Aerosol Sci. Tech*. 23: 357-372.

Supplement

Modification of theTSI 3081 Differential Mobility Analyzer to include three Monodisperse Outlets : Comparison between experimental and theoretical performance

S. Bezantakos, M. Giamarelou, L. Huang, K. Barmpounis, J. Olfert and G. Biskos

S5.1. Supporting Equations

The diffusion coefficient of the particles suspended in a gas is given by (Hinds 1999):

$$D_{\mathrm{p}} = \frac{kTCc}{3\pi\eta d_p}, \quad \text{(S5.1)}$$

where k is the Boltzmann constant (1.38×10^{-23} J/K), T is the absolute temperature, η is the air viscosity (1.81×10^{-5} kg/ms), d_{p} is the particle diameter and C_c is the Cunningham slip correction factor given by:

$$Cc = 1 + \frac{\lambda}{d_p} \times \left(2.34 + 1.05 \times exp\left(-0.39 \times \frac{d_p}{\lambda}\right)\right). \quad \text{(S5.2)}$$

Here λ is the air mean free path (66×10^{-9} m at atmospheric pressure).

The dimensionless electrical mobility of the particles classified by the single outlet DMA is given by Stolzenburg (1988) :

$$\tilde{Z}_{\mathrm{p1}} = \frac{Z_{\mathrm{p}}}{Z^*_{\mathrm{p_1}}}, \quad \text{(S5.3)}$$

where Z_{p} is the particles electrical mobility and $Z^*_{\mathrm{p_1}}$ is the central electrical mobility of particles classified by the DMA.

For the 3MO-DMA the dimensionless electrical mobility of the particles classified by each outlet is given by Giamarelou (2012):

$$\tilde{Z}_{\mathrm{p2}} = \frac{Z_{\mathrm{p}}}{Z^*_{\mathrm{p2i}}}, \quad \text{(S5.4)}$$

where Z^*_{p2i} is the central electrical mobility of particles classified by the each monodisperse outlet of the 3MO-DMA.

The dimensionless flow parameters for the single, cylindrical DMA are given by (Knutson and Whitby, 1975) and Stolzenburg (1988):

$$\beta_1 = \frac{Q_s + Q_a}{Q_{sh} + Q_m} \text{ and} \quad \text{(S5.5)}$$

$$\delta_1 = \frac{Q_s - Q_a}{Q_s + Q_a}, \quad \text{(S5.6)}$$

where Q_s, Q_a are the flows of the monodisperse sample and aerosol inlet, while Q_{sh} and Q_m are the sheath and excess flows.

Similarly for the 3MO-DMA the dimensionless flow parameters are obtained using (Giamarelou et al., 2012):

$$\beta_2 = \frac{Q_{si} + Q_a}{Q_{shi} + Q_{mi}} \text{ and}$$

$$\delta_2 = \frac{Q_{si} - Q_a}{Q_{si} + Q_a},$$

where i stands for the number of each monodisperse outlet.

The dimensionless diffusional broadening parameter for each monodisperse outlet i of the 3MO-DMA be expressed as:

$$\tilde{\sigma}_{2i} = \sqrt{\widetilde{D}_i G_i} \quad , \quad \text{(S5.7)}$$

where $\widetilde{D}_i$ is the dimensionless diffusion coefficient equal to:

$$\widetilde{D}_i = \frac{4\pi L_i D_{\mathrm{p}}}{Q_{shi} + Q_{mi}}, \quad \text{(S5.8)}$$

and G_i is a unique geometric- and flow-condition-dependent parameter which is given by (Giamarelou et al., 2012):

$$G_i = \sum_{j=n}^{i} G_{i,j} \quad \text{(S5.9)}$$

and

$$G_{i,j} = G_{i,j,axial} + G_{i,j,radial} \quad \text{(S5.10)}$$

where:

$$G_{i,j,axial} = 4\left(\frac{Q_{tj}}{Q_{ti}}\right)^2 \frac{(1+\beta_i)^2}{(1-\gamma)} \left[I_\gamma\left(\omega_{i,\mathrm{j},d}\right) - \left(\omega_{i,j,u}\right)\right] \quad \text{(S5.11)}$$

and

$$G_{i,j,radial} = \left(\frac{R_2}{L_i}\right)^2 \left(\omega_{i,j,u} - \omega_{i,j,d}\right). \quad \text{(S5.12)}$$

Q_{tj}, Q_{ti} are the total flows corresponding to the jth and ith segments of the 3MO-DMA and $\omega_{i,j,u}$ and $\omega_{i,j,d}$ are respectively the upstream and downstream dimensionless radial positions in the jth segment for particles having mobility corresponding to the centroid mobility of the transfer function of the ith outlet.

For plug flow:

$$I_\gamma(\omega) = \frac{(1-\omega^2)}{2(1-\gamma)}\ , \quad \text{(S5.13)}$$

and for Poiseuille flow:

$$I_\gamma(\omega) = A_\gamma^2(1-\gamma)^{-1}\left\{-\frac{1}{2}\omega^2[(1-\gamma)ln\omega-(1-\omega)ln\gamma]^2+\left[\frac{1}{2}\omega^2(1-\gamma)+\frac{1}{3}\omega^3 ln\gamma\right]\times\right.$$
$$\left. 1-\gamma ln\omega-1-\omega ln\gamma+141-\omega 21-\gamma 2+5181-\omega 31-\gamma ln\gamma+1121-\omega 4ln2\gamma\right. \quad ,$$

(S5.14)

with

$$\omega = \left(\frac{r}{R_2}\right)^2 \text{ and} \quad \text{(S5.15)}$$

$$\gamma = \left(\frac{R_1}{R_2}\right)^2, \quad \text{(S5.16)}$$

where R_1 and R_2 are respectively the inner and outer radii of the 3MO-DMA and r is the particles radial position.

The upstream and downstream endpoints (i.e., $\omega_{i,j,u}$and $\omega_{i,j,d}$) can be estimated by the fraction of flow between ω and γ (i.e., $F_\gamma(\omega)$) as:

$$F_\gamma(\omega_{i,j,u}) = \frac{Q_i(L_{j+1})}{Q_{tj}} = \frac{L_{j+1}}{L_i}\times\frac{(Q_{shi}+Q_{mi})}{2Q_{tj}}+\frac{Q_a}{2Q_{tj}} \text{ and} \quad \text{(S5.17)}$$

$$F_\gamma(\omega_{i,j,d}) = \frac{Q_i(L_j)}{Q_{tj}} = \frac{L_j}{L_i}\times\frac{(Q_{shi}+Q_{mi})}{2Q_{tj}}+\frac{Q_a}{2Q_{tj}}, \quad \text{(S5.18)}$$

where L_{j+1} and L_j are the lengths between the aerosol inlet and the j+1st and jth monodisperse outlets, respectively. Q_{tj} is the total flow through the jth segment and $Q_i(z)$ is the flow between the trajectory and the axial position z and the outer wall (i.e., R_2) given by (Giamarelou et al., 2012):

$$Q_i = \frac{Z}{L_i}\times\frac{(Q_{shi}+Q_{mi})}{2}+\frac{1}{2}Q_a\ .$$

The ratio Q_i/Q_{tj} is the flow fraction between the particle trajectory at r, z and the outer wall of the 3MO-DMA (i.e., R_2), where z is the jth segment.

In case of plug flow the flow fraction is given by:

$$F_\gamma(\omega) = \frac{1-\omega}{1-\gamma} \text{ and} \quad \text{(S5.19)}$$

in case of Poiseuille flow is given by (Stolzenburg 1988):

$$F_\gamma(\omega) = -A_\gamma\left[\frac{(1-\omega)^2}{2(1-\gamma)}ln\gamma+\omega ln\omega+(1-\omega)\right], \quad \text{(S5.20)}$$

where:

$$A_\gamma = \left[-\frac{1}{2}(1+\gamma)ln\gamma - (1-\gamma)\right]^{-1} . \quad \text{(S5.21)}$$

Epsilon (ε) function is defined as:

$$\varepsilon(x) = x \times \text{erf}(x) + \frac{1}{\sqrt{\pi}}\exp(-x^2) \text{ and} \quad \text{(S5.22)}$$

$$\text{erf}(x) = \frac{2}{\sqrt{\pi}}\int_0^x \exp(-u^2)\, du . \quad \text{(S5.23)}$$

S5.2. Finite Element Model for Simulating the Flow Velocity field within the 3MO-DMA

In order to study any flow disturbances inside the 3MO-DMA, which could pose a possible reason for the reduced resolution of outlet #2 (cf. sect. 5.3) a 2D axisymetric numerical model, created in COMSOL Multiphysics® was employed to simulate the profiles of the flows within the 3MO-DMA. The design of the 3MO-DMA which was used in this model, incorporated the main geometrical features and dimensions (cf. Fig. S5.1a, herein and Fig. 5.1, Table 5.1). Since in a 2D axisymetric model the monodisperse outlets cannot be designed as constructed in reality (i.e., 12 holes in the circumference of each outlet slit; cf. Fig. 5.1) we used 3 narrow regions as monodisperse outlets in the model. Each region resembles to an opening through which air will move with an area equal to the total area of the holes of each outlet. With this feature the model was able to reproduce the experimental monodisperse sample flows of each outlet. Assuming that the air flowing inside the 3MO-DMA had a constant temperature of 25 C and based on the flow rates used in the experiments we used the *Laminar Flow* module of COMSOL Multiphysics® to calculate the flow velocity profiles inside the 3MO-DMA. The Navier-Stokes equations for incompressible flow have the form of:

$$\rho(u\cdot\nabla)u = \nabla\cdot[-p\mathrm{I} + \mu(\nabla u + (\nabla u)^T] + F \text{ and} \quad \text{(S5.24)}$$

$$\rho\nabla\cdot u = 0 , \quad \text{(S5.25)}$$

where u is the velocity vector, ρ and μ are respectively the density and dynamic viscosity of air, p is the pressure, T is the absolute temperature, F is the volume force vector and I is the identity matrix.

Figures S5.1b and S5.1c show the velocity profiles and the streamlines in the vicinity of the aerosol inlet and monodisperse outlets when the sheath and aerosol flows were 3.0, 0.3 and 8.0, 1.5 lpm, respectively. The streamlines show that the particles

trajectories in the vicinity of an outlet will be affected by the sample outflow, corroborating the use of the unique geometric- and flow-condition-dependent parameter G_i (cf. Eq. S5.9 and Giamarelou et al., 2012 for more details) for obtaining the theoretical transfer function of the 3MO-DMA. Using this parameter the theory was able to reproduce quite accurately (i.e., within 6%) the experimental results, in terms of resolution, for outlets #3 and #1 (cf. sect. 5.3). Except from this effect, which is taken into account by the theory, no other flow disturbances are present in the classification zone of the 3MO-DMA. According to the simulation some eddies appear inside the hollow inner electrode as sample flow is forced through the narrow region of the monodisperse outlet. If they were affecting the resolution of the 3MO-DMA the deviations between the theory and the measurements should be maximized under the highest flow conditions, (i.e., sheath 8.0 and total sample flow of 1.5 lpm) since they are more pronounced at these flow rates (cf. Fig S5.1c). Based on the experimental results however, which show the best agreement between the theoretical and measured resolutions for all the monodisperse outlets at these flow rates (i.e., sheath 8.0 and aerosol 1.5 lpm; cf. sect. 5.3 and Fig. 5.5) we conclude that they do not affect the resolution of the 3MO-DMA.

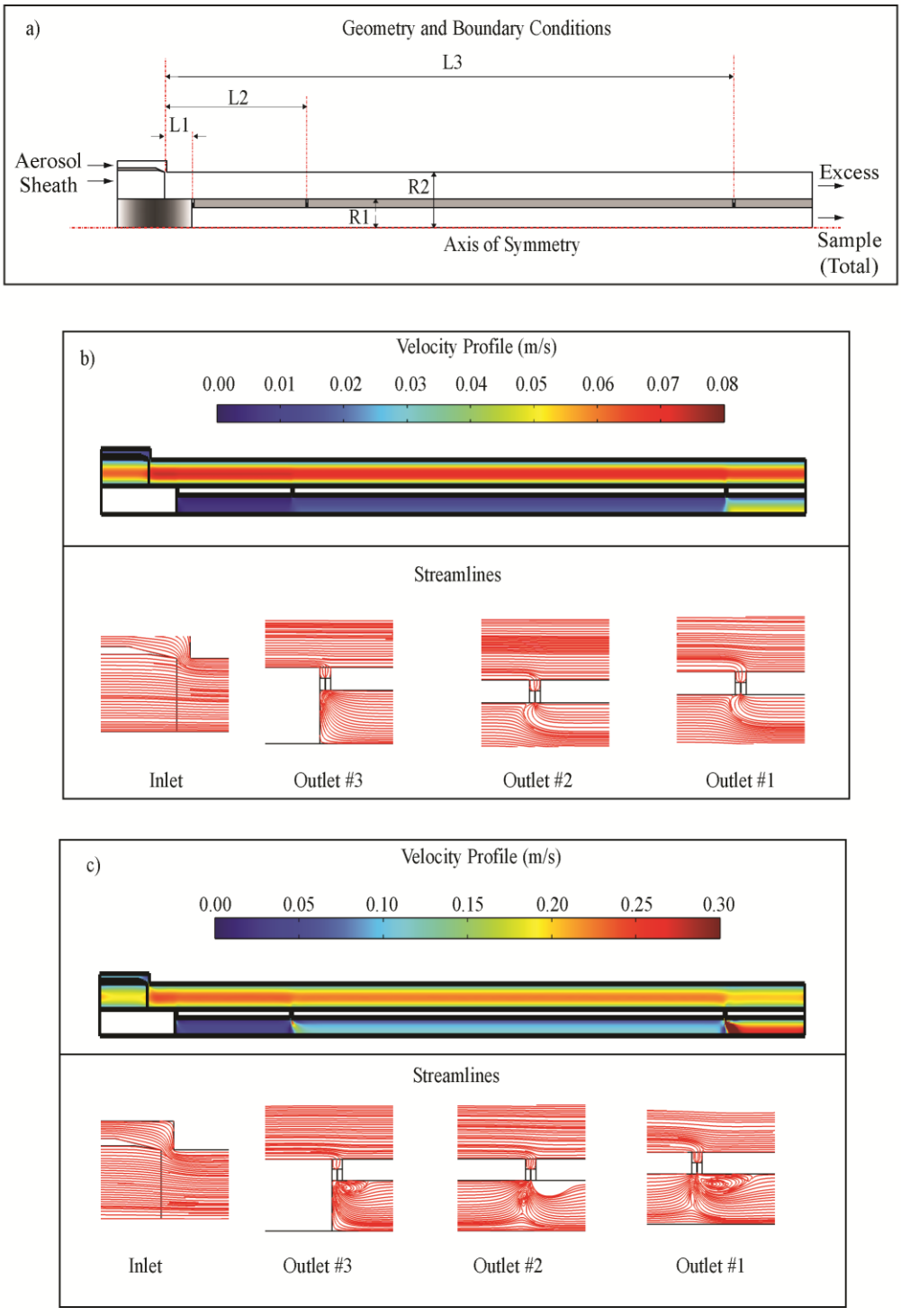

Fig. S5.1. Modeled results of the 3MO-DMA's flow velocity profiles and details of the streamlines at the proximity of the aerosol inlet and each monodisperse outlet. The simulations were conducted using Comsol multiphysics® software, maintaining the 3MO-DMA's design key features (**a**) and when the flows of sheath and aerosol were 3.0, 0.3 (**b**) and 8.0, 1.5 (**c**).

References

COMSOL® multiphysics version 4.3b. *Reference manual*. Stockholm, Sweden: COMSOL AB

Giamarelou, M., Stolzenburg, M., and Biskos, G. (2012). The Multiple Monodisperse Outlet Differential Mobility Analyzer: Derivation of its Transfer Function and Resolution. *Aerosol Sci. Technol.*, 46:951–965.

Hinds, W. C., (1999). Aerosol Technology: Properties, Behavior, and Measurement of Airborne Particles. (2nd ed.). New York: John Willey & Sons, Inc., (Chapter 7)

Stolzenburg, M. (1988). An Ultrafine Aerosol Size Distribution Measuring System. Ph.D. Thesis, University of Minnesota, St. Paul, MN.

6. A Cost-Effective Electrostatic Precipitator for Aerosol Nanoparticle Segregation

S. Bezantakos[1,2], L. Huang[3], K. Barmpounis[3], M. Attoui[4],
A. Schmidt-Ott[3] and G. Biskos[1,3,5,6]

[1]*Department of Environment, University of the Aegean, Mytilene 81100, Greece*
[2]*Institute of Nuclear Technology and Radiation Protection, NCSR Demokritos, 15310 Ag. Paraskevi, Attiki, Greece*
[3]*Faculty of Applied Sciences, Delft University of Technology, Delft 2628-BL, The Netherlands*
[4]*University Paris Est Creteil, University Paris-Diderot, LISA, UMR CNRS 7583, France*
[5]*Faculty of Civil Engineering and Geosciences, Delft University of Technology, Delft 2628-CN, The Netherlands*
[6]*Energy Environment and Water Research Center, The Cyprus Institute, Nicosia 1645, Cyprus*

Published: January 2015
Aerosol Research Letter
Aerosol Science and Technology , 49:iv–vi, 2015

Abstract

The relative penetration of aerosol nanoparticles ranging from 10 to 55 nm through a tube made from Electrostatic Dissipative Materials (EDM) subjected to high voltage, was measured to evaluate its performance as a cost effective and portable nanoparticle classifier. The electric field inside the tube combined with the diffusion of nanoparticles increases their deposition compared to a Diffusion Battery (DB), thus the EDM classifier can be viewed as a combination of a DB and an Electrostatic Precipitator (ESP). Based on the experimental observations, numerical simulations of the electric field inside the tube and by extending the semi-empirical model employed for DBs, we propose a semi-empirical model able to predict the penetration efficiency through the classifier within ±15% of accuracy. The steep penetration efficiency curves of the EDM-tube are suitable for using it for nanoparticle classification. Furthermore the EDM classifier offers better measuring accuracy compared to an ESP, while the easier adjustment of the voltage poses an advantage over DBs. This cost effective and portable classifier can be employed in tandem systems for measuring size-dependent particles properties such as hygroscopicity and volatility.

6.1. Introduction

Measuring the size of aerosol particles having diameters smaller than 100 nm (i.e., nanoparticles) is important for assessing their environmental impacts (McMurry, 2000) and investigating their potential technological applications (Biskos *et al*., 2008). The most effective way for sizing aerosol nanoparticles is by classifying them based on their electrical mobility using differential mobility analyzers (DMAs; Knutson and Whitby, 1975). Despite that DMAs can classify particles with a high resolution by simply changing the potential difference between their two electrodes, their high cost and bulky size is limiting for widespread applications. Diffusion Batteries (DBs) that distinguish aerosol particles based on their diffusivity, can also be used as particle size classifiers (DeMarcus and Thomas, 1952). Although compact designs of DBs have been proposed, a number of technical limitations (cf. McMurry, 2000) has made them less favorable for particle size measurements compared to electrical mobility classifiers.

In this letter we introduce a simple and cost-effective method for size segregating aerosol nanoparticles by employing tubes composed of Electrostatic Dissipative Materials (EDMs). EDM tubes have surface resistivities that range from 10^5 to 10^{12} Ω/sq. Applying a potential difference along the tube creates an electric field of varying strength that has a radial and an axial component (cf. the discussion Sect. of this chapter). This field affects the charged particles passing through the tube in two ways: the axial field decelerates the particles and therefore increases their residence time in the tube and their chance for diffusional deposition to its walls, whereas the radial field removes particles by electrostatic deposition. As a result of these two processes EDM tubes can be viewed as a combination of a DB and an electrostatic precipitator (or a crude DMA), with the advantage of being significantly more simple and inexpensive.

The relative penetration efficiency of the particles passing through an EDM tube (i.e. the ratio of the particle number concentration at the outlet when a potential difference is applied along the tube over that when it is grounded) can be predicted using a modified version of the semi-empirical model employed for diffusion batteries:

$$P_r = \alpha \times \exp(-\beta \times \mu_{\text{diff}} \times \mu_{\text{elec}}) + \gamma \times exp(-\delta \times \mu_{\text{elec}}), \qquad (6.1)$$

Here α, β, γ, and δ are positive empirical constants, whereas μ_{diff} and μ_{elec} are dimensionless parameters accounting for particle deposition by diffusion and electrostatic forces, respectively. For laminar flow conditions μ_{diff} is given by (Hinds, 1999):

$$\mu_{\text{diff}} = \frac{DL}{Q}. \quad (6.2)$$

Here, D is the diffusion coefficient of the particles, L is the length of the tube, and Q is the aerosol volumetric flow rate. In a similar manner, μ_{elec} can be defined as:

$$\mu_{\text{elec}} = \frac{Z_{\text{p}}V}{Q} f_{\text{g}}, \quad (6.3)$$

where Z_{p} is the electrical mobility of the particles and f_{g} is a factor accounting for the dependence of the edge effects of the electric field to geometrical parameters, given by:

$$f_{\text{g}} = \frac{\pi d_{\text{tube}}^2}{4L_{\text{HV}}}. \quad (6.4)$$

Here d_{tube} is the inner diameter of the EDM tube and L_{HV} is the distance between the grounded inlet and the position along the tube where the high voltage is applied. Expressions for the parameters used to calculate D and Z_{p} are given in Sect. S6.1 in the supplement).

6.2. Experimental

The EDM tube (Freelin Wade, Model 1A-405-81) used in our tests had a length of 240 mm and inner diameter of 6.4 mm. Three metallic rings were attached along its length as shown in Fig. 6.1: one at the inlet, one at the outlet, and one at an intermediate point between the inlet and the outlet. The metal rings at the inlet and the outlet were grounded, while the intermediate ring was connected to a positive high-voltage power supply (Fug, Model HCN14-12 500) that can deliver up to 12.5 kV.

The experimental setup for characterizing the classifier consisted of an aerosol Spark Discharger Generator (SDG; Schwyn *et al*., 1988), a custom-made DMA (Sect. S6.2 in the supplement) with a closed recirculating system for the sheath flow, the EDM-tube and two Condensation Particle Counters (CPCs; Agarwal and Sem, 1980) as shown in Fig. 6.1. In brief, the SDG was used to produce polydisperse singly-charged silver particles of variable sizes by adjusting the energy per spark and the carrier gas flow as described by Tabrizi *et al*. (2009). Positively-charged, monodisperse particles having electrical mobility diameters from 10 to 55 nm were obtained after classification by the DMA. The

monodisperse particles were then passed through the EDM tube before their concentration was measured by an ultrafine CPC (uCPC; TSI Model 3025).

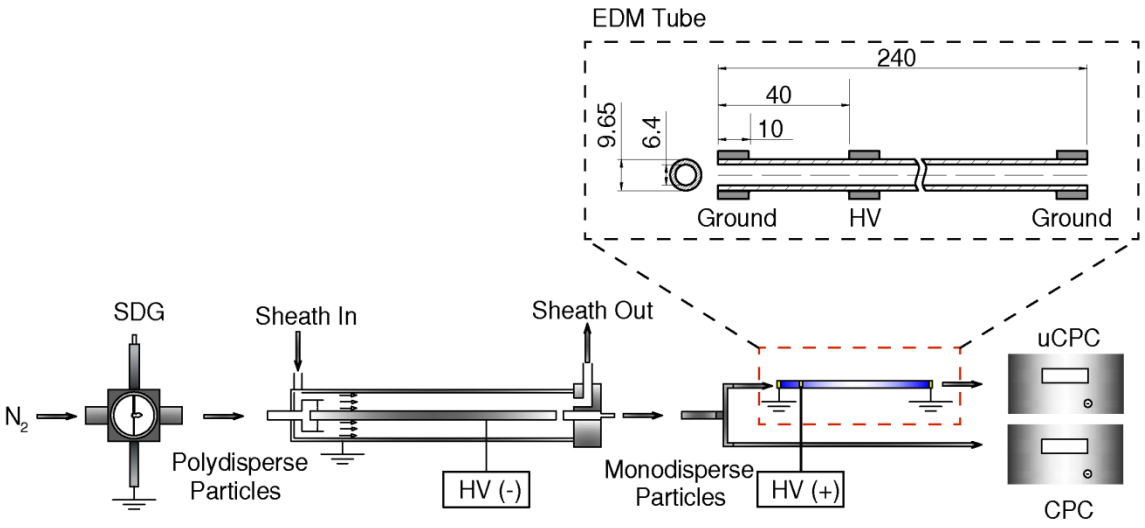

Fig. 6.1. Schematic diagram of the experimental setup and the EDM-tube classifier (inset). Metal rings are attached to the tube for grounding the inlet and the outlet, and for applying a high voltage at an intermediate point (i.e., 40 mm downstream the inlet) along the tube. A DMA was used to select monodisperse positively charged silver particles produced by a SDG. The monodisperse particles having electrical mobility diameters ranging from 10 to 55 nm were then passed through the EDM tube, which was operated at voltages ranging from zero to 8 kV. The particle number concentration was measured downstream the EDM tube by a uCPC. A CPC was used to check the stability of the number concentration of the monodisperse particles upstream the EDM tube.

The relative penetration efficiency through the EDM-tube when the applied voltage at the intermediate electrode varied from 1 to 8 kV was calculated by:

$$P_r(V) = 1 - \left(\frac{N(0)-N(V)}{N(0)}\right) = \frac{N(V)}{N(0)}. \quad (6.5)$$

Here $N(0)$ and $N(V)$ are the average particle number concentrations measured over 60 s by the uCPC downstream the EDM tube when zero and V volts were respectively applied at the intermediate electrode. A second CPC (TSI Model 3072) was used to verify that the particle number concentration upstream the EDM tube was stable throughout the measurements.

6.3. Results and Discussion

Figure 6.2 shows the measured and predicted relative penetration efficiency of particles having electrical mobility diameters from 10 to 55 nm that enter the EDM tube. Measurements are shown for two different aerosol flow rates, 0.32 and 0.76 lpm, when 1 to 8 kV were applied on the intermediate electrode of the tube. The semi-empirical model (i.e., Eq. 6.1) was fitted to the measurements using the least squares method, yielding the following constants: $\alpha = 0.65$, $\beta = 2668.83$, $\gamma = 0.35$, and $\delta = 4.21$. For all particle sizes and operating conditions tested, the agreement between predictions and measurements was within 15%, which is in the same range to the uncertainty of our setup.

For a fixed aerosol flow, the larger particles require higher potential differences between the intermediate ring electrode and the two ends of the EDM tube in order to decrease their penetration probability. When the potential difference is also fixed, the relative penetration of the particles increases logarithmically with their size, yielding curves that become steeper as particle size decreases (Fig. 6.2). The size resolving capability of the EDM tube is higher in these steep regions of the curves; a feature that is highly desirable when electrostatic precipitators are used for particle segregation. Another feature of the EDM tubes that makes them attractive classifiers is that in the steep regions of the penetration efficiency curves, the relative size resolution is almost constant. This is verified by the fact that the curves are almost parallel when a logarithmic horizontal axis is used in the plots shown in Fig. 2.

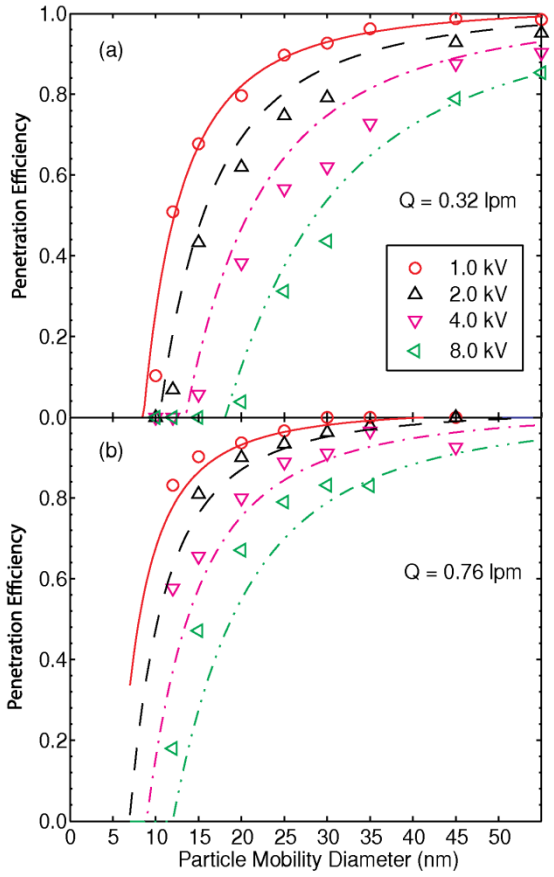

Fig 6.2. Relative penetration efficiency of particles passing through the EDM-tube classifier at a flow rate of 0.32 lpm (a) and 0.76 lpm (b). Symbols indicate experimental measurements while lines are produced using the semi-empirical model (i.e., Eq. 6.1) described in this chapter.

Interestingly, the relative penetration efficiency curves of the EDM tube are steeper compared to those of classical parallel-plate precipitators having the same cross-sectional area (Sect. S6.3 and Fig. S6.1 in the supplement), indicating that they would perform much better as classifiers. This characteristic can be attributed to the diffusional deposition of the charged particles, which is enhanced by the axial component of the electric field that can significantly decelerate the smaller charged particles in the EDM tube. To further investigate the role of the electric field on the penetration of the particles through the EMD tube, we used a numerical model to calculate its strength when 1 kV is applied at the intermediate ring electrode (Sect. S6.4 and Fig. S6.2 in the supplement). The electric field is significantly distorted near the three electrode rings, inducing a radial component that is extremely strong in their vicinity (i.e., the "Hot Spot" regions indicated in Fig. S6.2), but

decays fast along the axial and radial dimension. This component of the field attracts the positively charged particles towards the walls right at the edge of the grounded electrode ring at the inlet of the tube (i.e., "Hot Spot 1") thereby increasing the probability of their deposition. At the same time, the mean strength of the axial component of the electric field upstream (Zone 1) and downstream (Zone 2) the high voltage electrode is 30 and 5.5 kV/m, respectively (Fig. S2c). For 10-nm singly charged particles, this field can reduce the mean convective particle velocity by 0.07 m/s in Zone 1 and increase it by 0.01 m/s in Zone 2. For typical flow rates used through the EDM tubes (i.e., in the range of an lpm), this can substantially increase the residence time of the particles, if not force them to move opposite to the direction of the flow, in Zone 1 thereby increasing their probability of deposition to the tube walls. This feature is reflected by the relative penetration efficiency curves that are noticeably steeper compared to those of parallel plate precipitators as discussed above.

6.4. Conclusions

In this work we demonstrate the ability of EDM tubes to be used as effective and compact electrostatic precipitators that can be employed for size segregation of charged aerosol nanoparticles, and provide a semi-empirical model to predict their performance. These tubes can be considered a combination of a DB and an electrostatic precipitator. Compared to DBs, where only the flow rate can be adjusted to select particles of different size, EDM tubes offer higher flexibility as they can segregate particles by simply adjusting the potential difference along their inner surface. Compared to classical parallel plate electrostatic precipitators, EDM tubes exhibit steeper cut-off curves. This feature is highly attractive for their potential use in mobility spectrometers or in tandem systems downstream a DMA for measuring size-dependent particle properties such as hygroscopicity and volatility. Considering also their simple design, high portability, and negligible cost, EDM tubes can open up new opportunities in environmental monitoring as discussed above.

References

Agarwal, J. K. and Sem, G. J. (1980). Continuous flow, single-particle-counting condensation nucleus counter. *J. Aerosol Sci.*, 11:343–357.

Biskos, G., Vons, V., Yurteri, C. and Andreas, S.-O., (2008). Generation and sizing of particles for Aerosol-based Nanotechnology. *KONA Powder Part J.*, 26, 13–35.

DeMarcus, W. C. and Thomas, J. W. (1952). Theory of a Diffusion Battery. USAEC Report ORNL-1413, Oak Ridge National Laboratory, Oak Ridge, TN.

Hinds, W. C. (1999). Aerosol Technology: Properties, Behavior, and Measurement of Airborne Particles, 2nd Edition. John Willey & Sons, Inc..

Knutson, E.O., Whitby, K.T. (1975). Aerosol Classification by Electric Mobility: Apparatus, Theory, and Applications. *J. Aerosol Sci*., 6: 443-451.

McMurry, P. H. (2000). A review of Atmospheric Aerosol Measurements. *Atmos. Environ*., 34:1959-1999.

Schwyn S., Garwin E., Schmidt-Ott A. (1988). Aerosol Generation by Spark Discharge. *J Aerosol Sci.*, 19(5):639–642.

Tabrizi N. S., Ullmann M., Vons V. A., Lafont U. and Schmidt-Ott A. (2009). Generation of Nanoparticles by Spark Discharge. *J. Nanopart. Res.*, 11:315–332.

Supplement

S6.1: Supporting equations for the EDM tube penetration model:

The diffusion coefficient and the electrical mobility of the particles are respectively given by:

$$D = \frac{kTCc}{3\pi\eta d_p}, \quad \text{(S6.1)}$$

$$Z_p = \frac{neCc}{3\pi\eta d_p}, \quad \text{(S6.2)}$$

where k is the Boltzmann constant (1.38×10^{-23} J/K), T is the absolute temperature (T = 298 K for all the calculations described in the letter), η is the air viscosity (1.81×10^{-5} kg/ms), e is the electron charge (1.6×10^{-19} C), n is the number of elementary charges on the particles, d_p is the particle diameter and C_c is the Cunningham slip correction factor given by:

$$Cc = 1 + \frac{\lambda}{d_p} \times \left(2.34 + 1.05 \times exp\left(-0.39 \times \frac{d_p}{\lambda}\right)\right). \quad \text{(S6.3)}$$

Here λ is the air mean free path (66×10^{-9} m at atmospheric pressure).

S6.2: Details of the custom-made DMA used in our experiments:

A cylindrical type DMA having 0.935 and 1.9575 cm inner and outer radii, respectively, and an effective length of 11.47 cm was used in all the measurements. The sheath flow of the DMA was driven by a controlled closed loop system which included a blower, a heat exchanger, a pressure transducer connected to a laminar flow element for measuring the flow, and a PID controller. A 1:10 aerosol-to-sheath-flow ratio was used throughout all the experiments.

S6.3. Comparison EDM-tube and Parallel-Plate ESPs

Figure S6.1 compares EDM-tube penetration efficiency curves predicted by Eq. 6.1 with corresponding curves (i.e., exhibiting the same cut-off diameters at 50% penetration, d_{50}) for a parallel plate electrostatic precipitators having the same cross-sectional area as predicted by the modified Deutsch-Anderson equation (Leonard *et al*., 1967).

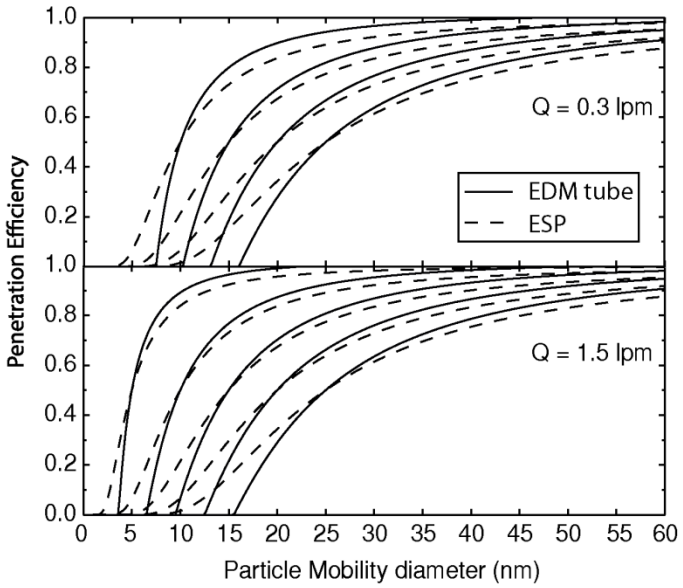

Fig. S6.1. Comparison between predicted penetration efficiency curves of the EDM tube (solid lines) and of a parallel plate electrostatic precipitator using the modified Deutsch-Anderson equation (dashed lines). For the calculations we assumed that both instruments have the same cross sectional area (i.e., 32.15 mm^2) and operate at the same flow rates: (a) 0.3 lpm, and (b) 1.5 lpm. All curves intersect at 50% penetration efficiency. The labels on each curve indicate the potential required to obtain 50% penetration efficiency for particles having dry mobility diameters of 10, 15, 20, and 25 nm.

S6.4: Numerical Model:

The electric field inside the EDM tube was numerically simulated using version 4.3b of COMSOL® multiphysics. More specifically, we developed a 2-dimensional axisymmetric model, with the axis of symmetry being the center of the tube (cf. Fig. S6.2a). The boundary conditions included the potential on the intermediate electrode (i.e., V = 1000 V) and the grounded inlet and outlet (V = 0 V). The resistivity of the EDM tube material is 4×10^{10} ohm×cm, according to the manufacturer. Since the relative permittivity of the specific material is unknown in the calculations we assumed values that range from 2.0 to 7.0, which are typical for most polyurathanes. Variation of the relative permittivity in this range had a less than 4% influence on the calculated electric field strength. The strength of the electric field within the tube was determined by solving Poisson equation:

$$-\nabla \times (\varepsilon_0 \nabla V - P) = \rho \qquad \text{(S6.4)}$$

where ε_0 is the permittivity of free space, V is the potential, P the polarization of the medium and ρ is the charge density ($\rho = 0$ in our calculations). To solve Eq. S6.4 we used an extremely fine mesh (ca. 5×10^5 elements) and the multifrontal massively parallel sparse direct solver (MUMPS; COMSOL® multiphysics 4.3b reference manual).

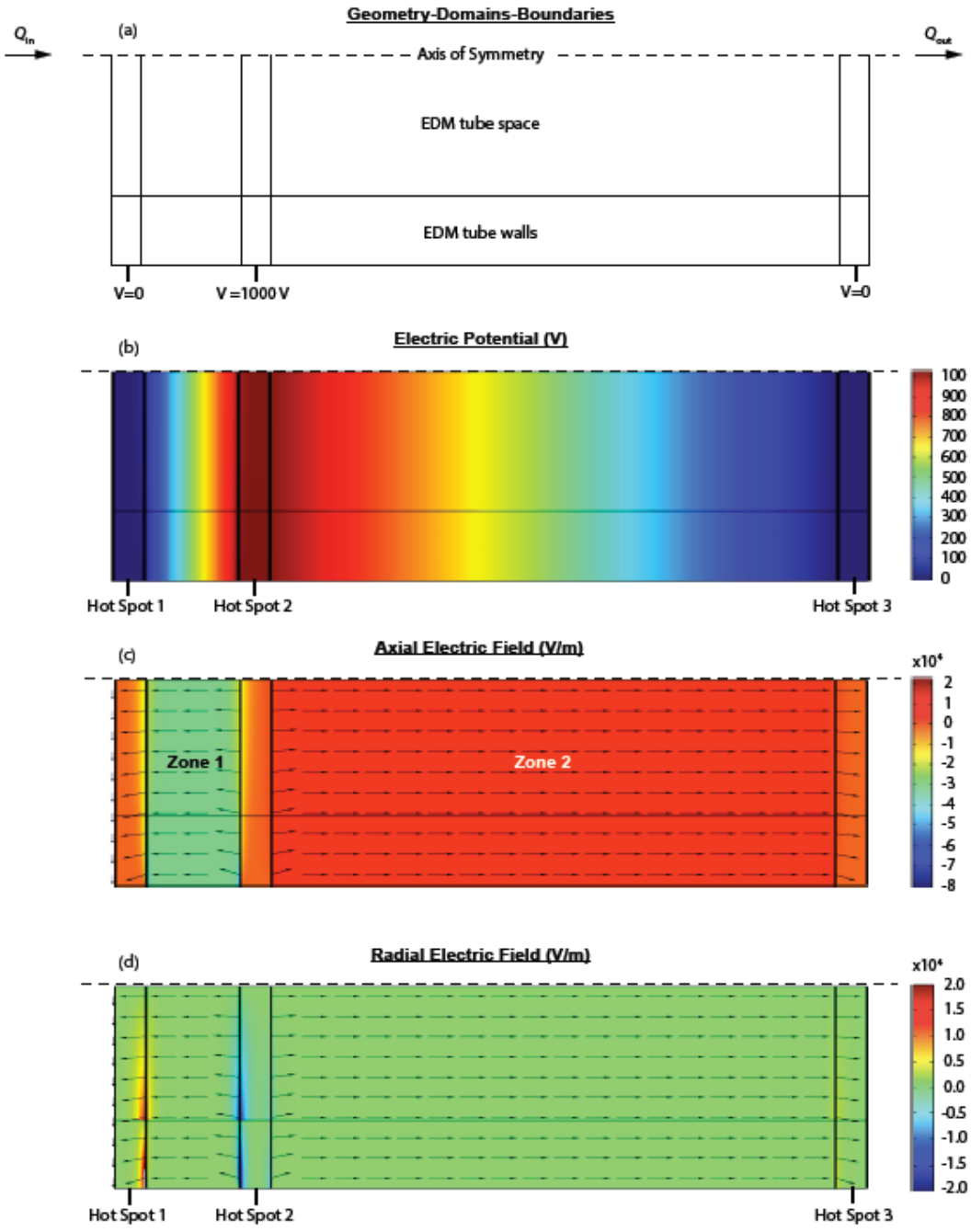

Fig. S6.2. Predicted electric field strength within the EDM tube when 1 kV is applied on the intermediate electrode. The calculations performed using COMSOL multiphysics® show (a) the Geometry, (b) the voltage profile, (c) the axial component E_z, and (d) the radial component E_r of the electric field. Zones 1 and 2

respectively denote the region upstream and downstream the intermediate electrode where the high voltage is applied, while the "Hot Spots" indicate locations where E_r is significantly stronger compared to the rest of the area within the EDM tube. Note: The aspect ratio in all plots is distorted to highlight the above-mentioned features, while the arrows are used to illustrate the electric field direction and not its magnitude.

S6.5: The Volatility Tandem DMA-EDM tube system

The EDM segregator was used in tandem with a DMA and in parallel with a TDMA (Mendez et al., 2016) for probing the volatility of ammonium sulfate particles having mobility diameters of 20 and 30 nm at room temperature (cf. Fig. S6.3). Ammonium sulfate particles produced by atomization were dried and charge neutralized before classified by the first DMA of the system. The monodisperse aerosol stream downstream the first DMA was exposed to temperatures varying from 25 to 230 ºC, inside a thermal denuder (TD; Fierz et al., 2007). Half of the sample flow (i.e., 0.3 lpm) downstream the TD was introduced to the second DMA (part of the VTDMA) which was operated at a scanning voltage, while the particle number concentration was measured by a CPC (TSI Model 3022A). The other half of the flow downstream the TD was passed through the EDM-tube, the voltage of which was changed between 0 and V volts, while the number concentration of particles was measured downstream by a second CPC (TSI Model 3776).

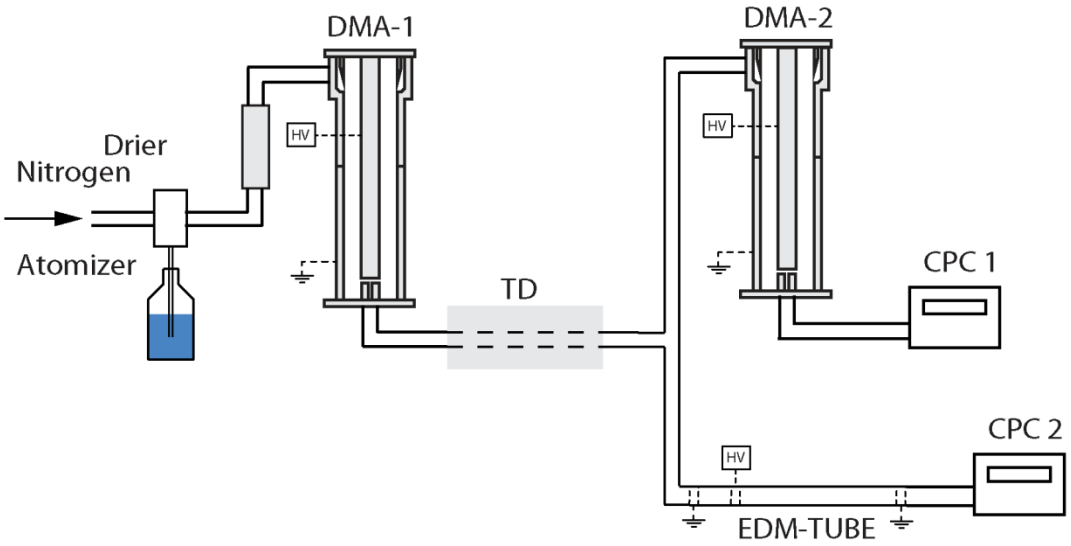

Fig. S6.3: Experimental setup for measuring the volatility of ammonium sulfate particles with a custom made TDMA and a tandem DMA-EDM-tube system.

The shrink factor of particles exposed at temperature (T), is given by:

$$sf(T) = \frac{d(T)}{d_{25C}}, \quad \text{(S6.5)}$$

where $d(T)$ and d_{25C} are the size of particles at temperature T and at room temperature (25 ºC), respectively. The particle size for every temperature was calculated either from the geometrical mean diameter (i.e., from the VTDMA measurements) or from their relative penetration through the EDM-tube (using Eq. 6.1). Figure S6.4 shows the shrink factors of ammonium sulfate particles, having mobility diameters of 30 and 20 nm at room temperature after being exposed to temperatures ranging from 25 to 230 ºC.

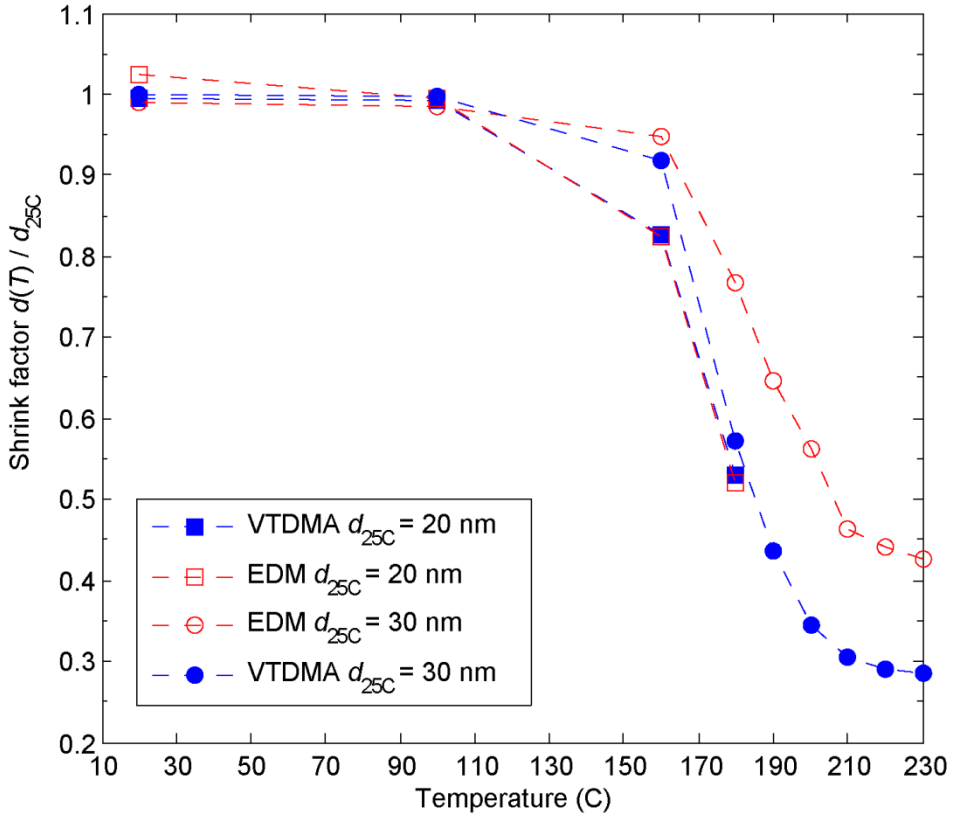

Fig. S6.4: Shrink factors of ammonium sulfate particles having mobility diameters of 20- and 30-nm at room temperature, after being passed through the TD and exposed to temperatures from 25 to 230 ºC.

The shrink factors obtained from the VTDMA and the tandem DMA-EDM-tube measurements were almost identical for the case of the 20-nm particles, while deviations of ca. 20% were observed for the 30-nm particles. These deviations could be justified by a wider, than a unimodal (i.e., standard geometric deviation of more than 1.2), particle size distribution downstream the TD, probably due to partial evaporation of the 30-nm particles

above 170 ºC. 20-nm particles exhibited narrow size distributions (i.e., measured by the VTDMA), resembling a monodisperse population in all tested temperatures (cf. Fig S6.5a as an example). In this case, the size of particles can be more accurately predicted by their relative penetration (cf. Eq. 6.1) through the EDM-tube as the resulted size distribution downstream the tube would be also unimodal. In contrast, as Fig. S6.5b shows, 30-nm particles exhibited a bimodal size distribution (i.e., measured by the VTDMA) after being exposed to increased temperatures. When these particles pass through the EDM-tube the smaller particles of the distribution will be more efficiently deposited on the walls of the tube, than the larger ones as the size distribution downstream the EDM-tube suggests (cf. red line in Fig. S6.5b). In this case the apparent particle size (derived from the semi-empirical equation) would be biased towards larger diameters.

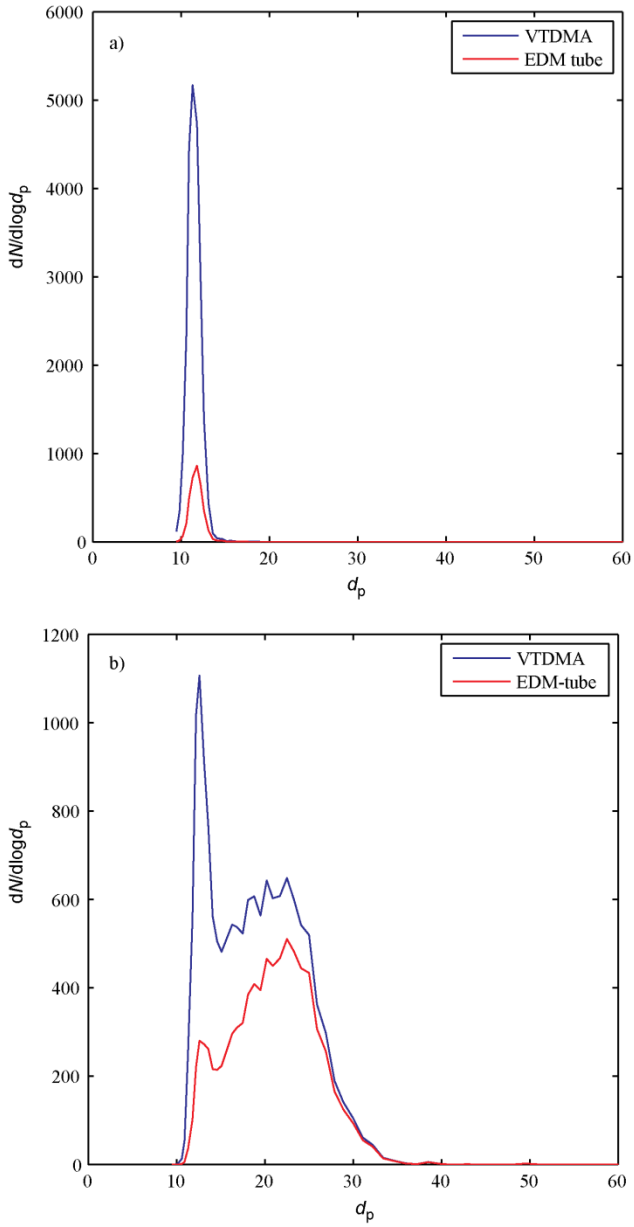

Fig. S6.5: Example of particle size distributions of 20- (**a**) and 30-nm (**b**) obtained with the VTDMA and the EDM-tube downstream the TD at temperatures higher than 170 ºC.

References

COMSOL® multiphysics version 4.3b. Reference manual. Stockholm, Sweden: COMSOL AB

Fierz, M., Vernooij, M. G. C., & Burtscher, H. (2007). An improved low-flow thermodenuder *J. Aerosol Sci*, 38, 1163–1168.

Hinds, W. C. (1999). Aerosol Technology: Properties, Behavior, and Measurement of Airborne Particles, 2nd Edition. John Willey & Sons, Inc.

Leonard, G., Mitchner, M., & Self, S. (1967). Particle transport in electrostatic precipitators. *Atmos. Environ.*, 14:1289–1299.

Mendes L., Eleftheriadis, K., Biskos G. (2016). Performance comparison of two thermodenuders in Volatility Tandem DMA measurements. *J. Aerosol Sci.*, 92, 38-52.

Pecht, M. (2000). In "The Electrical Engineering Handbook". Boca Raton: CRC Press LLC.

7. Conclusions

The overall aim of this thesis is to investigate the hygroscopic properties of atmospheric sub micrometer particles at remote and suburban locations of Greece. The first part of the thesis therefore provides state-of-the-art field observations of aerosol hygroscopicity at a remote location in the country (namely on the island of Lemnos), as well as measurements at sub-urban locations at the cities of Patras and Athens. Identifying the limitation of the measurements, the second part of the thesis goes beyond the state-of-the-art on aerosol instrumentation, providing a theoretical analysis of possible artefacts in hygroscopicity measurements as well as new designs that can further improve the aerosol hygroscopicity measurements. Below is an overview of the conclusions from each chapter, excluding the introduction (Chapter 1).

Chapter 2 provides measurements of particle hygroscopicity and chemical composition which were respectively conducted at a remote location on the island of Lemnos and over the Aegean Sea using an airborne AMS, during a period with prevailing northern winds (i.e., Etesians). The hygroscopicity measurements showed that particles sizing from 50 to 170 nm had medium hygroscopicities exhibiting an average growth factor of 1.2 and were internally mixed. A good closure between the measured and the estimated (i.e., from chemical composition) hygroscopicity allowed for the estimation of the aerosol hygroscopic properties over the entire Aegean Sea. Despite the variability in particle hygroscopicity caused by the different origin and paths of the air masses reaching the region, the median values of particle hygroscopicity were similar to the ones of continental aerosol particles.

Measurement of aerosol hygroscopicity and mixing state in suburban areas in Patras and Athens are provided in Chapter 3. The particles mixing state was, as expected, influenced by the prevailing winds, resulting in an increase in the fraction of externally mixed particles when the winds were crossing the nearby cities. During periods of increased externally mixed fraction, the population of less hygroscopic particles was also increased, indicating that freshly emitted particles from the cities are less hygroscopic than the aged ones. Particles observed in the suburban area of Patras exhibited hygroscopicities similar to those observed for continental Europe aerosols. In contrast, aerosols measured in the suburban area of Athens exhibited higher values of hygroscopicity, which in many cases

were even higher than that of ammonium sulfate. While the presence of significant amounts of highly hygroscopic refractory matter (e.g., sea salt) on the sampled particles can be excluded, other causes, like the existence of highly hygroscopic, but uncommon to the atmosphere, organics or even instrumentation artifacts should be further investigated.

A detailed theoretical analysis of the effects of RH/temperature non-uniformities inside the second DMA of an HTDMA system is provided in Chapter 4, using a numerical model. The model findings corroborated earlier experiments, where non-prompt deliquescence behavior of 10 nm ammonium sulfate particles was observed when the second DMA of an HTDMA systems was operated under mismatched RHs of the aerosol and sheath flow. Considering the uncertainties of typical RH/T sensors used in HTDMAs, recommendations are provided for reducing these artifacts. A similar theoretical model can be useful in investigating possible instrumentation artifacts during the measurements conducted in Athens.

Chapter 5 describes a simple modification of the classical DMA design by including 3 monodisperse particle outlets at its central rod, providing the ability to classify simultaneously particles of 3 distinct populations and therefore when used as the first DMA in HTDMA systems decreasing the measuring cycle time of the systems substantially. Its performance was tested under laboratory conditions and compared with theoretical predictions. The results show that the theory can accurately (within 3%) predict the geometric mean diameter of the sampled particles for all the outlets. The measured resolutions of the first and the third outlet are in good agreement with the theoretical predicted ones (i.e., less than 6% difference). Despite a discrepancy between the theoretical and the measured resolution of its second outlet, this modified DMA can be used for determining the hygroscopic properties of aerosols and reduce the measuring cycle of size resolved measurements, when employed as the first DMA of TDMA system.

Finally, Chapter 6 describes a simple, effective and compact electrostatic precipitator that can be employed for size segregation of charged aerosol nanoparticles. A possible application of this simple segregator for probing the volatility of aerosol particles is also investigated in this chapter. While its sizing resolution and accuracy is not better than systems which employ DMAs, its negligible cost and increased portability poses an advantage in certain applications, where quantity leads to increased quality. Such

applications could involve an array of instruments for increasing the spatial resolution of environmental monitoring, without the need of increased expenses, or light systems which could be part of a portable network of sensors.